UNIVERSITA' DEGLI STUDI DI NAPOLI
"FEDERICO II"
FACOLTA' DI INGEGNERIA

DOTTORATO DI RICERCA IN INGEGNERIA AEROSPAZIALE, NAVALE E DELLA QUALITA'
XXII CICLO

Plasma Wind Tunnel Testing of Ultra High Temperature Ceramics: Experiments And Numerical Correlation

Coordinatore:
Prof. A. Moccia

Candidato:
Ing. Andrea Di Maso

Tutor:
Prof. R. Savino

Index

Abstract

The space flight isn't a purely military and strategic objective, no more, now it's has become an important commercial resource. The space flight has brought many advantages also to the common people. Every body experiments the benefits of the satellite, for communications, for earth observation and for positioning systems. Many of us are going to experiment the advantages in studying the extra terrestrial bodies. Some of us will be able to go in to the space as tourist.
The space flight requires high velocity and altitude that results in high values of potential and kinetic energy, for this reason, requires careful considerations about system concept design and trajectory definition. In fact when a body flies at a such high velocity as that required by the space flight, the friction of the air on it's surface cause a high heating (in the order of thousands of Kelvin degrees). Particular hazardous is the re-entry phase. The space vehicles design is driven by the heat protection [1] for this reason it's important the thermal protection system of the vehicle, especially when the spacecraft is manned.
The most used space vehicle is the capsule. The capsule is simple and economical but isn't manoeuvrable and flexible. The Space Shuttle is a semi-lifting and multi-purpose spacecraft but it's complex and expensive.
An alternative system to re-enter Earth atmosphere, is based on slender vehicles with sharp edges, flying at moderate angles of attack. Sharp leading edges would imply lower aerodynamic drag, improved flight performances and crew safety, due to the larger cross range and manoeuvrability along with lower accelerations [2,3,4,5]. As in any thermodynamic process, also for the hypersonic flight there is the need to minimize entropy, it is recognized that slender bodies and sharp components are critical to hypersonics in the broad sense, e.g., for re-entry as well as for missile applications and for cruiser or launchers in the future. The idea of a slender spacecraft isn't new, already in the fifteen E. Von Braun, R. Carman and H. Drake of the NACA designed combinations of booster-orbiter reusable vehicles with sharp nose and wings [1]; but only now the technology permit us to implementing a such project.

Fig. 1. The Orion Capsule. The capsules are not manoeuvrable, are not flexible to the changes during the missions and are not reusable.

Fig. 2. The Space Shuttle re-enters more as a capsule than an aerodynamic vehicle, is very expensive and the complicated thermal shield subject to damages, is reusable only after a long refurbishment.

Fig. 3. The slender vehicle configuration.

Because the temperature at the tip of the leading edge is inversely proportional to the square root of the leading edge nose radius, the reduced curvature radius results in higher surface temperature than that of the actual blunt vehicles that could not be withstood by the conventional thermal protection system materials. A new class of ceramic materials the Ultra High Temperature Ceramics (UHTC) has been proposed for thermal protection system (TPS) based on hot structure concept. Metallic diborides, as Zirconium, Hafnium and Titanium with different additives, are candidates for thermal protection materials in both re-entry and hypersonic cruise vehicles because of their high melting points (>3000 K) and excellent chemical stability [6,7,8,9,10]. These materials are also characterized by high hardness, high electrical and thermal conductivity; in particular the relatively high thermal conductivity is useful to reduce the stagnation point temperature. In fact, the convective heat transfer entering the surface is partly transported in to the solid and partly re-radiated into the atmosphere. When a steady state is achieved, global radiative equilibrium is established, in the sense that the overall convective heat flux is perfectly balanced by the overall surface radiative flux.

The heat flux distribution over typical geometries of nose and wing leading edge of space vehicles, exhibits the typical dependence by the inverse of the square root with the distance from the stagnation point and therefore decreases by increasing boundary layer thickness (boundary layer thermal protection) [11,12]. Thus there is a relatively small heat flux at distances sufficiently downstream of the leading edge. This suggest the adoption of a massive thermal protection system only in the tip region of the vehicle, while the remaining part of the vehicle's surface can be free from heavy protections.

The present work deals with the study of different Ultra High Temperature Ceramics models; the research has been carried out with a joint venture with the ISTEC-CNR (Institute for Ceramic Technologies) of Faenza (Ra). The method is either experimental and numerical and includes the following steps:

- sintering of UHTC material with the chosen composition*

- Investigation of the thermo-mechanical properties*

- Definition of the settings to achieve the selected experimental test conditions in the arc-jet SPES facility

- Execution of arc-jet tests, monitoring the temperature evolution of the sample and estimation of spectral emissivity

- Numerical rebuilding of the tests in order to characterize the plasma flow, the chemical and thermal environment and to evaluate the catalytic behaviour of the materials

• SEM, EDX, and X-ray diffraction (XRD) analysis on the surface and inside the specimen to investigate the effects of arc-jet heating.*

*This steps have been executed at the ISTEC-CNR.

This work deals with the study of arc-jet experiments on different Ultra High Temperature Ceramics models. Typical geometries of interest for nose tip or wing leading edges of hypersonic vehicles, as rounded wedge, hemisphere and cone are considered. Temperature and spectral emissivity measurements have been performed using pyrometers, an IR thermocamera and thermocouples. The UHTC materials have been tested for several minutes to temperatures up to 2250 K showing a good oxidation resistance in extreme conditions. Fundamental differences between the various model shapes have been analysed and discussed.

Arc-jet testing represents the best ground-based simulation of a re-entry environment, in different ways. On one hand, it provides the possibility to test the behaviour of these materials under extreme conditions. On the other hand, the materials response to large heat fluxes is evaluated through the determination of two important parameters, i.e. emissivity and catalytic efficiency. High values of emissivity and low values of surface catalytic efficiency are desired for the above mentioned applications as they reduce temperature gradients and thermal stresses in the structure, thus enabling the vehicle to operate under relatively high enthalpy flow conditions.

The arc-jet tests reported in the present work have been carried out at high total enthalpy (5-16Mj/kg typical of atmospheric re-entry environment) in hypersonic flow conditions ($M \cong 3$) . The surface temperature and emissivity of the materials have been evaluated.

Fluid dynamic numerical simulations were carried out to evaluate the details of the flow and thermal heating, as well as the catalytic efficiencies of the materials.

Preface

In the chapter I there is a brief description of the hypersonic flight, there is also described why hypersonic is important. An introduction on the hypersonic vehicles and their thermal protection systems is included. The fundamental characteristics of the flow field and some utility formula are indicated. Some historical note about the hypersonic flight will help us to understand better the situation today and the hypersonic operative vehicles of our times, as well as the re-entry vehicles of the future. The reader with relevant skills about the hypersonic and re-entry vehicles can avoid this chapter.

In the chapter II there is a description of the Ultra High Temperature Ceramics (UHTC) materials.
There are depicted the composition and the properties of several of the most important UHTC.
The methods of sintering, manufacturing is explained. What are the preferred mechanical chemical and physical performances. The most common analysis methods for these materials are explained.

In the chap III, a general description of the ground based facilities for the study of hypersonic flight is included. There is the description of the Small Planetary Entry Simulator (SPES) facility. The SPES is an arc-jet facility, and has been used extensively to experiment the UHTC in the present work. There are listed the capabilities, performances and limits for this facility.
A description of the diagnostic set up is included. At the end the test bed configuration selection is depicted.

In the chapter IV the numerical models are explained. A general description of the CFD utilities and advantages in plasma wind tunnel studies is given. A description of chemical models used in the CFD computations, examples, with advantages and problems, is included. The difference between the laminar and turbolent model is given. There is an explanation of the thermal non equilibrium model. The most widely used model is explained, with relative boundary conditions. The method for thermal analysis is described.

In the chapter V there are the fundamental results of present work. Several experimental arc-jet tests on UHTC are shown, with the relative measured conditions. The details of arc-jet testing are shown, by using the results of the numerical models. The SPES environmental characterization has been done by plots and contours of fluxes, of species, and of pressure, in various test conditions. The rebuilding of UHTC models thermal heating shows us the importance of the geometry and chemical-physical properties of the material in the temperature achieved.
The are the post test analysis performed which allow us to understand the model behaviour in the arc-jet conditions.

Chap. I. Introduction

I.1. Hypersonic flight

From the first aircraft which travelled below 50km/h at altitudes below one thousands meters, in the early 1900; the desire of the men was to fly higher and faster. Finally the first hypersonic flight was achieved in 1949 with a two stage rocket the first of which was a German V2.
The hypersonic is different from subsonic or supersonic flow. The subsonic and supersonic vehicles are different from the hypersonic, in fact the first two have the fuselage, wings, tail, and engines separated among them, instead the vehicles for re-entry appear as an unique body. Hypersonic can a be considered a flow both at Mach above 3 and at Mach numbers above 12; it is not characterised by Mach number, but by particular phenomena (Fig. 4):

- Strong shock waves, resulting in high temperatures from 2000 up to 11000K; at this temperature the air becomes a chemical reacting mixture, and above 8000K the ions presence can't be neglected.
- The strong shock wave is curved by the flow velocity, thus for slender vehicles the wave angle is only 20% larger than the wedge angle, this implies a shock wave very close to the body.
- The curvature and closeness of shock wave results in a entropy layer which causes high vorticity in the shock stratum, the entropy layer embodies the boundary layer complicating the solution of flow field around the body.
- In hypersonic conditions, the boundary layer is thick, because $\delta \cong \frac{M^2}{\mathrm{Re}}$, this makes the geometry of the vehicle appear different; this phenomena is called the viscous interaction and complicates the solution of the outer flow field.
- For Mach number above 11 the radiation from the gas in the shock wave can't be neglected, and during the lunar re-entry at Mach 36 the radiation is about the 30% of the total heat flux.
- Because the high temperatures the vibrational and electronic degrees can be excited, and because the high velocities of the flow, the characteristic convective time can be lower than the characteristic time of energy exchanging between the freedom degree, thus to calculate the energy it could be important to consider different temperatures: for the translation – rotation, for

the vibration, and for the electronic energy. I.e. it can be necessary to consider the thermal non equilibrium.

- The hypersonic flow is inherently non linear, because it involves non linear phenomena as the chemical reactions, the lift and drag coefficient are non linear function of the angle of attack.
- Is not possible to study the aerodynamic of every part of a space plane separately and then summing the effects, as can be done for subsonic and supersonic aircraft.

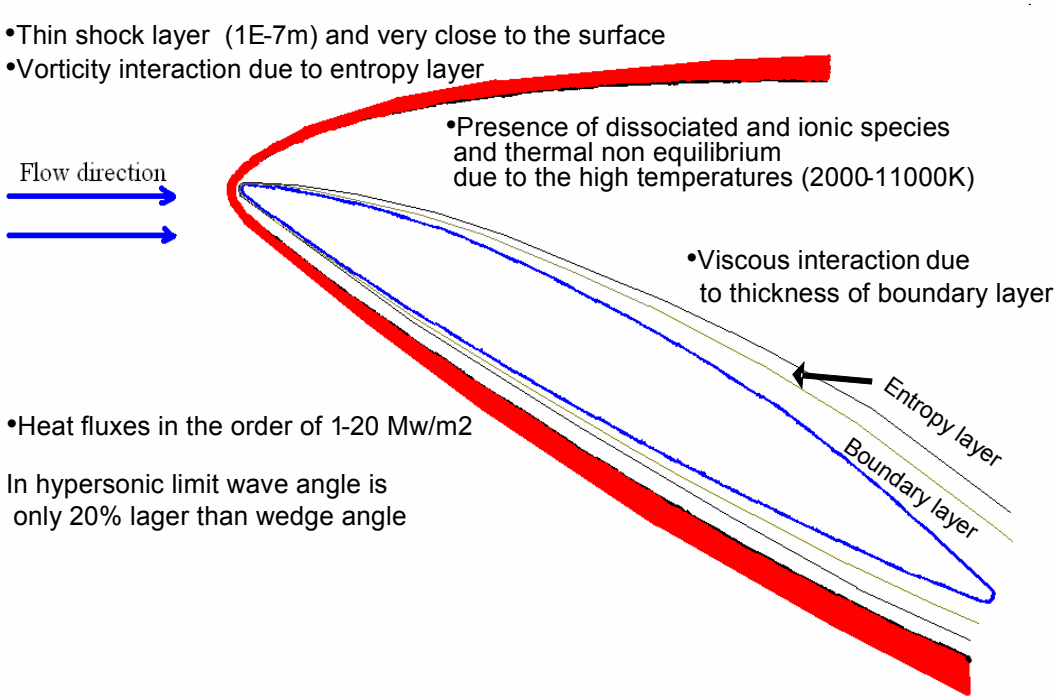

Fig. 4. Features of hypersonic flight.

To achieve the space flight the terrestrial gravity must be won, by high altitudes (above 300km) with high velocities (above 10km/s). Finally the fast progress of missiles for military purposes allowed in 1957 the first satellite launch, and in 1961 the first manned space flight. Today there are about 25 launches for year, of which 5 or 7 manned, and the launches will increase in the next future. The hypersonic flight is important because is necessary for the space missions, especially in the re-entry phase of the manned missions. Today the manned hypersonic operative vehicles, are: the Soyuz, the Shenzhou and the Space Shuttle. The first two are capsules, instead the Space Shuttle is a reusable multi-purpose spacecraft.

The capsules are not reusable and flexible but are simple. The Space Shuttle is a flying laboratory, it is flexible, and it is a semi-lifting body that can fly as an aeroplane at the lower altitudes. The Space Shuttle is very expensive and reusable only after a long period of refurbishment.

For the next future the NASA has programmed to substitute the Space Shuttle with the Orion, a capsule, to lower the costs.

I.2. The thermal protection system

Re-entry heating is different from normal atmospheric heating associated with jet aircraft. The skin of high speed jet aircraft can become hot from atmospheric friction, but this is frictional heat, instead the vast part of the heating the vehicles experience during re-entry, over 80 percent, is caused by compression of the air ahead of the vehicle, the shock wave.

The first objective to consider in the design of a re-entry vehicle, is the heat protection rather than the aerodynamic efficiency, for this reason the thermal shield is the fundamental part of a space vehicle. The capsules espouse exactly the first objective. If the cone-wedge angle of the nose of a hypersonic vehicle is bigger than the maximum allowed for the attached shock wave, the shock wave becomes detached. The detached shock wave warms up the vehicle much less than the attached one. The capsules are blunt vehicles, they are characterized by a low ratio of lift coefficient C_f on drag coefficient C_D, in fact the heat transfer efficiency is $\eta_q \cong \frac{C_f}{2C_D}$. The capsule use also an ablative thermal shield to subtract the incoming convective heat by ablative heat; in fact the net wall heat flux formula for the ablative capsule is: $\dot{q} = h_{conv}\left(T_{fluid} - T_{wall}\right) - \sigma\varepsilon T_{wall}^4 - \dot{m}\lambda_{sublimation}$ where the convective heat flux is $h_{conv}\left(T_{fluid} - T_{wall}\right)$, the heat flux irradiated by the surface of the capsule is: $\sigma\varepsilon T_{wall}^4$, the heat subtracted by the ablation from the surface is $\dot{m}\lambda_{sublimation}$.

The capsules heat shield burn off during re-entry and so couldn't be reused. Because a lot of successful missions achieved, this technology of thermal insulation is robust and reliable, and the single-use nature was appropriate for a single-use vehicle.

Fig. 5. The heat shield of Orion.

The Space Shuttle re-enters the atmosphere as a blunt body by having a very high (40 degrees) angle of attack, with its broad lower surface facing the direction of flight, this to increase the drag coefficient, to detach the shock wave, and to minimize the heating of the vehicle.

The Space Shuttle must be re-usable and manoeuvrable at low altitudes to can land as an aircraft, for this reason can't have an ablative thermal shield. The thermal protection system (TPS) is the union of

different protection types. They are in two basic categories: tile TPS, and non-tile TPS for the leading edges where the temperature is higher. The main selection criteria is using the lightest weight protection but capable of handling the heat in a given area.

Much of the shuttle is covered with 24300 LI-900 silica tiles coat made of low density silica fiber made. The tiles can withstand at temperature up to 1550K and create a thermal insulation that prevents heat transfer to the underlying aluminium structure.

The tiles are not mechanically fastened to the vehicle, but glued. Since the brittle tiles cannot flex with the underlying vehicle skin, they are glued with silicone adhesive, which are in turn glued to the Space Shuttle skin. These isolate the tiles from the structural deflections and expansions of the aluminium structure.

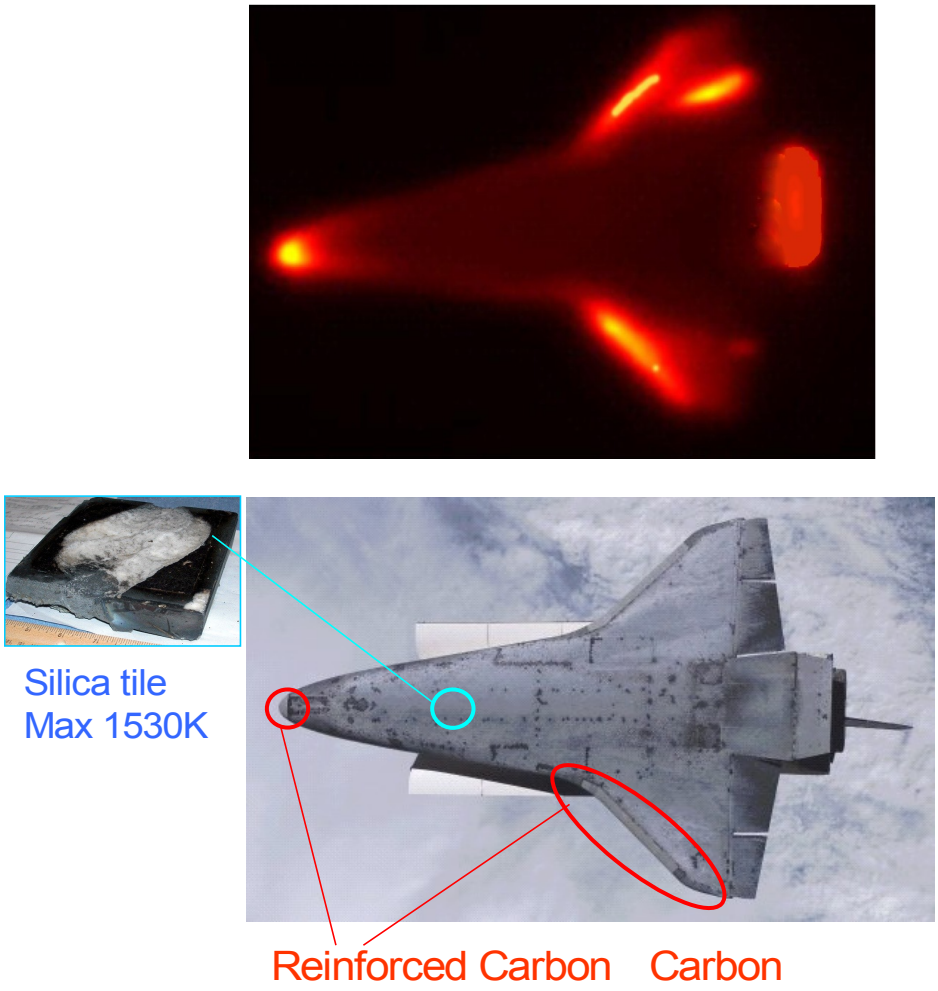

Fig. 6. A thermography of the Space Shuttle and an image of the thermal shield, the zones where the temperature is high are yellow in the thermography, and indicated by a red circle in the photo, the zone where there are silica tiles is indicated by the blue circle, also a damaged silica title is shown.

The leading edges are made of Reinforced Carbon Carbon (RCC) panels. The RCC is Carbon-carbon composite consisting of highly-ordered graphite fibres embedded in a carbon matrix, the external surface is protected from the oxidation by the presence of a silica (SiO_2) glass scale. Reinforced Carbon Carbon composites are made by gradually building up a carbon matrix on a carbon fibre through a

series of impregnation and pyrolysis steps or chemical vapour deposition. Oxidation protection is afforded by converting the outer layers of the RCC to SiC by chemical vapour deposition, at high temperatures in an oxidizing environment, the SiC layer forms the protective SiO_2 scale.
This composites tend to be stiffer, stronger and lighter than steel or other metals, they can resist at temperatures up to 1920K for up to 15 minutes in the presence of an extremely oxidizing plasma environment. RCC is also a good thermal insulator in the order of 1/10 of the iron.

I.3. The slender re-entry vehicles

A reusable sharp hypersonic vehicle should be manoeuvrable as an aircraft, but not complicate, big and heavy as the Space Shuttle. A light and aerodynamic vehicle can generate lift at high altitude having a long duration re-entry flight. The long duration re-entry flight allow a gradually deceleration, for this, the vehicle gradually convert its enormous kinetic and potential energy into thermal energy. These vehicles will be more secure because the astronauts will be able to control the plane along the entire flight path. This vehicle will has an extensive down and cross ranges so could return from nearly any point along the orbit and land at different sites, on contrary the Space Shuttle has a very narrow window to land at a pre-selected site, and the capsules have a ballistic trajectory.
Re-entry vehicles with enhanced aerodynamic performances and high manoeuvrability require sharp leading edges for the wings, control surfaces and sharp tip of the fuselage nose. This geometric configuration made high heat fluxes. In fact the wall heat flux is inversely proportional to the square root of the curvature radius. For a non ablative thermal shield the net wall heat flux is $\dot{q} \propto \sqrt{\frac{P_{02}}{R}}\left(H_0^{fluid} - H_0^{wall}\right) - \sigma\varepsilon T_{wall}^4$. The high wall heat fluxes and the consequential high temperatures have been the cause that have forbidden the construction of such hypersonic vehicles up to date. The UHTC materials can withstand at temperature thousands of degree higher than the thermal shield today used. This material will made possible the construction of slender re-entry vehicles. Furthermore the heat flux distribution over the nose and the wing leading edge of space vehicles, exhibits the typical dependence by the inverse of the square root of the distance from the stagnation point and therefore decreases by increasing boundary layer thickness. The boundary layer thermal protection concept [12] allows the use of the new Ultra High Temperature Ceramics only in the fore-parts of the vehicle Fig. 7. Thus the thermal shield of the vehicle is light relatively to the standard re-entry vehicles of today.

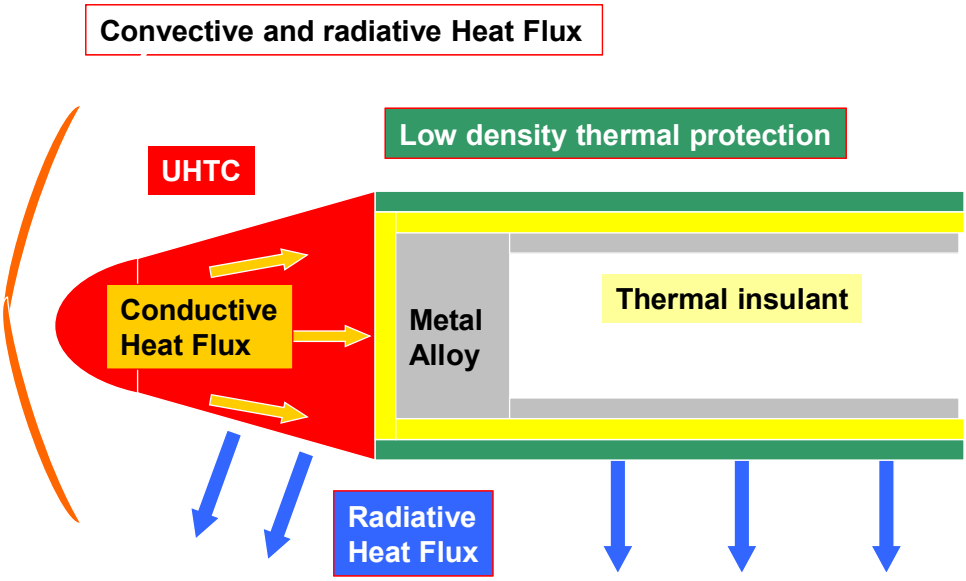

Fig. 7. Wing section sketch of a re-entry vehicle equipped with UHTC thermal shield.

Chap. II. UHTC materials

Refractory intermetallic compounds such as ceramic carbides, borides, silicates and nitrides are characterized by high melting points, high hardness and good chemical inertness. These refractory materials have been termed Ultra High Temperature Ceramics.

Although RCC and SiC can withstand at temperatures up to 2000K they are not classified UHTC.

Ultra-high temperature ceramics (UHTCs) are currently considered as emerging materials for aerospace applications [13,14,15,16] because their capability to withstand in extreme environment, such as conditions experienced during re-entry. The increasing attention on this class of materials is driven by the demand of developing re-usable hot structures as thermal protection systems of re-entry vehicles characterized by sharp leading edges and therefore by large aero thermal heating. The sharp vehicles will have to withstand temperatures that may exceed 2000 K during re-entry. As available materials can not survive such extreme temperatures, new ones are required for advanced thermal protection systems, such as the UHTCs [11,13,15,16,17]. The first UHTC have been developed since the ’60 by US Air Force to construct the noses of the Intercontinental Ballistic Missile (ICBM), and the leading edge of hypersonic vehicles. NASA’s Ames Research Center concentrated on developing materials in the HfB_2/SiC (boride/carbide) family for a leading-edge application. The work focused on developing a process to make uniform monolithic materials, and on the testing and design of these materials. Other composition of ceramic have been developed, for example the nitrides, carbides, and the fiber-reinforced composites. Many additives at the primary phase have been studied, to improve the thermo-chemical and mechanical properties, including nano-particles.

In comparison to carbides and nitrides, the diborides tend to have higher thermal conductivity, which gives them good shock resistance; the diborides have also better oxidation resistance than other UHTC [8]. Because their chemical inertness, the UHTC diborides are ideal for molten metal crucibles, thermowell tubes for steel refining, for the shells of combustion chamber, and as parts for electrical devices such as heaters and igniters.

II.1. Methods of sintering, manufacturing

There are several methods of sintering of UHTC. Here will be described the sinterization process of an HfB_2 matrix with $TaSi_2$ (15%vol), via hot pressing (HP), see Fig. 8 for the block diagram. The UHTC fabrication have been performed at Institute for Science and Technology for Ceramics (ISTEC). The starting powders are provided as pulverized substance with certified maximum granulometry. Because lumps are usually present, the powders are submitted to ultrasound and sieved. The first step is mixing of the HfB_2 with $TaSi_2$, the two powders are inserted in a cruet with 3 parts of pure etilic alcohol, and several HfO_2 spheres; the cruet is mixed for one day, to be sure of the perfect isotropy of the mixture. After the mixing, whole is dried and sieved to extract the alcohol, and the HfO_2 spheres. In the second step the powder is pressed by two metallic cylinder at 150 MPa, at room temperature and pressure i.e. 300K and 10^5Pa in air, to compact the mixture for the successive step of the Hot Pressing (HP) furnace. In the third step the compacted powder is inserted in the HP furnace between two graphite cylinder (Fig. 9) at a pressure of 300MPa, the whole is heated for sintering. The sintering method via HP is one of the most used, the graphite dies surrounding the UHTC powder are warmed up by electric induction. Pyrolytic graphite paper covered by a boron nitride wash is interposed between the UHTC powder and the dies to hinder diffusion of material. The furnace atmospheric pressure is at 100Pa to prevent the oxidation phenomena. In Fig. 10 there are the relative density=density/density of ideal mixture, and the temperature Vs. time. The controlled heating

generates a linear function of temperature Vs. time (Fig. 10). The temperature increasing is stopped when the slope of the curve of relative density Vs. the time decreases; also if the furnace temperature and pressure is constant at 1970K, the relative density continue to increase, because of the chemical reactions. It should be underlined that the powder pressed at room temperature has only the 50% of the final density, only by means of temperature above 1500K the grain edges melt merge each other and increase the density.

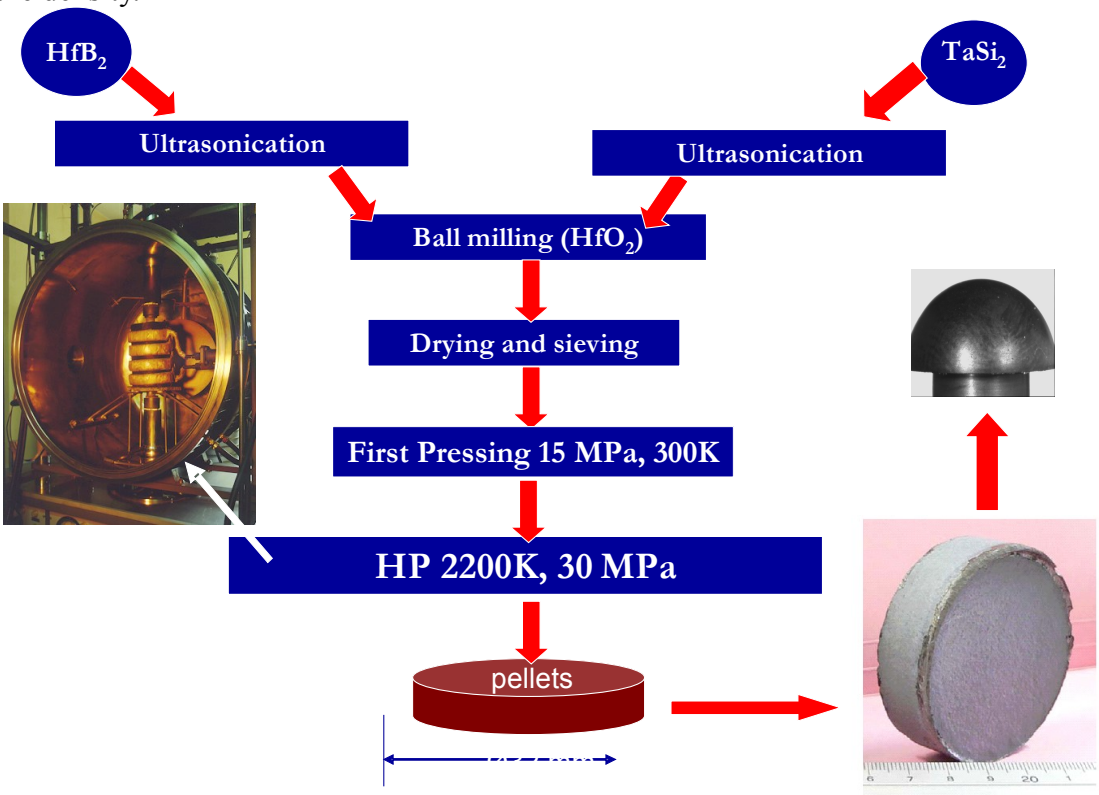

Fig. 8. The UHTC fabrication scheme.

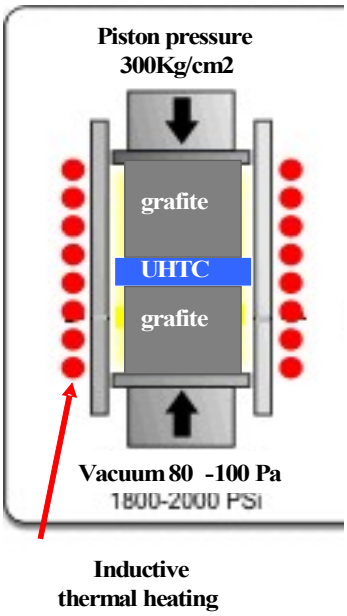

Fig. 9. Sketch of HP furnace.

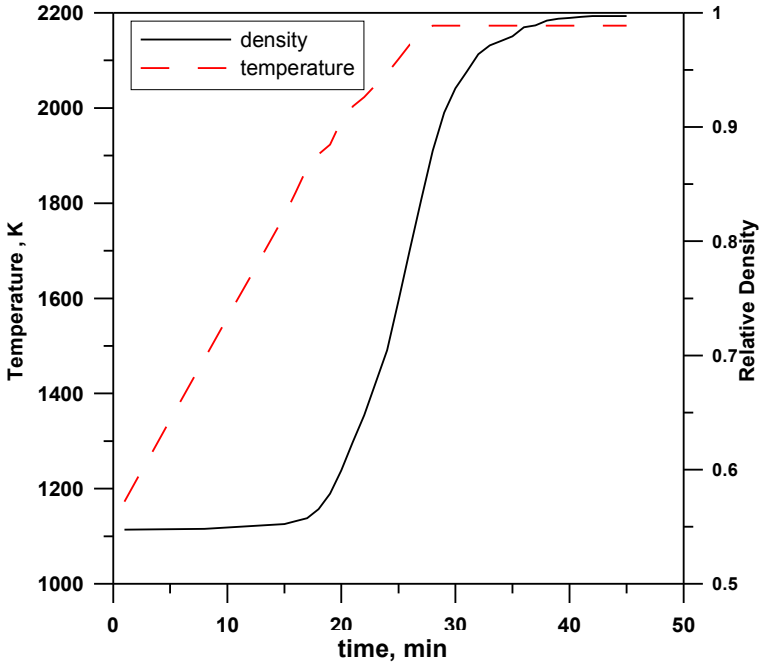

Fig. 10. Relative density and temperature Vs. time for a HP sintering.

The HfB_2-$TaSi_2$ system is not a composite, because there are not differences in form or composition on a macro-scale. The constituents can not be physically identified and they doesn't exhibit an interface between one another. The final product can not be isotropic perfectly, because the applied pressure during the sintering process is directional.

But HfB_2-$TaSi_2$ can appear a composite on a microscale (Fig. 11).

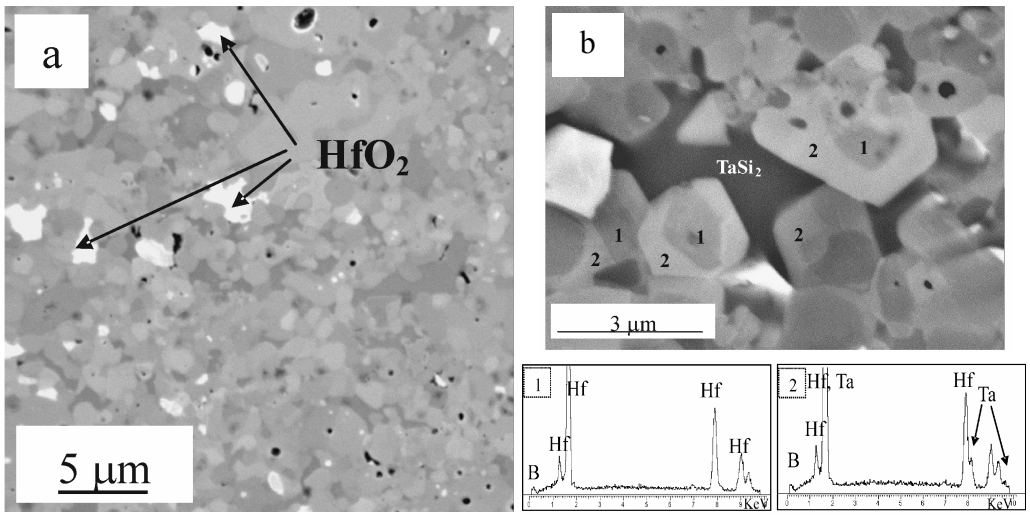

Fig. 11. Polished surfaces of as sintered HfB_2- $TaSi_2$ composite showing in a) the homogeneous and dense microstructure, with HfO_2 crystals. b) Detail of the microstructure evidencing a pocket of $TaSi_2$ phase and the core-rim substructure of HfB_2 grains with the corresponding EDS spectra.

The mean HfB_2 grain size is around 1 mm, which is similar to the starting particle size of the HfB_2 powder, indicating that no significant grain coarsening occurred during sintering. The brightest

phase is identified as HfO_2 . $TaSi_2$ appeared darker than HfB_2. Analyzing the microstructure, many HfB_2 grains exhibited a core-shell structure. By EDS analysis, the outer shell was estimated to be a solid solution with composition $(Hf_{0.8}Ta_{0.2})B_2$ in agreement with XRD analysis.

From the HP is obtained a diskette which is machined by electro-erosion to obtain the desired shape.

II.2. Material properties and characteristics

The diboride compounds have higher thermal conductivity than the other UHTC, this gives them better shock resistance. The diborides have a better oxidation resistance also.

The presence of additives as SiC and $TaSi_2$ have several positive effects as: a better densification, an improved tensile strength and toughness, limited grain grown, and improved oxidation resistance because these materials with oxygen at high temperature produce protective oxides.

In Fig. 12 there is the thermal conductivity for several UHTC in comparison with RCC. The UHTC have a thermal conductivity by one order magnitude higher than RCC, this allows lower stagnation point temperature than RCC but requires a thermal insulation for the structural parts of the vehicle.

Note the anisotropy of RCC because is a composite with carbon fiber.

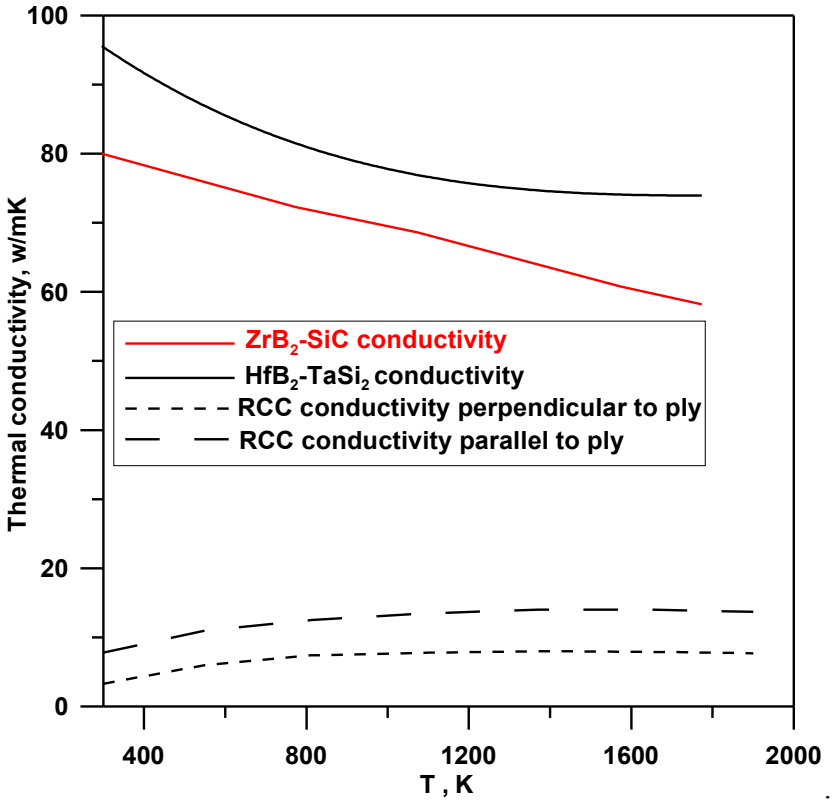

Fig. 12. UHTC and RCC thermal conductivity.

In the Tab.1 are indicated several fundamental properties for selected UHTC in comparison with RCC.

The Flexural strength is also named modulus of rupture at flexure or bend strength, it is the pressure needed to broke a standard model subject to flexure force.

Material	Density	C_p		Thermal Conductivity		Melting temperature	σ Flexural strength
		(300K)	(2000K)	(300K)	(2000K)		
%vol	g/cm^3	J/(kgK)		W/(mK)		K	MPa
HfB_2+15 $TaSi_2$	10.9	400	-	78	-	3513(HfB2) 2500(TaSi2)	210(TaSi2 at 1473K)
ZrB_2	5.3	462	785	104	70	3500	-
ZrB_2-SiC	5.3	466	1773	80	58	3300(ZrB2) 2700(SiC)	730(300K) 1200(1473K)
HfB_2+15 SiC	10.9	241	452	95	66	3513(HfB2) 2700(SiC)	-
SiC (HP)	3.2	750	-	120-153	-	3000	550(300K)
RCC	1.6	840	1200	3.5-8	8-14	1985	322; 50-700

Tab.1. UHTC properties.

The UHTC are heavier than RCC or SiC but have superior mechanical and thermal properties. The RCC flexural strength can change because the direction of the carbon fiber and the dimension of the graphite crystals. The UHTC can have a better oxidization resistance than RCC or SiC and can withstand to higher temperatures. The melting points are important, but the most important thermal feature is the melting point of the oxidation products. In fact at temperature lower than the melting point, the materials react with the oxygen creating new oxide material that can protect the inner bulk phase. This phenomenon is named passive oxidation. Instead if the oxide scale is not able to protect the UHTC, active oxidation occurs. For example the melting temperature of SiO_2 , ZrO_2 , and HfO_2 is 2000K, 3000K, and 3100K respectively. Complicated oxide can form for example the HfB_2-$TaSi_2$ can form $Ta_2O_5 \cdot 6HfO_2$, whom the melting temperature is unknown.

The UHTC by look, toughness, thermal conductivity, and flexural strength appear closer to a metal than a ceramic. By definition a ceramic has random defects that can not be prevented by the production systems of today. These defects can not be seen by non-destructive methods. The probability to have a big defect increases with the dimension of the model. For this reason the mechanical features of UHTC big sized specimens can not be the same as the small sized specimens; today this is the true limit for the application of UHTC. For the future the UHTC will became composite material and or the fabrication techniques will change such to allow a control over the defects.

II.3. The analysis methods

The chemical and physical analysis have been performed at Institute for Science and Technology for Ceramics (ISTEC). The analysis performed on the samples are of two types: morphological and chemical. The morphology is examined by means of optical and electronic microscopes. The chemical is by X-ray diffraction and dispersion.

II.3.A. Electron microscopy

The UHTC can be analysed by means of scanning electron microscopy (SEM). This type of instrument is able to magnification up to 10^6x, in particular the SEM used in the present work, available at ISTEC CNR Faenza, it is able to magnification from 10x up to 2 E5x, or up to 4nm. The focus must be set only once and it is valid for every magnification, because it depends only by the distance of the sample from the electron source.

The SEM has a tungsten string that produces a focused electron beam by thermo-ionic effect. This electron beam arrives to sample surface. At each point on the specimen the energy of the incident electron beam changes and is converted into other forms, such as x-ray emission, emission of low-energy secondary electrons, retro-diffused electron, light emission (cathodoluminescence) and heat. The sensors of the SEM capture the varying intensity of the first three of these signals. The image is constructed from signals produced by a secondary electron detector, the normal or conventional imaging mode in most SEMs. In fact the secondary electron accumulate themselves on the peaks, as every electric charge, and this allow to distinguish the peaks from the depressions, this give a monochromatic but three dimensional image of the specimen's surface.

The retro-diffused electron have higher energy than the secondary electron, this allows them to penetrate the surface in profundity (about 200nm). The expulsion of retro-diffused electron is high when the density of the specimen is high. The retro-diffused electron are detected by another sensor of the SEM, and are used to valuate the superficial density.

The x-rays emitted are detected by another sensor to identify the elemental composition of the specimen. To explain further, when an electron vacancy is filled by an electron from a higher shell, an x-ray is emitted to balance the energy difference between the two electrons. The EDS x-ray detector measures the number of emitted x-rays versus their energy. The energy of the x-ray is characteristic of the element from which the x-ray is emitted. A spectrum of the energy versus relative counts of the detected x-rays is obtained and evaluated for qualitative and quantitative determinations of the chemical elements present.

The greater resolution and magnification of the electron microscope is because the de Broglie wavelength of an electron is much smaller than that of a photon of visible light.

It must pointed out that the sample can be seen by SEM microscope only if its surface is a good electric conductor. The UHTC surface must be polished from organic compounds accurately, and it must be covered by a thin carbon film, by carbon vapour deposition.

Also the transmission electron microscopy (TEM) can be used for morphological UHTC images, the image resolution of an SEM is about an order of magnitude poorer than that of a TEM. However, because the SEM image relies on surface processes rather than transmission, it is able to image bulk samples up to many centimetres in size and (depending on instrument design and settings) has a great depth of field, and so can produce images that are good representations of the three-dimensional shape of the sample.

II.3.B. X-ray analysis

The X-ray diffraction is a method of determining the geometry of crystals. From geometry the qualitative and quantitative chemical composition can be obtained. Any wave impinging on a regular array of scatterers produces diffraction. X-rays was discovered by Roetgen in 1985, they are electromagnetic radiation product by several metals if hit by fast electron, X-ray are defined electromagnetic radiation with $\lambda \in 0.02; 200$ Ångström, these radiations have a shorter wavelength than the visible ones, for that reason higher energy and are more penetrating than the visible light. X-rays are used to produce the diffraction pattern because their wavelength λ is the same order of magnitude (0.5-3 Ångström) as the spacing *d* between planes in the ceramics crystal. A beam of X-rays with a

unique wavelength strikes a crystal and diffracts into many specific directions. From the angles and intensities of these diffracted beams, a crystallographer can produce a three-dimensional picture of the density of electrons within the crystal. From this electron density, the mean positions of the atoms in the crystal can be determined, as well as their chemical bonds, their disorder. The X-ray scattering is determined by the density of electrons within the crystal. In fact every hit electron emits a spherical radiation, the spherical radiations of the electrons interfere with a destructive interference in some directions and a constructive interference in other direction. The intensity and the number of directions of the constructive interference allows to determine the space position of the electrons. Since the energy of an X-ray is much greater than that of a valence electron, the scattering may be modelled as the interaction of an electromagnetic ray with a free electron. Follow this model the intensity of the scattered radiation declines as $1/m^2$ where m is the mass of the charged particle that is scattering the radiation; hence, the atomic nuclei, which are thousands of times heavier than an electron, contribute negligibly to the scattered X-rays. In principle the X-ray analysis can determine the quantity of the detected crystals, but the scattering depends both on the direction of incident beam, and by the orientation of the crystals. For every analysis, many direction of incident beam are used, but the orientation of the crystals is not casual because the sintering method and the gravity force; for this reason the quantitative analysis can be not exact.

Chap. III. Arc-Jet facility description

The hypersonic wind tunnels are the best way to experiment hypersonic condition effects, in a ground based facility, with low cost respect to the flight experiments. Unfortunately there is not the capability to simulate the whole hypersonic condition at the same time. In fact also in the most powerful hypersonic wind tunnel the energy given at the flow it's lower than the energy of the flow that impact a re-entry vehicle. For example during a re-entry from low earth orbit (LEO) the Mach number is more than 20 for several minutes, this generates a blow shock wave with temperatures in the order of 7000K; instead for a lunar re-entry the Mach number is 36 with temperature in the order of 11000K. Since the flow energy can be transformed in kinetic or thermal energy, the hypersonic wind tunnels can reproduce either the kinetic or thermal condition of an hypersonic re-entry. Several types of hypersonic wind tunnels exist, for example the shock tube, the hot wind tunnel (HWT), laser heated hypersonic wind tunnel, and the arc-jet plasma wind tunnel (PWT). The first two are discontinuous in the sense that the time of the experiment is less than one second, the last one is continuous but can obtain limited Mach number. The Small Planetary Entry Simulator (SPES) used for the test in the present work, it is an arc-jet plasma wind tunnel, it is able to reproduce only the thermal condition of the re-entry.

III.1. The SPES facility

The SPES (Small Planetary Entry Simulator) facility, located in the laboratory of the DIAS (Dept. of Aero-Space Science Engineering), University of Study "Federico II", Naples, Italy, is a continuous, open-circuit, blow-down arc facility. It is equipped with:

• A 80 kW plasma torch that operates with inert gas (He, N_2, Ar and their mixtures) at mass flow rates up to 5 g/s. Specific total enthalpies at the exit nozzle up to 20 MJ/kg are achieved at gas mass flow rate of 1g/s.

•Two supersonic nozzle where the flow expands to a nominal Mach number of 3 and 6.

•A pressurized cooling system with de-mineralised water for the torch, the nozzle and the test chamber components.

• A test chamber with infra-red and optical windows.

• The vacuum system is a three stage system composed by mechanical pumps and two boosters allowing a pressure below 100 Pa in the test chamber.

• Swirl mixer where a oxygen can be supplied to obtain desired atmospheric chemical composition.

• Automatic control system allows monitoring the facility main parameter (arc heater voltage and current, water cooling temperature, mass flow rate and test chamber pressure).

One of the main subcomponents of the facility is the plasma torch; with arc voltages of the order of 50-60 V and arc current in the range between 200 and 600 A, specific total enthalpies up to 18 MJ/kg can be achieved at a gas mass flow rate of 1g/s.

For a given mass flow rate and nozzle nominal mach number, the flow is characterized by evaluation of specific total enthalpy at the exit nozzle by means of the energy balance between the energy supplied to the gas by arc heater and the lost energy through the cooling system. It is possible to obtain an average value at the nozzle exit with the following formula:

$$\hat{H}_0 = \frac{VI + c_{pg}\left(T_{fg} - T_g^i\right)\dot{m}_g - c_{pw}\Delta T_t \dot{m}_{wt} - c_{pw}\Delta T_n \dot{m}_{wn}}{\dot{m}_g}$$

Where $\hat{H}_0$ [J/kg] is the average specific total specific enthalpy at the nozzle exit, VI [W] is the supplied power to the gas by arc heater, $\dot{m}_g$, $\dot{m}_{wt}$, $\dot{m}_{wn}$ [kg/s] is the mass flow rate of the gas, of the

cooling water in the torch, and in the nozzle respectively; ΔT_t , ΔT_n [K] are the temperature jump in the torch and nozzle cooling system respectively; $\left(T_{fg} - T_g^i\right)$ is the inlet temperature of the gas less the reference temperature for enthalpy calculation.
The mixture composition is 80 % N_2 and 20%O_2 to simulate air composition. Fundamental measured parameters of the tests are typically:
1) Mass flow rate
2) Arc voltage and current (e.g. electric power)
3) Exit nozzle and test chamber pressure
4) The power subtracted by the cooling system
Fig. 13 shows the SPES facility image and Fig. 14 shows the arc heater.

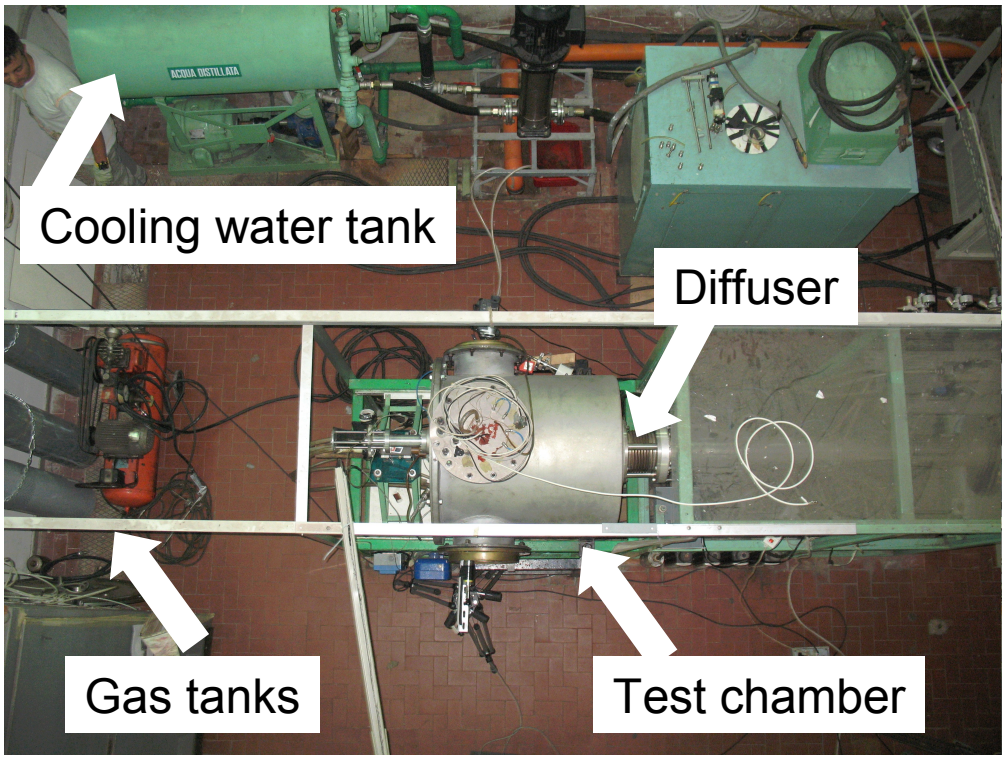

Fig. 13. SPES experimental setup.

Fig. 14. SPES arc heater pressure probe in the flux.

The gas used for the experimental test is contained in high pressure tanks (about 220 bar), it is fed up to the torch at a pressure about 1 bar, and it flows between the blow-down arc electrodes, between the

electrodes the electric arc warms up the gas at a temperature up to 15000K, depending on arc power and mass flow rate. The mass flow, after the torch exit, is mixed with oxygen in the mixing chamber. The mixture expands through a convergent-divergent nozzle (area ratio = 4 , for the nozzle with nominal mach number = 3) and it arrives in a cylindrical test chamber with about 1 m diameter and length (Fig. 15).

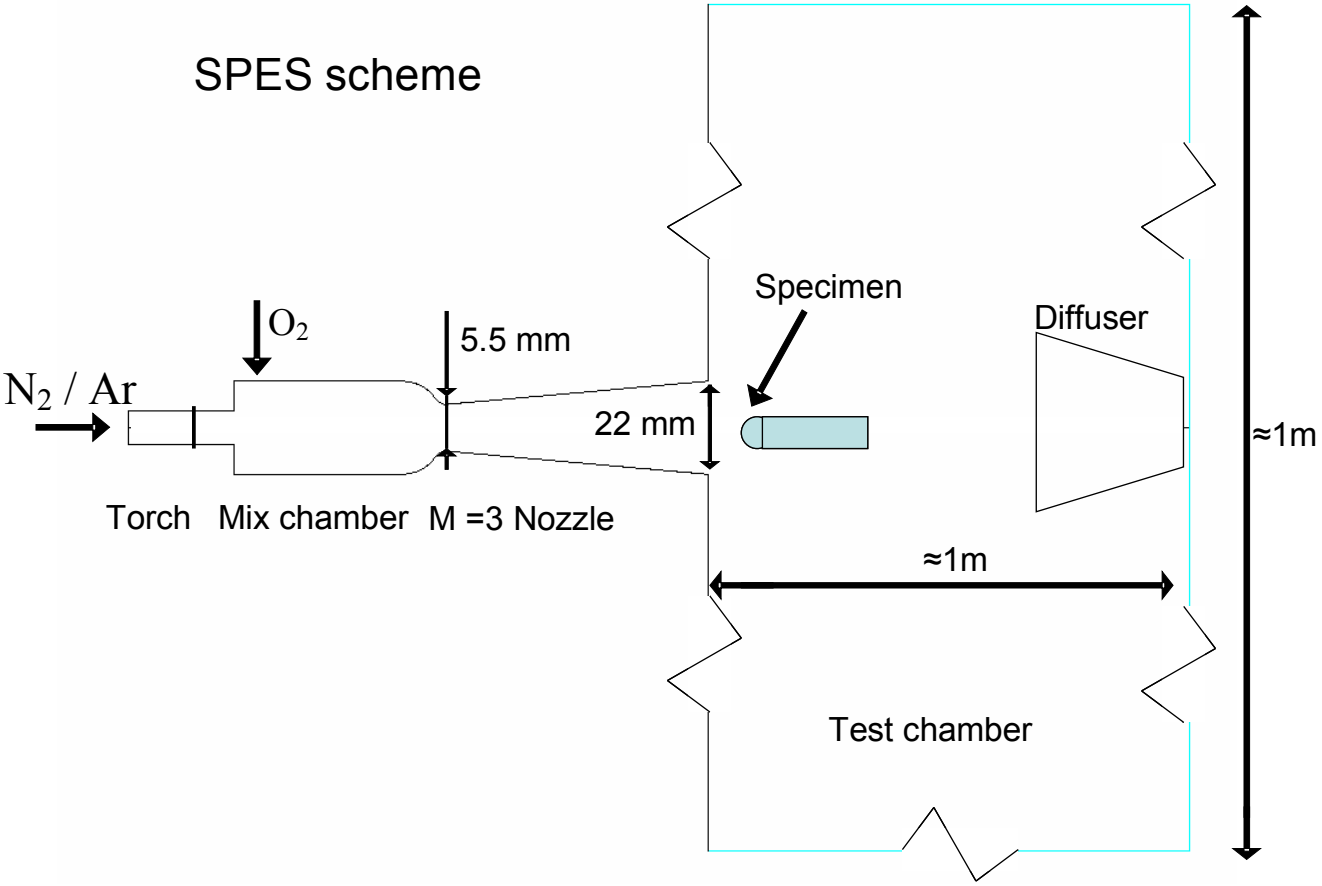

Fig. 15. SPES scheme.

The test chamber has three circular windows to allow the access, the infra-red and optical vision. One of the window is equipped with an infra-red window (transparent in the infra-red wavelength) realized in Barium Fluoride (BaF), while the optical windows are realized in Pyrex-glass. The plasma flow impacts the model that is kept in position by a mechanical arm. The plasma flow exits the test chamber throughout a water cooled diffuser that reduces the flow velocity to subsonic values. With an arc power up to 29 kW, the facility configuration allows long lasting test up to 20 minutes. For the details of SPES facility components see ref. [18].
The Fig. 16 and 17 show the standard set-up for the specimen in the test chamber.

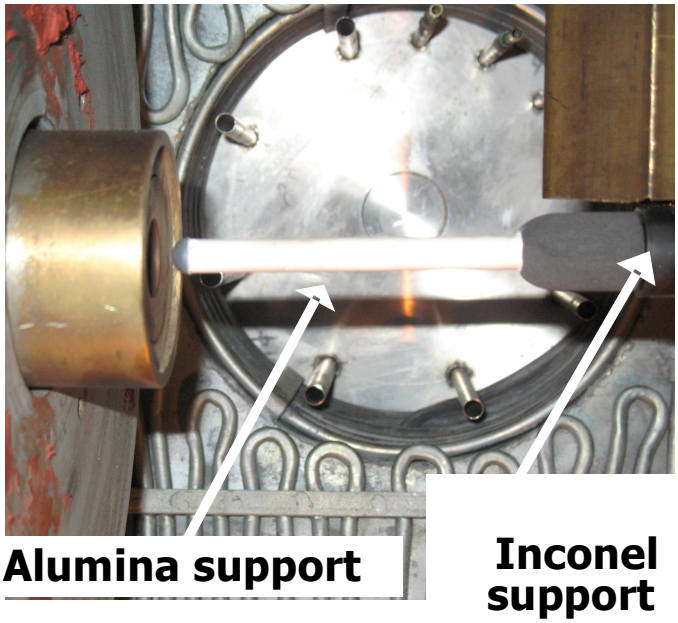

Fig. 16. The test chamber standard set-up.

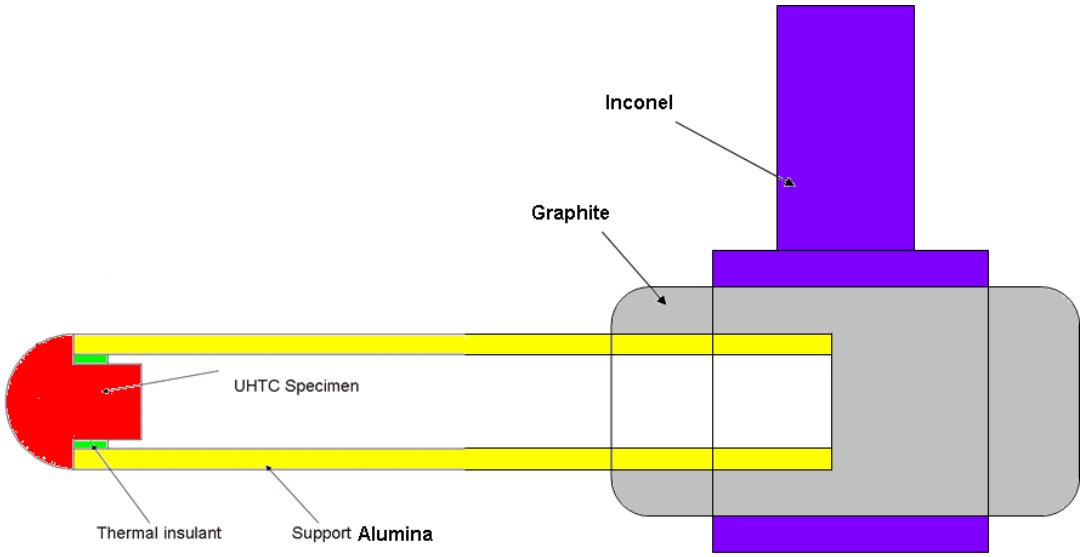

Fig. 17. The section support sketch.

The specimen is fitted in an alumina pipe, the alumina tube is inserted in a graphite joint which is inserted in the inconel support arm connected to the chamber wall. A thermal insulator is interposed between the specimen handle and the alumina support (Fig. 17).
The thermal properties of the support materials are shown in Tab. 2.

	Graphite	Inconel	Alumina	Thermal Insulant
ρ , kg/m^3	2100	8200	3900	400
c_p, J/kgK	710	444	881	469
K,W/mK	85	7	30	0.15

Tab. 2 Thermal properties of the support's elements

III.2. The diagnostic setup

During the experiments, infra-red and optical windows in the test chamber allow visual inspection and diagnostic analyses. A thermocam, and a two colour pyrometer provide the evaluation of the surface temperature distribution. Due to the extremely high temperatures and the presence of oxygen in the free stream, oxidation results in changes in the material's surface emissivity. To overcome this problem, the temperature measurements are carried out with a radiation ratio pyrometer (Infratherm ISQ5, Impac Electronic Gmbh, Germany) which operates both in two colour and in single colour mode. In the two colour mode the instrument makes use of the ratio of two spectral radiances, measured at different wavelengths (0.9–1.05 μm), to evaluate the true temperature. This overcomes the problem of the emissivity knowledge. Once the temperature is measured with the ratio pyrometer, its value is utilised to evaluate the spectral emissivity using the single colour function (λ = 0.9 μm), with the following procedure.

The spectral radiance is valued by the Plank's law $q_{rad}(\lambda,T,\varepsilon)=\varepsilon\tau\dfrac{1.19E8}{\lambda^5\left[\exp\left(\dfrac{1.44E4}{\lambda T}\right)-1\right]}\left[\dfrac{w}{m^2\mu m}\right]$

at both the true temperature $q_{rad}[(\lambda_1+\lambda_2)/2,T_1]$, and at the temperature evaluated in the single colour mode $q_{rad}(\lambda_1,T_1)$, thus the product between the emissivity and transmittivity is given by $\varepsilon_1\tau_1=\dfrac{q_{rad}(\lambda_1,T_1)}{q_{rad}\left(\dfrac{\lambda_1+\lambda_2}{2},T_2\right)}$.

In combination with the pyrometer, an infrared thermo-camera (Thermacam SC 3000, FLIR Systems, USA) is used to measure the surface temperature distributions and the spectral emissivity in the long wave range of the thermograph (λ=9 μm). The pyrometer must have a distance from the model from 35 up to 55cm, beyond this limits measurement errors occur. At the distance of 45cm the pyrometer measure the average value of a 3mm radius spot, this implies difficulties in measuring little specimen with dimensions in the order of the spot. The temperature range for the two colour pyrometer is 1273-3273K, the measurement uncertainty is 1% of the measured value, but the repeatability is about 2% due to the uncertainty on the target point. For the temperature measurement, the pyrometer is not affected by angle shot (<40°) of the measured surface, it don't requires the knowledge of material surface emissivity, specimen distance, and air humidity; and the presence of glass porthole has little influence (<3%) on the temperature measurement that can be erased completely by setting in the pyrometer software, the ration correction $k=tr_1\varepsilon_1/(tr_2\varepsilon_2)$ where ε_1 and ε_2 are the emissivity at the two wavelengths (0.9–1.05 μm), and tr_1, tr_2 are the transmittance of the porthole at the two wavelengths.
The thermocam has four temperature ranges from 253 up to 2273K, with an uncertain of the 2% for temperature above 450K. Because this instrument use only one wavelength, the measure depends on the knowledge of material surface emissivity, specimen distance, air humidity; and by the transmission coefficient of glass porthole.

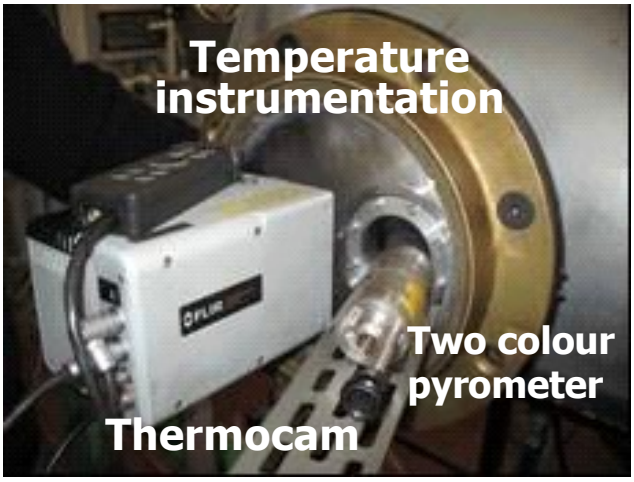

Fig. 18. Thermacam and two colour pyrometer.

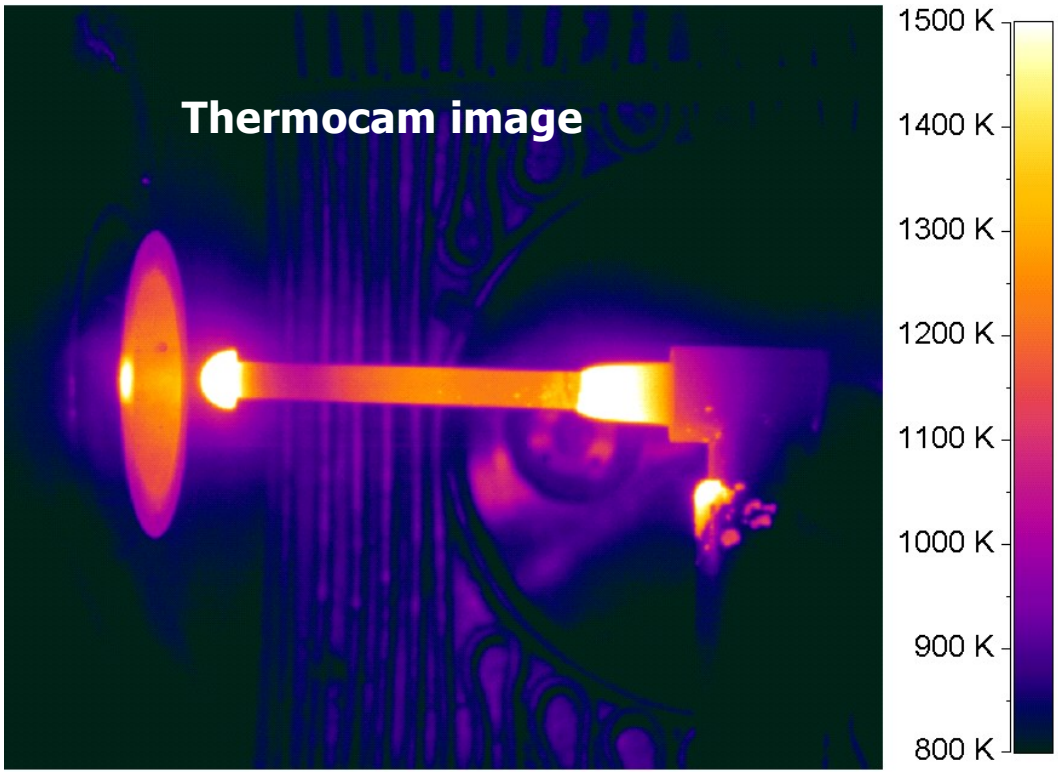

Fig. 19. Thermacam image.

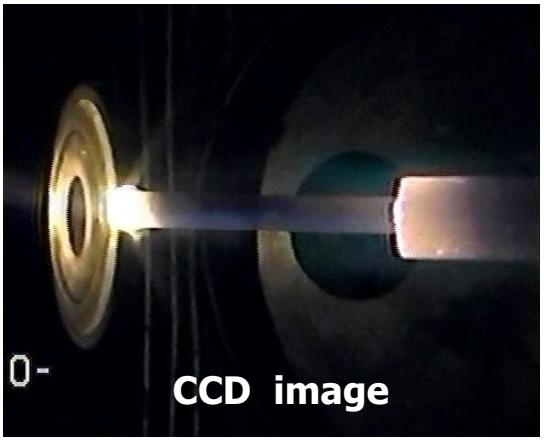

Fig. 20. Camera image of the model in the hypersonic high enthalpy flow.

A CCD camera is used to acquire images of the specimen during the test (Fig. 20).

Chap. IV. The numerical models

In this chapter is described the numerical model used in this work, with some result to show the model behaviour. The numerical results are interrelated with the SPES behaviour and with the tests results, for this reason they will be shown in the next chapters.

IV.1. The CFD for arc-jet testing

Up to 40 years ago there were only three methods to project the air-planes, and the space vehicles: the theoretic solutions, the wind tunnel testing, and the in-flight testing. The develop of digital computing has allowed the numerical integration of the full balance equations of energy mass and momentum. But only in the last 25 years the incoming of fast and low cost computers has provided for the diffusion and the develop of numerical computation, with the born of a new subject: the computing fluid dynamics (CFD). Thus there is a new instrument to study the space vehicles: the computing fluid dynamics.

The CFD has became fundamental for aerodynamics study, allowing the saving of a lot of wind tunnel and in-flight tests; for example during the development phase of the F16 airplane in the half of ’70 there come out an aerodynamic problem of the wing geometry that was able to require dozens of wind tunnel and in-flight testing, but the use of CFD permitted the saving of about 5 million of dollars [19].

Today there are a lot of commercial numerical code for CFD analysis, with an user friendly interface. This codes can be used also by people with very little informatics and programming skills, but can not be used by people who do not know the problem very well. It is fundamental the knowledge of the problem details, of the appropriate boundary conditions, of the theoretic and semi-empiric solution about the problem, because like as it is easy to obtain a numerical solution, it is easy to obtain the wrong solutions also.

On a wall of the office, next to my computers there is a picture with a famous phrase shared among CFD practitioners that correctly describes a perceived problem with numerical predictions: “Everyone believes experimental results except the person who performed the experiment, and no one believes numerical results except the person who performed the prediction.” Unfortunately this statement is closer to reality for hypersonics than for other regimes. Also if skilled engineers can obtain useful design information and guidance also from relatively immature models. Often hypersonic CFD predictions becomes difficult because substantial experimental data for a variety of flows and flight conditions are not available easily. Ever measurement is more difficult and expensive in hypersonic than in any other regime, the pressures, the chemical species, the temperatures, and the heat fluxes.

Typically, the equations solved in CFD programs are based on the assumptions that the fluid is a continuum, that the perfect-gas law applies, the chemical kinetic is the same of the standard-batch conditions, and that the only forces are due to pressure, viscous effects, and body forces. The continuum assumption is no longer valid for rarefied gas flows at high altitudes when the mean-free path of the fluid molecules is on the order of the length of the vehicle (Knudsen number >0.2), the other assumptions can lead to additional difficulties. These problems are due to the complex flow features that can occur in hypersonic flow: thin shock layers (high compression), entropy layers caused by highly swept and curved shock waves, viscous/inviscid interactions, and real gas effects, including dissociation, ionization (high temperatures), and rarefication (high altitudes); [20]. Note that rarefication is not an hypersonic problem but is a typical problem of re-entry vehicles. The validity of Navier-Stokes equation (the momentum balance in the continuum) depends on the local Knudsen

number $Kn = \frac{\lambda}{L(x)}$ where λ is the mean flight path and L(x) is the local characteristic length, since x is the distance from the leading edge, this length L(x) tends to zero in the forebody, for this reason the stagnation point solution can be wrong also if in the whole flow field the Navier-Stokes equations are fully valid.

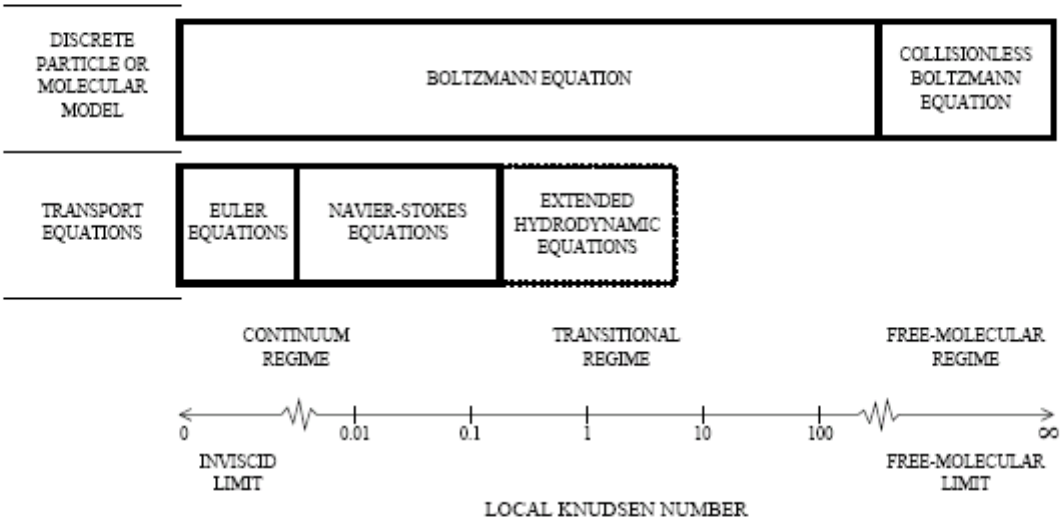

Fig. 21. The Knudsen number limits on the mathematical models [21].

The discrete particle model can be used in every regime (Fig. 21), the Euler equations are the momentum balance Navier-Stokes in inviscid flow with no body forces and in steady state; for $Kn \in [0.2;1]$ the Navier-Stokes equation are valid but could lead to meaning errors.
In the arc jet plasma wind tunnel, object of the present dissertation, the difficulties are increased respect a free stream hypersonic flow, because:

- The presence of plasma in the torch.
- The uncertain on the flow regime, it can be either turbolent or laminar, because the Reynolds number has values between 2000 and 1E6, i.e. in the uncertain interval (Fig. 22).
- The wall boundary condition of the facility can not be known exactly because the wall catalyticity, the wall heat exchange can be function either of the position and of the arc current-mass flow rate ratio.
- There are not reliable experimental data on chemical environment or on wall heat fluxes.
- The arc power can vary from 15 up to 38kW, this can imply the necessity to use different chemical-physical model at different power.

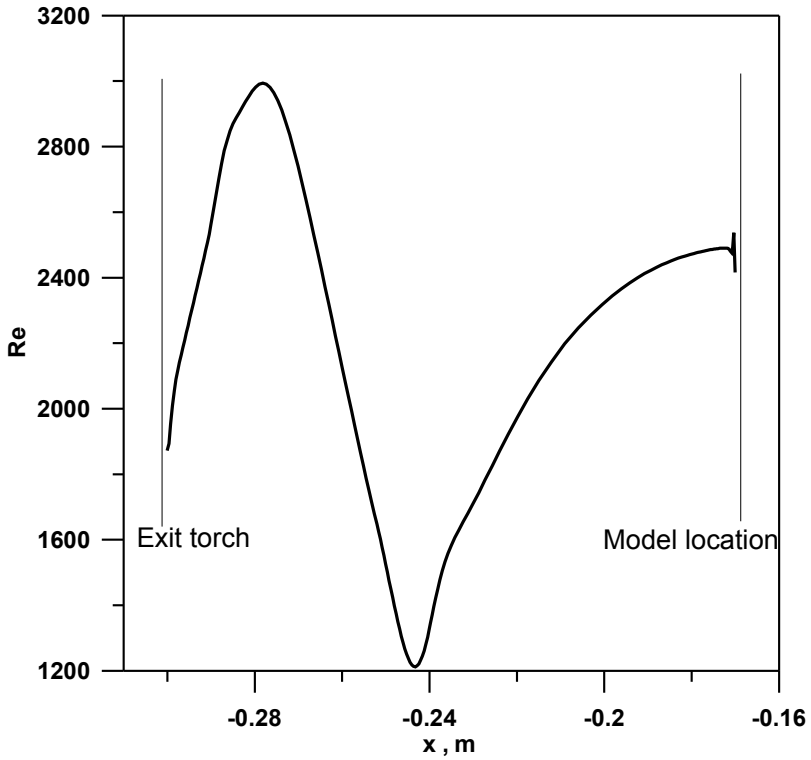

Fig. 22. Reynolds number along the SPES symmetry axis for an arc power of 29kW, an exit nozzle total enthalpy of 15 MJ/kg, and a reference length of 0.022m.

The flow simulations have been performed using a commercial CFD software able to solve the full balance equation system for the selected mixture, at high temperatures in chemical non-equilibrium, in hypersonic conditions, including chemical reactions. A density-based, time implicit, numerical resolution scheme has been used, solving the above field equations through a control-volume-based technique developed on the following three steps:

1. A division of the domain in smaller discrete control volumes using a computational grid is made.
2. Then the equations are integrated in each control volume to construct algebraic equations for the unknown discretized variables.
3. Finally the set of equations are linearized and solved.

Then the variables are updated with the obtained results and the process is repeated until convergence of the solution is obtained. The value obtained by substituting the solutions of the variables in the equations is named residual, the convergence check relies both on the variable values and on residuals value.

A typical grid used to simulate the SPES is in the Fig. 23, the specimen and the support zone is without meshing because the numerical solution in the solid phase is obtained separately from the fluid phase to fastening the global solution. For the same reason of computing time sometimes the fluid flow field around the model is resolved separately from the whole SPES CFD solution (Fig. 24).

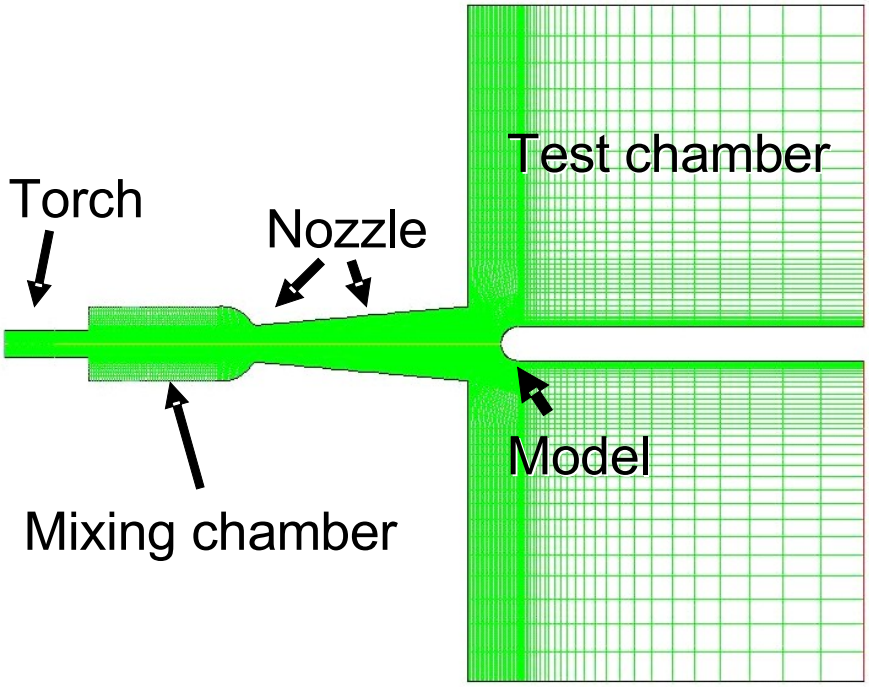

Fig. 23. SPES computational grid with Mach 3 nozzle and hemispheric specimen (R=0.005m).

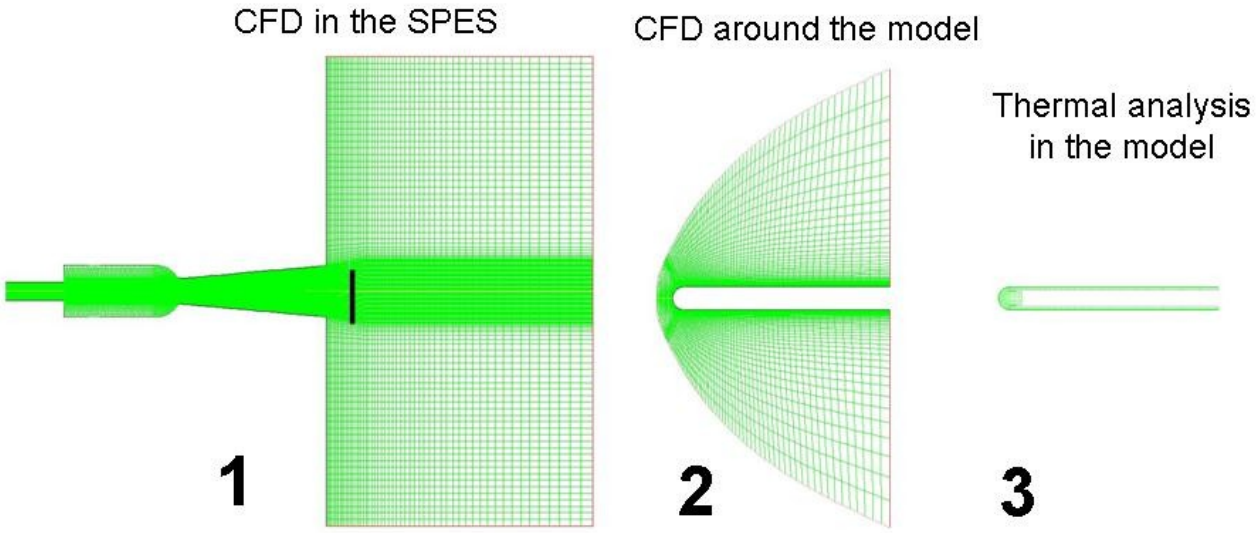

Fig. 24. SPES computational grid with separated grid for CFD solution at model location, and with the grid for thermal analysis solution, the global integration field is divided for fastening the solution.

IV.2. The chemical models

The chemical model tested are three: the Dunn-Kang model with 5 species [22], the Park model with 11 species [23], and the Evans model with 11 species. The models with 11 species include the ions, and the Evans model does not need of the calculation of chemical equilibrium equation to calculate the backward velocity of reaction because within 22 reactions there are the direct and the inverse ones, this model is more stable than the other because do not require the calculation of chemical constant [24,25]. The Park model with 11 species and 23 reactions has been used for the two temperature model.

For the tested cases, the computational time difference between the 11species and 5 species model don't justify the better accuracy of the first one, in fact the calculated pressure, heat flux, and species mass fraction along the hemispheric surface model is similar for both the chemical models. In Fig. 25,26,27,28 there are the wall heat flux, the pressure, and species mass fraction for the hemispheric model in the SPES equipped with Mach 3 nozzle, the specimen is located at 1cm from exit nozzle, the arch power is 25kW, and the mass weighted average total enthalpy at exit nozzle is (H_0) 11,6MJ/kg. The plotted conditions refer to average values for the SPES facility. Note in Fig. 27 and Fig. 28 the different profiles for the oxygen and the nitrogen, but the average mass fraction is similar (for oxygen) or very close (for nitrogen), this two species mass fractions are particularly important because the catalyticity calculation. The 11 species model is needed only for ion and plasma study of the arc-jet facility, and for the study of the two temperature model. The highest ion mass fraction at the exit nozzle is resulted to be smaller than 5E-5, in the worst case of 36kW arc power.

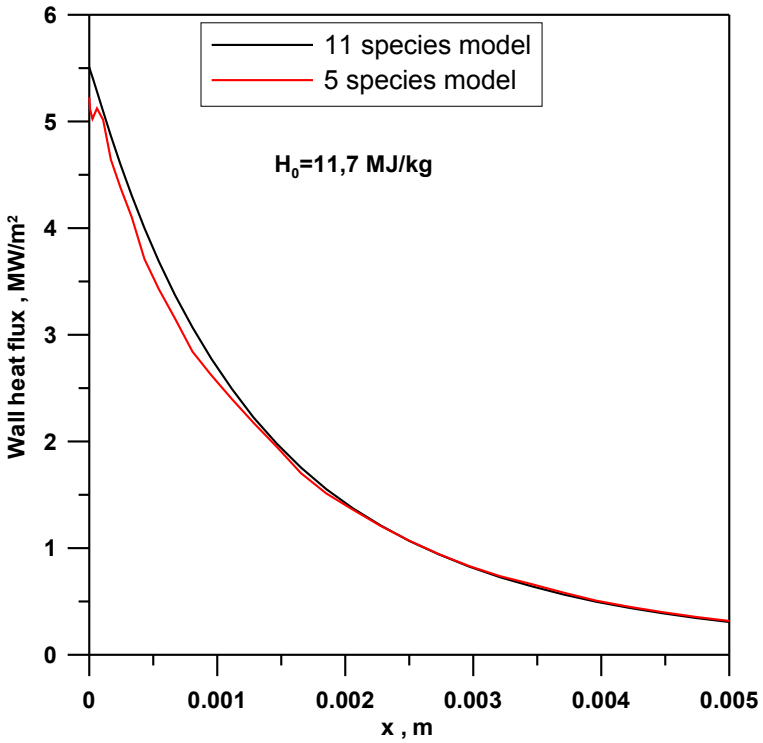

Fig. 25. The wall heat flux for the hemispheric specimen in the SPES with an exit nozzle H_0= 11,6MJ/kg.

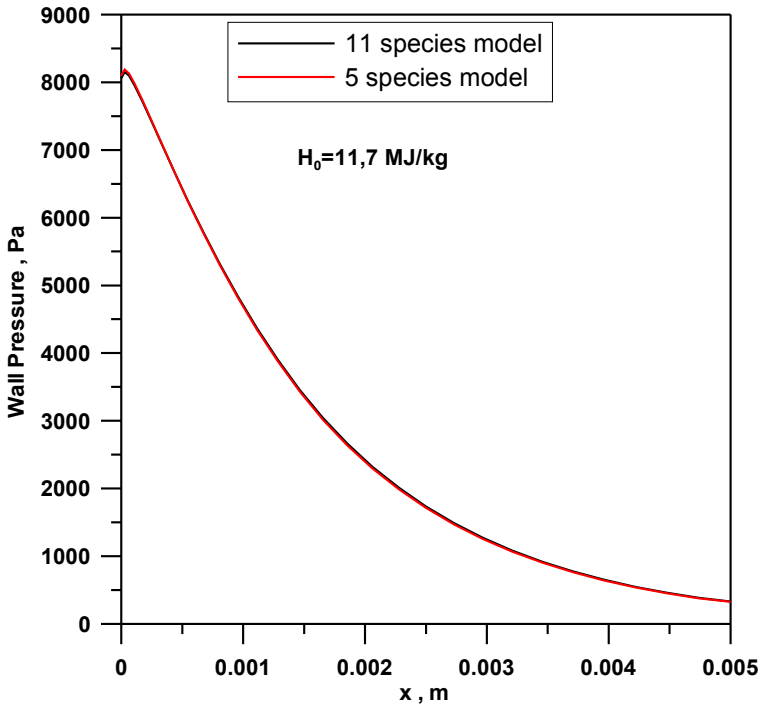

Fig. 26. The wall pressure for the hemispheric specimen in the SPES with an exit nozzle H_0= 11,6MJ/kg.

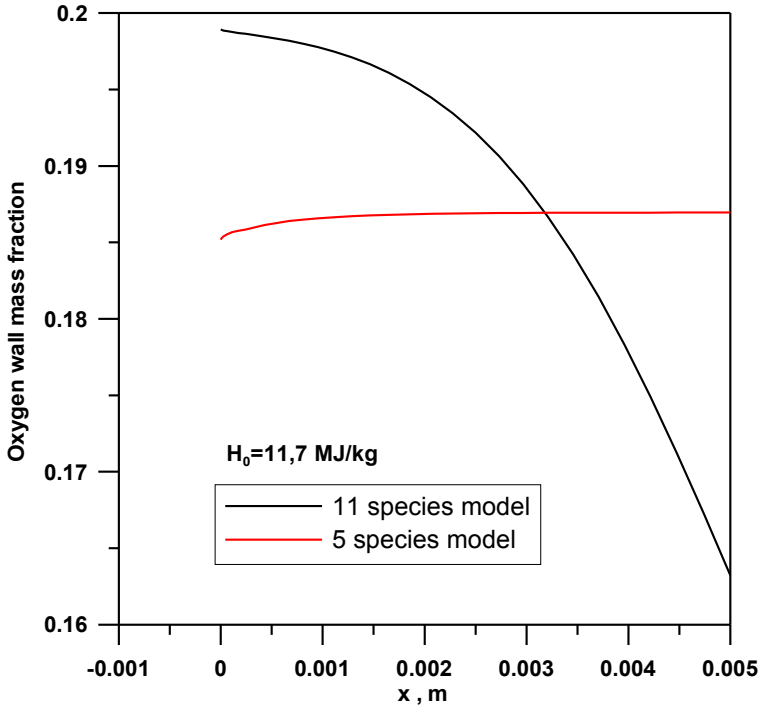

Fig. 27. The oxygen mass fraction on the hemispheric specimen in the SPES with an exit nozzle H_0= 11,6MJ/kg.

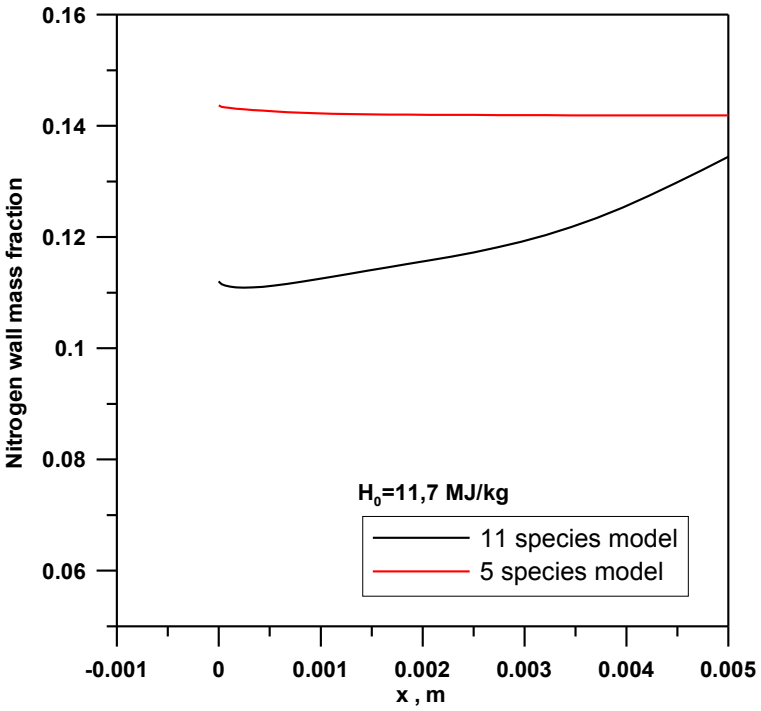

Fig. 28. The oxygen mass fraction on the hemispheric specimen in the SPES with an exit nozzle H_0= 11,6MJ/kg.

IV.3. The thermal non equilibrium model

The effects of the thermal non-equilibrium can be important in the plasma wind tunnels [1]. The vibration energy became not negligible for temperature above the 800K. When the electric discharge span the gas in the arc, the electrical energy is transformed in: electronic energy (excitation of the electron), in vibrational energy (only for the diatomic molecules), in translational energy, and in chemical energy. In Fig. 29 there are the roto-translational, vibrational and electronic specific energy Vs. temperature for oxygen, the maximum temperature indicated is 4000K because in chemical equilibrium,at 4000K and 1E5 Pa the oxygen is totally dissociated. By the second law of thermodynamic this energy is transferred between the various states until an equilibrium is not achieved; usually if the characteristic time of the energy exchange is lower than the convective characteristic time the thermal equilibrium is verified, but in some cases when the total enthalpy is about 30 MJ/kg, and the gas velocity is up to 3000 m/s (i.e. the standard conditions at the exit of the torch of the SPES), the thermal non-equilibrium can be verified. In the thermal non-equilibrium case two or more temperatures are required to represent the energy level of the flow. In literature a two temperature model is defined sufficient for a lot of cases [1], one temperature represent the translational-rotational energy, another one temperature represent the vibroelectronic energy status. Several chemical reactions depend on the translation temperature, some other one depend on the vibroelectronic temperature, and some depends on a combination of both the temperatures. A calculation of characteristic time of vibration in the SPES torch and mix chamber has shown that the characteristic time of vibration is of the same order of the convective time, for this reason the thermal non-equilibrium can be important.

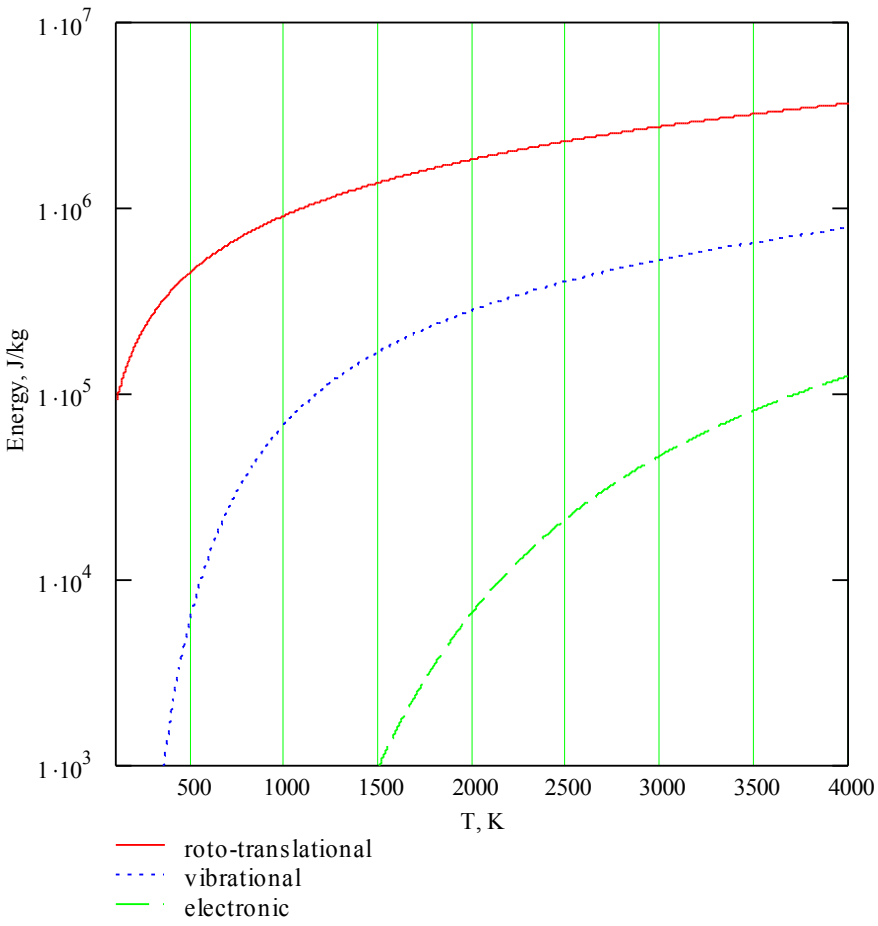

Fig. 29. The roto-translational, vibrational and electronic specific energy Vs. temperature for the oxygen.

The implementation of a two temperature model has been done to verify if an improvement of the standard SPES model was possible.
The two temperature numerical model is constituted by the following system of equations.
The material balance on the i-species

$$\rho \frac{D(\alpha_i)}{Dt} = \vec{\nabla} \cdot (\rho D_{i,mix} \vec{\nabla} \alpha_i) + M_i R_i \qquad \frac{Kg}{sm^3}$$

$D_{i,mix}$ diffusion coefficient of the i-element in the mixture $\frac{m^2}{s}$, M_i molecular weight of the i-species $\frac{kg}{kmol}$, ρ is the mixture density $\frac{kg}{m^3}$, α_i is the mass fraction, $\vec{\nabla}$ is the del operator = $\frac{\partial}{x}\hat{i} + \frac{\partial}{y}\hat{j} + \frac{\partial}{z}\hat{k}$ in Cartesian coordinate $\frac{1}{m}$. α_i is the mass fraction of the i-species.

The net reaction velocity R_i is the sum of all the direct and inverse reaction rate of the i-species in every r-reaction in which is included:

$R_i = \sum_r \left(R_{d_{i,r}} - R_{i_{i,r}} \right)$ $\frac{kmol}{m^3 s}$ the sum is on all the reactions, the direct velocity is $R_{d_{i,d}} = k_{f,r} \prod_{j=1}^{N_r} \left[C_{j,r} \right]^{\eta^I_{j,r}}$

$C_{j,r}$ molar concentration of specie j $\frac{Kmol}{m^3}$, the product is over all the j-species involved in the r-reactions. $\eta^I_{j,r}$ forward rate exponent for each reactant and product, in the elementary reactions it coincides with the stoichiometric coefficient of the species j in the reaction r, N_r number of reactant involved in the direct reaction r. $k_{f_r} = AT^{\beta} \exp\left(\frac{-E}{RT} \right)$ is the forward rate constant for the reaction r, E is the activation energy $\frac{J}{Kmol}$, β is the temperature exponent, R is the universal constant of the gas $8314 \frac{N}{m^2} \cdot m^3 \cdot \frac{1}{Kmol \cdot K}$, A the pre-exponential factor has the dimensions which depend on the specific reaction, $k_{b_r} = \frac{r_{d_{i,k}}}{K_{eq}}$ is the backward rate constant. $K_{eq} = \exp\left(\frac{-\Delta G}{RT} \right)$ is the equilibrium constant, $\Delta G = \Delta H - T\Delta S$ is the Gibbs free energy variation involved by the reaction $\frac{J}{kg}$. For $r_{d_{i,k}}$, $r_{i_{i,k}}$, and K_{eq} the units depend on the specific reaction.

The chemical kinetic model involve 23 reactions, 11 species, and three temperatures [26].

The matrix with the reaction coefficient is in Tab. 3.

reaction #	reactant	prodoucts	temperature	A	β	E
1	O2+M	O+O+M	Ta	2.00E+18	-1.5	4.95E+08
2	N2+M	N+N+M	Ta	7.00E+18	-1.6	9.41E+08
3	O+ +e-	O	Tv	1.07E+08	-0.52	0
4	NO+M	N+O+M	Ta	5.00E+12	0	6.28E+08
5	NO+O	N+O2	Tt	8.40E+09	0	1.62E+08
6	N2+O	NO+N	Tt	6.40E+14	-1	3.19E+08
7	N+O	NO+ +e-	Tt	8.80E+05	1	2.65E+08
8	O+O	O2+ +e-	Tt	0.71	2.7	6.70E+08
9	N+N	N2+ +e-	Tt	44000	1.5	5.61E+08
10	N+ +N2	N2+ +N	Tt	1.00E+09	0.5	1.01E+08
11	O+ +N2	N2+ + O	Tt	9.10E+08	0.36	1.90E+08
12	O2+ +O	O+ + O2	Tt	4.00E+09	0.09	1.50E+08
13	NO+ +O2	O2+ + NO	Tt	2.40E+10	0.41	2.71E+08
14	O2+ +N	N+ +O2	Tt	8.70E+10	0.14	2.38E+08
15	O2+ +N2	N2+ +O2	Tt	9.90E+09	0	3.38E+08
16	NO+ +O	N+ +O2	Tt	1.00E+09	0.5	6.42E+08
17	O+e-	O+ + 2e-	Tv	3.90E+30	-3.78	1.32E+09
18	N+e-	N+ +2e-	Tv	2.50E+31	-3.82	1.40E+09
19	NO+ +N	O+ +N2	Tt	3.40E+10	-1.08	1.06E+08

20	NO+ +N	N2+ +O	Tt	7.20E+10	0	2.95E+08
21	O+NO+	N + O2+	Tt	7.20E+10	0.29	4.40E+08
22	O+ +NO	N+ +O2	Tt	140	1.9	2.21E+08
23	N+ + e-	N	Tv	1.52E+08	-0.48	0

Tab.3. The reaction rate coefficient for Park 11 species model.

The third body efficiency η for the reactions, are in Tab. 4, note the same efficiency for a species and the ionised species:

Species	Reaction		
	1	2	4
O2	1	1	1
O	5	4.286	22
N2	1	1	1
N	5	4.286	22
NO	1	1	22
N2+	1	1	1
N+	5	4.286	22
O2+	1	1	1
O+	5	4.286	22
NO+	1	1	22
e-	0	0	0

Tab. 4. The third body efficiency for Park 11 species model.

Assuming an quasi electric and magnetic neutrality, and the absence of electrical macroscopic current, the diffusion coefficient for the electron and for ì-species in the mixture are given by:

$$D_{e-,mix} = \sum_{i=ion}^{5} \frac{y_i D_{i,mix}}{\sum_{j=ion}^{5} D_{j,mix}} \qquad D_{i,mix} = \frac{1-y_i}{\sum_{j=0}^{10} D_{i,j}} \qquad \frac{m^2}{s}$$

y_i is the molar fraction, $D_{i,j}$ is the binary diffusion, and is given by [27]:

$$D_{i,j} = \frac{1}{P} \pi\Omega_{i,j} \frac{\ln\left[2.09e-2\left(\frac{T}{1000}\right)^4 + 1.52\left(\frac{T}{1000}\right)^{\frac{8}{3}}\right]}{\ln\left[2.09e-2\left(\frac{T}{1000P_{e-}}\right)^4 + 1.52\left(\frac{T}{1000P_{e-}}\right)^{\frac{8}{3}}\right]} 1e-4 \qquad \frac{m^2}{s}$$

$\pi\Omega_{i,j}$ is the collisional integral between the species i and j, given by :

$$\pi\Omega_{i,j} = e^{D_{i,j} T^{A_{i,j}(\ln T)^2 + B_{i,j}(\ln T) + C_{i,j}}} 1E-20 \qquad m^2$$

The coefficient A, B, C, D, are given by [27] for all the 66 possible collisions in the air mixture with 11 species, the temperature used is the roto-translation temperature.
The momentum balance equation is given by:

$$\rho \cdot \frac{D(\vec{v})}{Dt} = \vec{\nabla} \cdot (\mu_{mix}((\vec{\nabla}\vec{v})^S - \frac{1}{3} \cdot \vec{\nabla} \cdot \vec{v} \cdot \overline{\overline{I}}) - \overrightarrow{\nabla P} \qquad \frac{N}{m^2}$$

$\vec{v}$ is the velocity vector $\frac{m}{s}$, μ_{mix} is the effective viscosity of the mixture, P is the pressure Pa, $(\vec{\nabla}\vec{v})^S$ is the symmetric part of the tensor $(\vec{\nabla}\vec{v})$, $\overline{\overline{I}}$ is the identity matrix.

Because the necessity of two temperatures to describe the energy status of the system, two energy balances are needed.
The balance of roto-translation energy is:

(3)
$$\rho \frac{D\left[\left(\sum_i \alpha_i e_{t,i}\right) + \frac{v^2}{2}\right]}{Dt} = \vec{\nabla} \cdot \left(\overline{\overline{\tau}}_D \cdot \vec{v}\right) - \vec{\nabla} \cdot (\vec{v}P) + \vec{\nabla} \cdot \left(k_{mix} \cdot \vec{\nabla} T\right) + Q^{VT} + Q^{he-} + \rho \sum_i R_i \alpha_i e_{t,i} \qquad \frac{j}{m^3 s}$$

The roto-translation energy of the i-species is $e_{t,i} = c_{p_i}(T - T_f)$ where $c_{p_i} = \frac{3}{2}R$ for the atoms, and $c_{p_i} = \frac{5}{2}R$ for the molecules, it is important to use the specific heats of the kinetic theory because they include only the roto-translational energy, instead the polynomial specific heat include also the others type of energy, in fact at temperatures above 1000K the polynomial specific heat results higher than kinetic theory specific heat. x_i is the molar fraction of the i-species, k_{mix} is the thermal conductivity of the mixture, $\overline{\overline{\tau}}_D$ is the deviatoric part of the stress tensor.

$Q^{he-} = 3R\rho_{e-}(T_t - T_{e-})v_{m_{e-}} \sum_{i \neq e-} \frac{\rho_i Na}{M_i^2} \sigma_{e-,i}$ is the exchange between the translational energy of the electron and the energy of the heavy particles [28,29]. $T_{e-} = \frac{e_{e-}}{c_{ve-}} = \frac{c_{ve-} T_{VE}}{c_{ve-}} = T_{VE}$ i.e. the electron temperature is assumed be coinciding with the vibro-electronic energy. Na is the Avogadre number.
$v_{m_{e-}}$ is the average translational velocity of the electron $v_{m_{e-}} = \sqrt{\frac{8RT_V}{\pi M_{e-}}} 0.01 \qquad \frac{m}{s}$; $\sigma_{e,-j} = \pi\Omega_{i,j}$

is the collitional cross section among the electron and heavy particles. Q^{VT} is the energy exchange between vibro-electronic energy and the roto-translational energy, by the Landau-Teller model: $Q^{VT} = \sum_i \rho_i \left(\frac{e_{VEi}(T) - e_{VEi}(T_{VE})}{\tau_i} \right) \qquad \frac{j}{m^3 s}$

The vibrational relaxation time for the i-species is: $\tau_i = \dfrac{\sum_i \dfrac{x_i}{M_i}}{\sum_j \dfrac{x_j}{M_j}\dfrac{1}{\tau_{i,j}}}$ s

The modified vibrational relaxation time [30,31], of the i-element respect to the collisional partner is: $\tau_{i,j} = \tau_{MW_{i,j}} + \dfrac{1}{\sigma_v n_{i,j} v_{m_i}}$ s, where σ_v is the collition limited vibrational cross section a function of translation temperature (Park 1994) : $\sigma_v = \sigma_v^I \left(\dfrac{50000}{T}\right)^2 1e-4 \qquad m^2$

$\sigma_v^I = 1e-17 \quad m^2$ is the collision limited vibrational cross section at 50000K. $v_{m_i} = \sqrt{\dfrac{8RT}{\pi M_i}} 0.01 \ \dfrac{m}{s}$ is the molecular average velocity.
The number of colliding particles i-j in one cubic meter is è:
$n_{i,j} = \rho Na \left(\dfrac{v_{m_i}}{M_i} + \dfrac{v_{m_j}}{M_j}\right) \qquad \dfrac{1}{m^3}$

The relaxation time is (Millikan and White formula [32]) :
$\tau_{MW_{i,j}} = \exp\left[a\left(T^{-\frac{1}{3}} - b\right) - 18.421\right]$ atm s

a and b are two coefficients: $a = 0.0016\left(M_{i,j}\right)^{0.5}\left(v_{v_i}\right)^{1.333} \qquad b = 0.015\left(M_{i,j}\right)^{0.25}$

$M_{i,j}$ is named the reduced molecular weight: $M_{i,j} = \dfrac{M_i M_j}{M_i + M_j} \qquad \dfrac{Kg}{Kmol}$, v_{v_i} is the vibrational characteristic temperature of the i-species

The balance of the vibro-electronic energy is:

(4) $\rho \cdot \dfrac{D(\sum_i \alpha_i e_{VE_i})}{Dt} = \vec{\nabla} \cdot (\mu_{mix} \vec{\nabla}(\sum_i \alpha_i e_{V_i}) - \sum_i \alpha_i e_{VE_i} v_{dif_i}) - Q^{VT} - Q^{he} + \rho \sum_i \alpha_i R_i e_{VE_i} \qquad \dfrac{j}{m^3 s}$

Where $e_{VE_i} = e_{E_i} + e_{V_i}$ is the specific vibroelectronic energy for the i-species $\dfrac{j}{kg}$,

$\mu_{mix} \vec{\nabla}(\sum_i \alpha_i e_{V_i}) \qquad \dfrac{j}{m^2 s}$ is the vibration conductive flux [33]

$\sum_i \alpha_i e_{VE_i} v_{dif_i} \qquad \dfrac{j}{m^2 s}$ is the diffusive flux of vibration energy [33]

$$v_{dif_i} = -\frac{1}{\alpha_i}\left(\frac{1-\alpha_i}{\sum_{j\neq i}\frac{y_i}{D_{i,j}}}\right)\frac{m}{s}$$ diffusion velocity of the i-species [33]

The vibration and electronic energy for the i-species at the T Temperature [33]:

$$e_{v_{i,T}} = \frac{R}{M_i}\left(\frac{\nu_{v_i}}{e^{\frac{\nu_{v_i}}{T}}-1}\right)\frac{j}{Kg} \qquad e_{E_{i,T}} = \frac{R}{M_i}\left(\frac{\nu_{e1_i} g_{1_i} e^{\frac{-\nu_{e1_i}}{T}} + \nu_{e2_i} g_{2_i} e^{\frac{-\nu_{e2_i}}{T}}}{g_{0_i} + g_{1_i} e^{\frac{-\nu_{e1_i}}{T}} + g_{2_i} e^{\frac{-\nu_{e2_i}}{T}}}\right)\frac{j}{Kg}$$

This energies are function of the temperature, the molecular weight (M_i),the characteristic vibrational (ν_{v_i}), and electronic temperatures (ν_{e1_i} , ν_{e2_i}). The values of the different energies for the oxygen are in Fig. 29.

formula	M[Kgr/Kmol]	T Vibr [K]	T elet1 [K]	T elet2 [K]	g0	g1	g2	h0[j/Kmol]	s0[j/(KmolK)	Cp[j/molK]	L-J-l [Å]	L-J-e [K]	l1[j/Kmol]
o2	32	2239	11390	18960	3	2	1	0	205026.86	20.785	3.458	107.4	1.20697E+08
o	16	non vibra	228	326	5	3	1	2.49E+08	160932.56	12.471	2.75	80	6.03485E+07
no+	30	3482	28715	44503	1	3	6	9.85E+08	210760	20.785	3.47	119	
n	14	non vibra	28000	41500	4	10	6	4.71E+08	153192	12.471	3.298	71.4	5.28049E+07
no	30	2817	174	63123	2	2	2	9.03E+07	210760	20.785	3.47	119	1.13153E+08
n2+	28	3177	1.00E+05	0.00E+00	1	0	0	1.50E+09	191494.78	20.785	3.681	91.5	
n+	14	non vibra	28000	41500	4	10	6	1.88E+09	153192	12.471	3.298	71.4	
o2+	32	2691	11390	18960	3	2	1	1.16E+09	205026.86	20.785	3.458	107.4	
o+	16	non vibra	228	326	5	3	1	1.57E+09	160932.56	12.471	2.75	80	
e-	0.0005	non vibra	0	0	0	0	0		0	5.46E-07			
n2	28	3395	1.00E+05	0	1	0	0	0	191494.78	20.785	3.681	91.5	1.05610E+08

Tab. 5. The characteristic vibrational and electronic temperatures, the number of states present at every electronic energy level (g_0, g_1, g_2), the formation enthalpy and entropy, the specific heat calculated by the kinetic theory, and the Lennard-Jones parameters.

In the Tab.5 There are the characteristic vibrational and electronic temperatures, the number of states present at every electronic energy level (g_0, g_1, g_2), the formation enthalpy and entropy, the specific heat calculated by the kinetic theory, and the Lennard-Jones parameters for the 11 species of the model.

The electronic and vibrational energy is subtracted from the enthalpy in the torch, in the mixer chamber and in the nozzle it is given back but only partially. In Fig. 30 there is the vibro-electronic energy source term along the axis of the torch, the mix chamber, and the nozzle, for an arc power of 22kW, and mass flow rate of 1g/s. The negative value implies an increasing of the vibro-electronic energy, that increases in the torch and decreases in the mix chamber and in the nozzle.

In the divergent part of the nozzle the vibro-electronic energy doesn't decrease because this energy can be considered frozen (Fig. 31), in fact the convective time is short respect to the vibrational relaxation time.

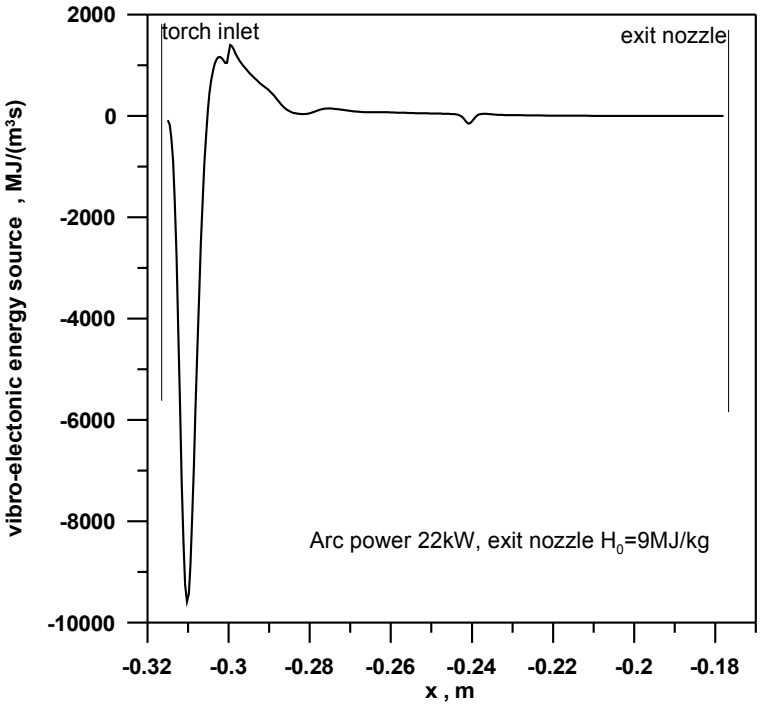

Fig. 30. Vibro-electronic energy source term along the axis of the torch, the mix chamber, and the nozzle of the SPES.

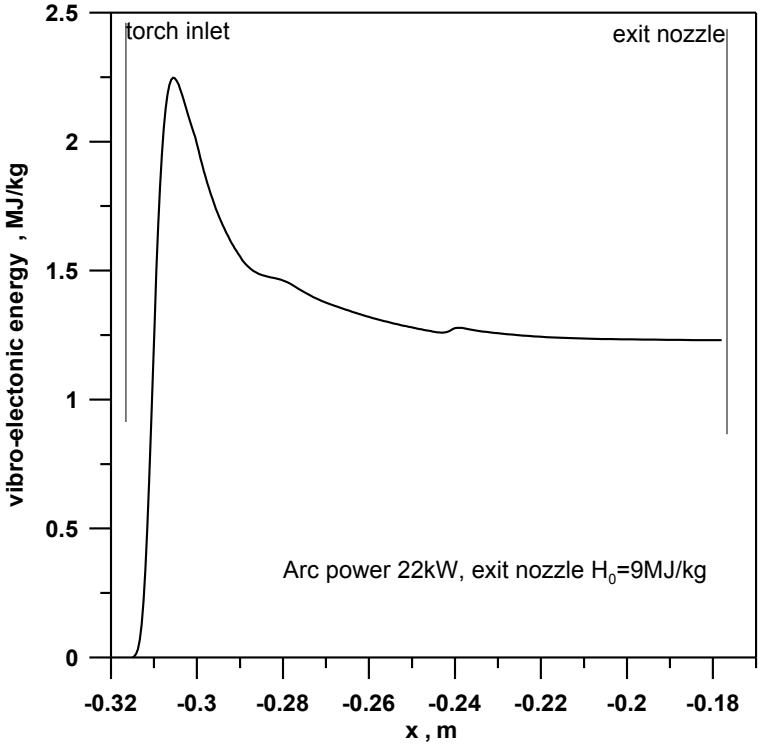

Fig. 31. Vibro-electronic energy along the axis of the torch, the mix chamber, and the nozzle of the SPES.

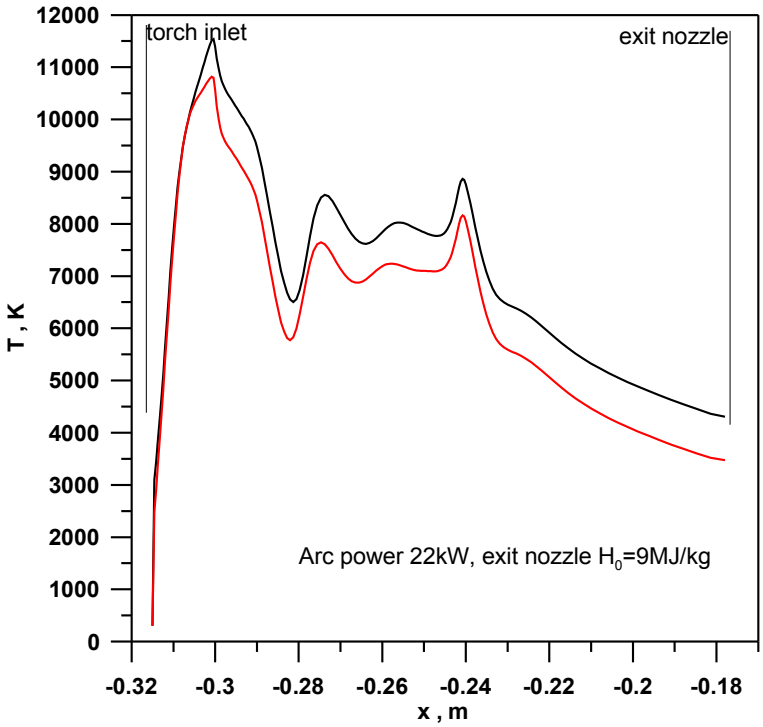

Fig. 32. Roto-translation temperature for the model with two temperature and for the model with one temperature along the axis of the torch, the mix chamber, and the nozzle of the SPES; the roto-translational temperature for the two temperature model is lower than the temperature of the one temperature model.

In the Fig. 32 there is the roto-translation temperature for the model with two temperature and for the model with one temperature along the axis of the torch, the mix chamber, and the nozzle of the SPES. The roto-translational temperature for the two temperature model is lower than the other one model because the vibro-electronic energy aliquot is subtracted at the roto-translational energy. For the two temperatures model is assumed that the vibro-electronic energy is at the equilibrium at the arc inlet and at test chamber outlet, but isn't clear if there is equilibrium on the model's surface, for this reason is not clear which amount of the vibro-electronic energy contribute to the thermal heating.

In the case of non thermal equilibrium at the specimen wall, the heat flux is $q_w \propto H_0 - H_{vibration-electronic}$ where H_0 is the total enthalpy in MJ/kg, and $H_{vibration\text{-}electronic}$ is the vibro-electronic energy. As shown in Fig. 31 the vibro-electronic energy is about the 20% of the total enthalpy, because the wall heat flux depends on the enthalpy and the square root of the pressure, and because the vibrational energy presence reduces this two values, the two model temperature results in lower pressure and thermal heating than the standard model, unless there is thermal equilibrium on the model surface.

The 11 species model with two temperatures requires long calculation times respect to the five species and one temperature model. Due to the presence of complicated user defined functions the two temperature model with 11 species is also difficult to converge at the solution. For this reason the model to correlate the experiment in the present work does not include the vibro-electronic energy.

Although it must be recognised the better accuracy of the 11 species model with two temperatures than the others, large studies must be conducted for a correct implementation of this model.

IV.4. The thermal heating analysis

The thermal field in the specimen is resolved separately from the CFD field for fastening the solution.

The numerical solution in the solid field implies the solution of only the energy balance in the cells of the computational grid. The standard grid for the solid models has about 1000 cells, only few minutes are needed to obtain the solution.

The energy equation is: $\rho_s c_p \frac{\partial T}{\partial t} - \mathrm{k_s}\overline{\nabla}^2 T_s = 0$ $\mathrm{k_s}$ is the thermal conductivity $\frac{W}{mK}$, ρ_s and $\mathrm{c_p}$ are the density and specific heat of the solid material. The boundary condition at the non catalytic surface is $\left(-\mathrm{k}\frac{\partial \mathrm{T}}{\partial \mathrm{n}} - \rho\sum_{\mathrm{i}} \mathrm{D_i h_i}\frac{\partial \alpha_{\mathrm{i}}}{\partial \mathrm{n}}\right)_{\mathrm{w}} = -\mathrm{k_s}\left(\frac{\partial \mathrm{T}}{\partial \mathrm{n}}\right)_{s,w} + \sigma\varepsilon \mathrm{T_w}^4$ the left hand side of the equation is the incoming wall heat flux due to thermal conduction (Furier law) and material diffusion (Fick law), $\mathrm{h_i}$ is the enthalpy of the ì-species that diffuse at the wall $\frac{J}{kg}$, $\mathrm{D_i}$ is the material diffusion coefficient $\frac{m^2}{s}$. The incoming heat flux is in part conducted in the solid and in part re-irradiated by Stephan-Boltzmann law. The CFD heat flux is calculated at cold wall $\mathrm{q_w(t_0)}$ (300K), and is updated with the time by the formula $q_w(t) = q_w(t_0)\left(1 - \frac{h_w(t)}{H_0(t_0)}\right) - \sigma\varepsilon T(t)^4$, $h_w(t)$ is the wall enthalpy depending on the wall temperature and for this reason on the time t, $H_0(t_0)$ is the total enthalpy of the fluid and doesn't depend on the time, σ is Stephan-Boltzmann constant = 5.67E-8 $\frac{J}{sm^2K^4}$, ε is the global emissivity. Usually the calculated emissivity from the two colour measurement has been approximated as the global emissivity value, because the spectral radiance function Vs. wavelength should have the maximum around μm1, that is the working wavelength of the two colour pyrometer.

The hemispheric axial symmetric model for thermal analysis is shown in Fig. 33, the average temperature in circle spot shown is used as comparison with the experimental pyrometer measurement.

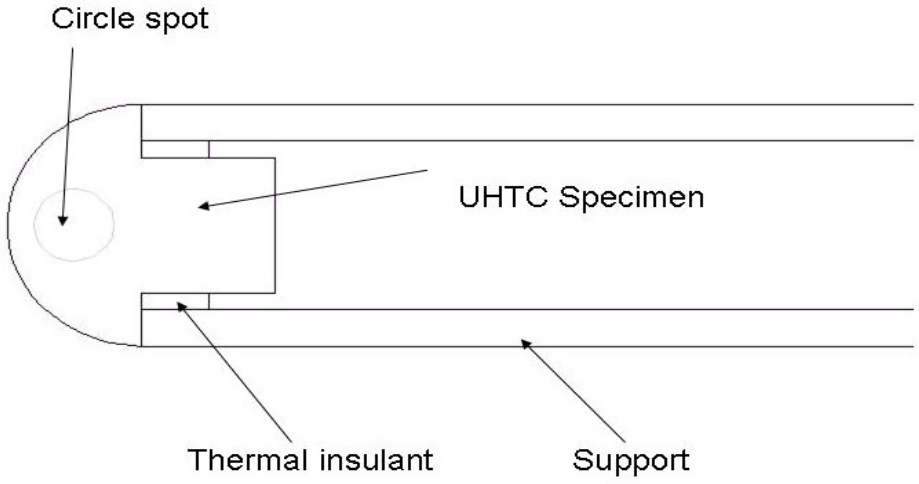

Fig. 33. The hemispheric thermal model.

In several cases the material changing has been keen in account by the thermal model, in fact some material during the warming up changes the chemical composition of a layer on the surface (thikness<200μm), this superficial layer becomes oxidised, changing the its thermal properties, this changing can be important for the overall thermal heating. In such cases the thermal model has a material with the opportune properties on a superficial layer.

IV.5. The selected CFD

The selected CFD model has:

- Chemical non equilibrium with 5species (Dunn & Kang model)
- Convective heat cooling walls
- Non catalytic walls in the SPES's nozzle
- Radiation in the nozzle, mix chamber and the torch
- Turbolent k-ε viscous model

The general fluid dynamic software has been widely validated over a large variety of tests belonging to all arc power regimes, by comparison with experimental data. In particular the attention is focused on the wall heat flux and pressure on the specimen's wall.
The chemical model is in the Tab. 6 and 7.

Reaction #	reactant	prodoucts	A	β	E
1	O2+M	O+O+M	3.61E+15	-1	4.94E+08
2	N2+M	N+N+M	1.92E+14	-0.5	9.41E+08
3	N2+N	N+N+N	4.15E+19	-1.5	9.40E+08
4	NO	N+O	3.97E+17	-1.5	6.29E+08
5	NO+O	O2+N	3.18E+06	1	1.64E+08
6	N2+O	NO+ N	6.75E+10	1	3.12E+08

Tab.6. The reaction rate coefficient for Dunn-Kang model.

Species	Reaction		
	1	2	4
O2	9	1	1
O	25	1	20
N2	1	2.5	1
N	1	0	20
NO	1	1	20

Tab.7. The third body efficiency for Dunn-Kang model.

All boundary conditions for the numerical simulation of the SPES experiments are fundamental. The inlet condition at the torch and at the mixing chamber (Fig. 34) is gas at room condition, i.e. 300K and 10^5 Pa.

The wall of the torch, mix chamber, and nozzle is considered non-catalytic, and the heat exchange is both convective and radiative, the highest thermal fluxes are in the torch and nozzle convergent wall.

The torch is approximated by an energy source in the fluid zone indicated in Fig. 34.

The test chamber walls are not catalytic and considered at 300K, this walls have a little thermal exchange respect to the others.

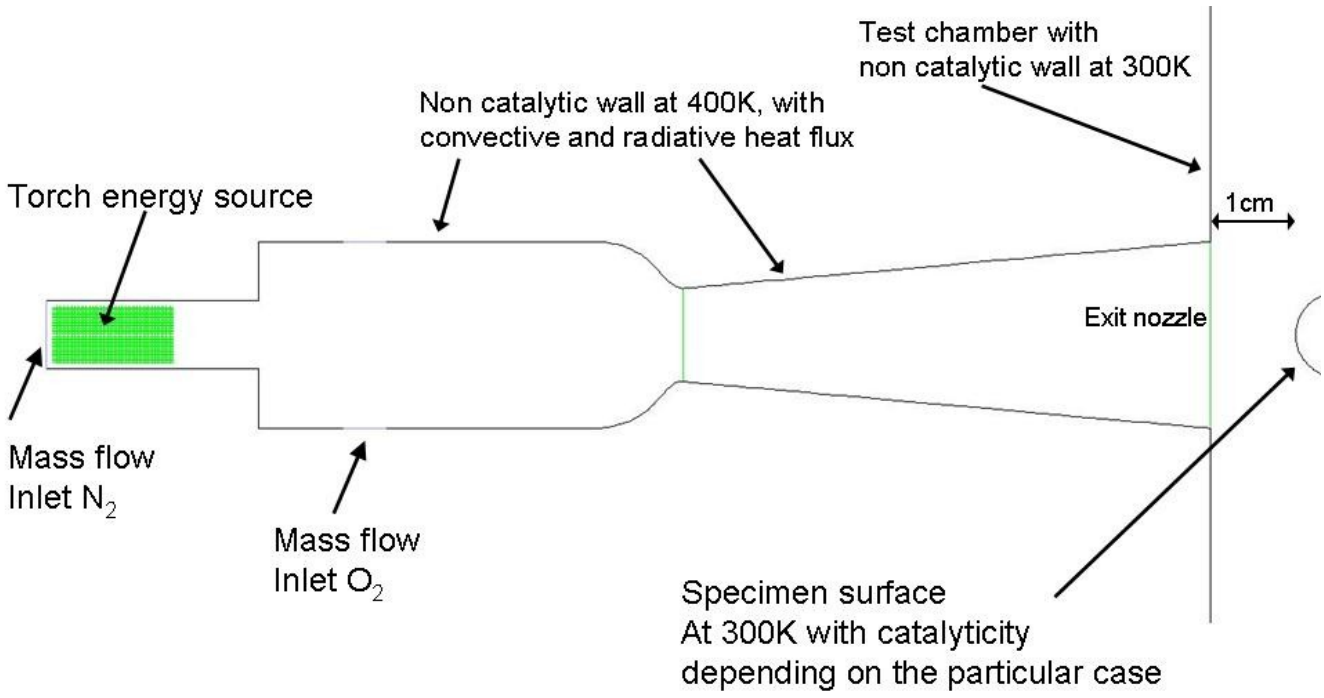

Fig. 34 The boundary conditions for the standard SPES model

At the model surface there are possible three wall conditions:

1. A non-catalytic wall, i.e. a wall where the chemical reactions can be neglected: $\overline{\nabla}\alpha_i \cdot \bar{n} = 0$ i.e. there are not changes in species mass fraction α_i along the normal coordinate at the surface n.

2. A partially catalytic wall can be defined as: $\rho\left(\alpha_i^w - \alpha_i^{eq}\right)K_i(T_w) = \rho D_i \overline{\nabla}\alpha_i \cdot \bar{n}$ where $K(T_w)$ is the catalytic constant depending of the wall chemical composition, the wall temperature, and the wall rughness [34], α_i^w is the actually mass fraction of the i-species at the wall, α_i^{eq} is the mass fraction at equilibrium conditions, $\rho D_i \overline{\nabla}\alpha_i \cdot \bar{n}$ is the mass diffusion Fick's law. Introducing the recombination factor γ_i = number of atom of i-species that recombine/number of atom of i-species impacting the surface , K_i is given by $K_i(T_w) = \gamma_i \sqrt{\frac{RT_w}{2\pi M_i}}$ R is 8314 $Pa\frac{m^3}{K}$ is the ideal constant of gas, T_w is the wall temperature, M_i is the molecular weight of the i-species.

A full catalytic wall can be described with the following condition: $\alpha_i^w = \alpha_i^{eq}$, because the wall in the CFD model is at 300K constant, the equilibrium coincides with the complete recombination of the dissociate species, thus the heat of the exothermic chemical reaction is given at the specimen wall.

The turbolence in the flow is necessary because the high thermal wall flux, required on the walls of the SPES facility. The k-ε model has been chosen because it allows the lowest pressure values at the exit nozzle, respect to the other turbolent models such like k-ω, or Reynolds Stress five equation. The k-ε model allows pressure values similar at the experimental ones.

Chap. V. The experimental tests

V.1. SPES Operative conditions

The best SPES configuration for re-entry thermal heating simulation has been found, by a wide campaign of experimental tests with different:

- mass flow rate from 0.5 up to 1 g/s
- model position, distance from the exit nozzle from 0.5, up to 4cm
- Arc current experimented from 300 up to 600A, corresponding to a power from 14 up to 38kW
- Pressure chamber from 90Pa up to atmospheric conditions
- Maximum mass weighted average total enthalpy at exit nozzle up to 19MJ/kg

Two nozzle have been tested with a nominal mach number of 3 and 6, although the second one achieves higher gas velocity at the exit, the stronger expansion bring to lower pressure at the model location, for this reason the Mach 3 nozzle allows higher model temperature than the Mach 6 nozzle, for example with a mass flow rate of 0,5 g/s and an arc current of 500A the maximum temperature is about 100K lower than Mach 3 nozzle case. From the one dimensional solution theory, the equation $M_{out} = f(\gamma)\frac{1}{R}\frac{A_{throat}}{A_{out}}\frac{1}{\rho_{out}\sqrt{T_{out}}}\frac{P_{in}}{\sqrt{T_{in}}}$, allows to understand the inverse relation between Mach at exit nozzle (M_{out}) and the product among density (ρ_{out}) and temperature (T_{out}) at the exit nozzle. R is the gas constant, and γ is the specific heat at constant pressure on the specific heat at constant volume ($\gamma = \frac{c_p}{c_v}$), by this formula an high Mach implies low density and temperature. The following SPES fundamental data refer all to Mach 3 nozzle.

The Tab.8,9,10 resume all the experimental data for the mass flow rate of 1, 0.75, and 0.5 g/s, there are indicated the average values of arc tension, current, and power (from 16 up to 35,7kW), the mass flow rate of the two gas, the temperature difference from inlet and outlet of the two cooling system of the torch and nozzle, the water mass flow rate of the two cooling systems, the specific total enthalpy at the exit torch and nozzle, the pressure in the chamber and at the exit nozzle, and in the last row of the table there are the averages of the maximum temperature achieved during the test.

	1	2	3	4	5	6	7
V[volt]	54	55	55	58	59	65	60
I[A]	300	350	400	450	500	550	600
Pot[w]torch	16167	19221	22124	25920	29473	35567	35700
m N2 [Kg/s]	0,0008	0,0008	0,0008	0,0008	0,0008	0,0008	0,0008
m O2 [Kg/s]	0,0002	0,0002	0,0002	0,0002	0,0002	0,0002	0,0002
m H2O torch [Kg/s]	0,142	0,144	0,145	0,143	0,146	0,151	0,136
m H2O nozzle [Kg/s]	0,208	0,208	0,207	0,208	0,205	0,208	0,210
deltaT_torch [K]	8,4	10,9	11,6	14,7	14,5	17,6	16,1
deltaT_nozzle [K]	4,7	6,1	6,8	7,9	9,4	11,6	9,6
Hout torch [Mj/Kg]	14,0	15,8	18,8	21,3	25,8	30,6	33,2
Hout nozzle [Mj/Kg]	7,0	7,1	9,0	9,9	12,5	14,4	18,1
Pchamber [Pa]	252	269	226	269	226	233	220
Pout nozzle [Pa]	931	931	941	932	909	666	np
Tmax [K]	1624	1729	1799	1923	2077	2089	2122

Tab.8. Averaged experimental condition for mass flow rate 1g/s.

	1	2
V[volt]	53	54
I[A]	400	500
Pot[w]torch	21200	27000
m N2 [Kg/s]	0,0006	0,0006
m O2 [Kg/s]	0,00015	0,00015
m H2O torch [Kg/s]	0,159	0,167
m H2O nozzle [Kg/s]	0,189	0,189
deltaT_torch [K]	9,3	11,4
deltaT_nozzle [K]	9,3	12,1
Hout torch [Mj/Kg]	25,0	31,8
Hout nozzle [Mj/Kg]	10,3	12,8
Pchamber [Pa]	100	91
Pout nozzle [Pa]	1146	960
Tmax [K]	1798	2046

Tab. 9. Averaged experimental condition for mass flow rate 0.75g/s.

	1	2	3
V[volt]	47	48,4	49,7
I[A]	300	400	500
Pot[w]torch	14100	19360	24850
m N2 [Kg/s]	0,0004	0,0004	0,0004
m O2 [Kg/s]	0,0001	0,0001	0,0001
m H2O torch [Kg/s]	0,161	0,167	0,163
m H2O nozzle [Kg/s]	0,209	0,197	0,199
deltaT_torch [K]	7,3	9,0	11,5
deltaT_nozzle [K]	5,4	8,4	10,2
Hout torch [Mj/Kg]	23,0	32,7	42,7
Hout nozzle [Mj/Kg]	9,1	12,5	17,4
Pchamber [Pa]	107	93	93
Pout nozzle [Pa]	np	np	np
Tmax [K]	1694	1854	1968

Tab.10. Averaged experimental condition for mass flow rate 0.5 g/s.

Two things must be noted in the above data, the first one is that at the same arch current the highest temperature is achieved with a mass flow rate of 1 g/s, the second one is the efficiency, i.e. the ratio of the total enthalpy at exit nozzle on the arc power, decreases with the arc power by the thermal dissipations, for this reason too high currents (above 500A) are not suggested.

Arc current above 500A erode the electrodes quickly. Moreover high enthalpy implies high chemical dissociation, by this for current above 500A the exit nozzle total enthalpy has about the 70% in chemical dissociation (numerical analysis data); the total enthalpy due to chemical dissociation does not contribute to the thermal heating of the non catalytic UHTC (the most part of UHTCs has low surface catalyticity), in fact for 600A arc current the temperature is 45K higher than for a 500A (Tab.8) , i.e. an arc power the 50% higher has given a maximum temperature only of the 2% higher. The wall heat flux is proportional not to the total enthalpy, but to the "operative" enthalpy for heating: $q_w \propto H_0 - \sum \alpha_i H_i^d - H_{vibration-electronic} + \sum \gamma_i \alpha_i H_i^d$, where H_0 is the total enthalpy (MJ/kg), H_i^d is the dissociation or ionization enthalpy for the i-species, α_i is the mass fraction of the dissociated or ionized i-species, $H_{vibration\text{-}electronic}$ is the enthalpy due to vibrational and electronic energy (only for the two

temperature model), and γ_i is the recombination coefficient for the i-species. For this reason the "operative" enthalpy for heating is usually about 1/3 of the exit nozzle total enthalpy.

In Fig. 35 it is plotted the specific total enthalpy at exit nozzle Vs. arc current, parametric with mass flow rate. Obviously at the same arc current the specific total enthalpy increases as the mass flow rate decreases, but the stagnation point pressure decreases, for this reason the best compromise for the thermal heating analysis is resulted to be the 1 g/s mass flow rate. In fact the wall heat flux is a linear function of the total enthalpy but also of the square root of the surface pressure P_{02}: $q \propto \sqrt{\frac{P_{02}}{R_s}} H_0$.

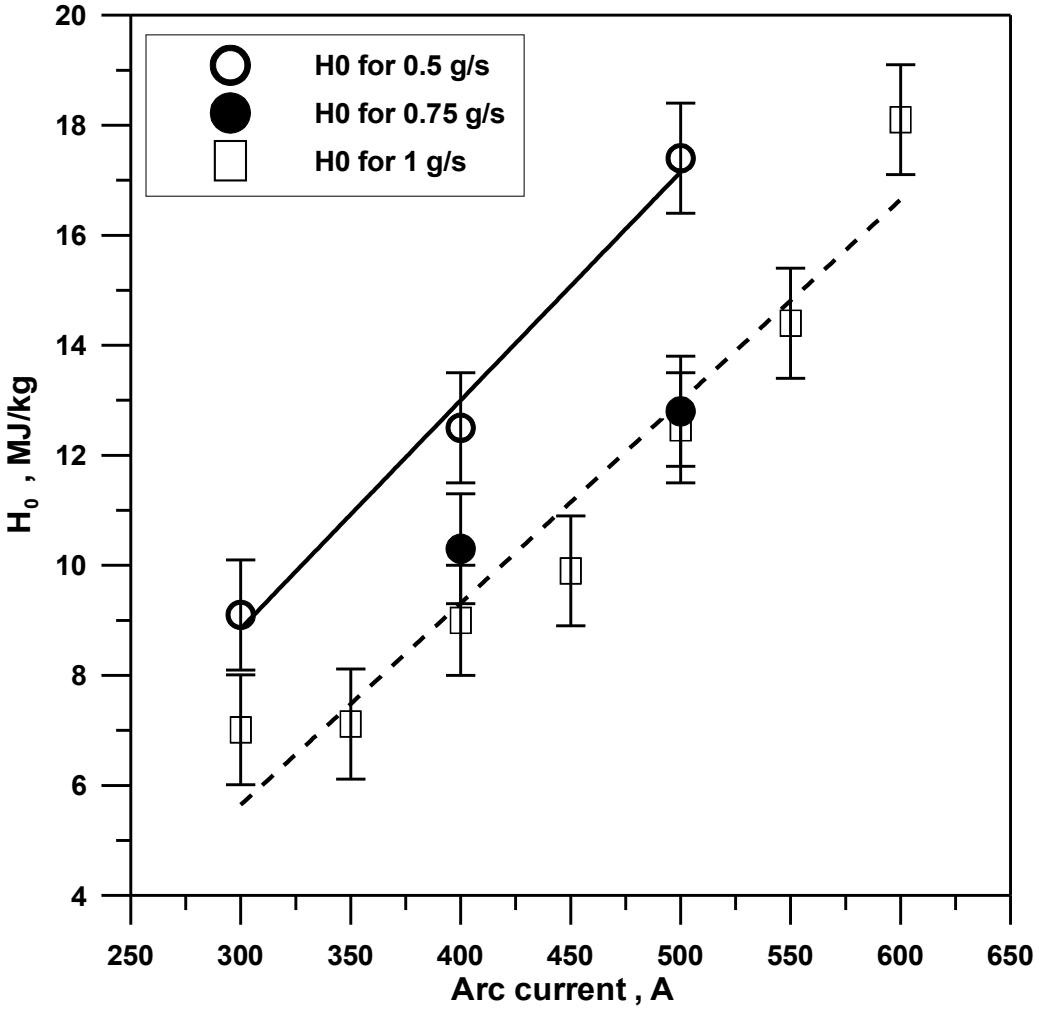

Fig. 35. Specific total enthalpy at the exit nozzle of the SPES facility, averaged values over all the experiments.

The stagnation point pressure has been measured by means of the Pitot probe, at several distances from the exit nozzle, for an arc power of 22kW and a mass flow rate of 1 g/s. The result is plotted in Fig. 36, the stagnation point pressure decreases about linearly with the distance, and at 1cm has a value about 9000Pa, at 2cm has a little increasing perhaps because there is an intersection of the expansion shock waves generate by the edges at the exit nozzle.

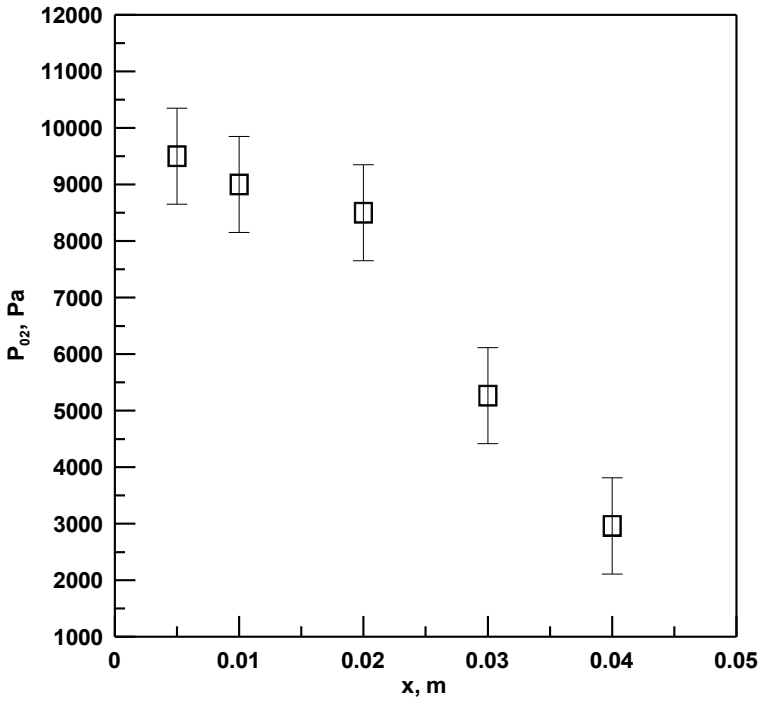

Fig. 36. The stagnation point pressure Vs. distance from exit nozzle, for an arc current of 400A, and a mass flow rate of 1 g/s.

Because the pressure at the exit nozzle is higher (typically 800-1200Pa) than the test chamber pressure (90-300 Pa), the nozzle is under-expanded, in the sense that the expansion continues throughout the test chamber, from the theory for an adiabatic shock wave the stagnation point pressure is a function:

$P_{02} = P_1\left(\frac{\gamma+1}{2}\right)^{\frac{\gamma+1}{\gamma-1}}\left(\frac{2M_1^{2\gamma}}{2\gamma M_1^2-(\gamma-1)}\right)^{\frac{1}{\gamma-1}}$ [35] for this reason a decrease of the static pressure upwind the shock wave P_1 results in a decrease of the stagnation point pressure.

In Fig. 37 there is a picture of the Pitot probe, the Pitot is water cooled, but it can withstand only few seconds in the flow.

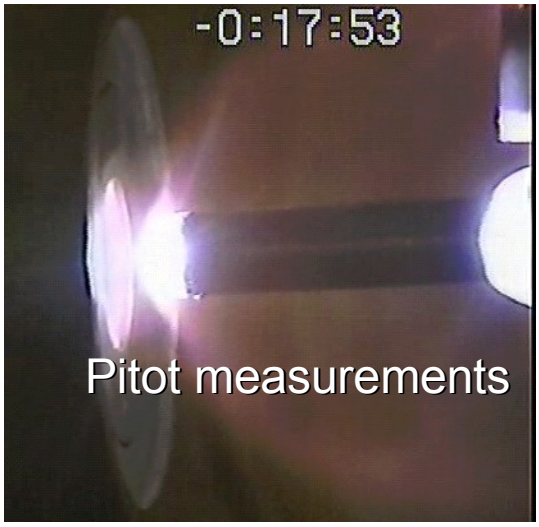

Fig. 37. A picture of the Pitot probe.

In Fig. 38 there is an image of the exit nozzle supersonic plasma jet, the gas is Argon at 0,5 g/s with an arc current of 500A; it is clear the expansion of the jet in the test chamber, as also the clashing of the shock waves generate by the exit nozzle edges. The Argon flow is more visible than the Nitrogen-Oxygen flow, because the colour of the first one is red-orange, the second one is closer to white-bleu.

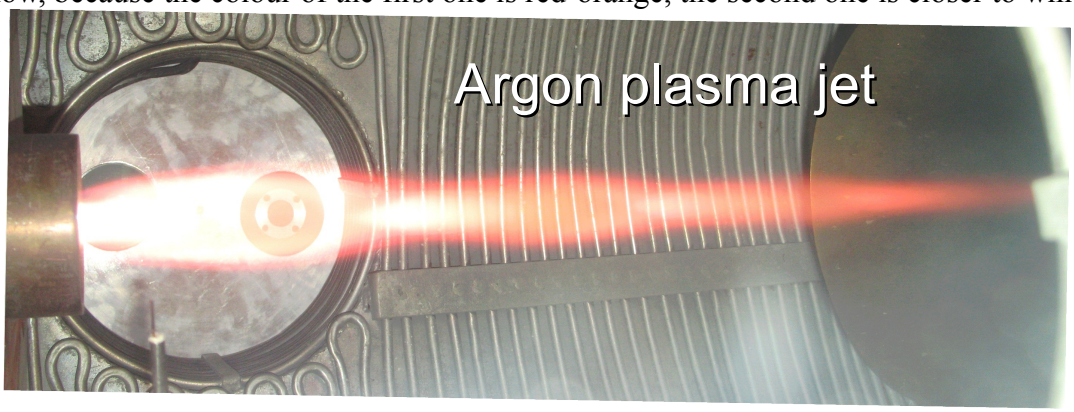

Fig. 38 Image of the exit nozzle supersonic plasma jet

In Fig. 39 there are the experimental stagnation point pressure (P_{02}) Vs. exit nozzle distance, compared with the P_{02} calculated by the Rayleigh formula: $P_{02} = P_1\left(\frac{\gamma+1}{2}\right)^{\frac{\gamma+1}{\gamma-1}}\left(\frac{2M_1^{2\gamma}}{2\gamma M_1^2-(\gamma-1)}\right)^{\frac{1}{\gamma-1}}$ from CFD results of two different numerical model, for an arc current of 400A, and a mass flow rate of 1 g/s; in CFD calculation there is not energy equilibrium on the model surface. Two concepts can be understand. The first is the independence of the stagnation point pressure by the chamber pressure in the first centimetres, in fact the two black curves are superimposed until to 6 centimetres from exit nozzle, this is surely true until under-expanded nozzle conditions overstay. The second one is that in the firsts centimetres, the experimental values are included between the two models with one and two temperatures.

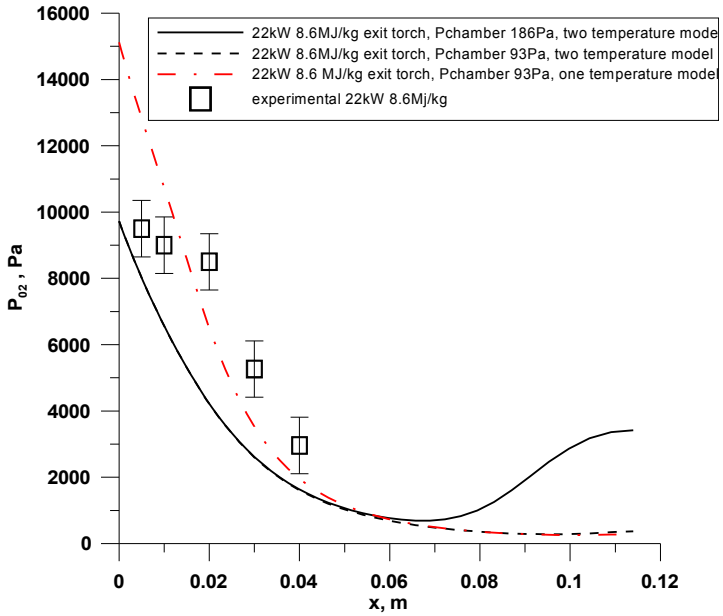

Fig. 39 The experimental and numerical stagnation point pressure (P_{02}) Vs. exit nozzle distance, valued by Rayleigh formula

After the preliminary tests, the selected distance from the exit nozzle for the thermal heating experiments has been one centimetre, because the need of high stagnation point pressure, closer distances have not be considered because the partial locking of the nozzle. The partial locking of the nozzle has been measured by the increasing of the exit nozzle and chamber static pressure due to the presence of the model in front of the exit nozzle. For specimen with big diameter that the standard 1cm used by the most of experiment, a bigger distance from exit nozzle is needed.

In Fig. 40 there is the maximum temperature on a model Vs. the exit nozzle distance, it is clear as the high temperature is possible closer the exit nozzle at 1cm. Note that for a supersonic flow the total enthalpy remains constant by increasing the exit nozzle distance, but the heating decreases because the stagnation point pressure becomes low.

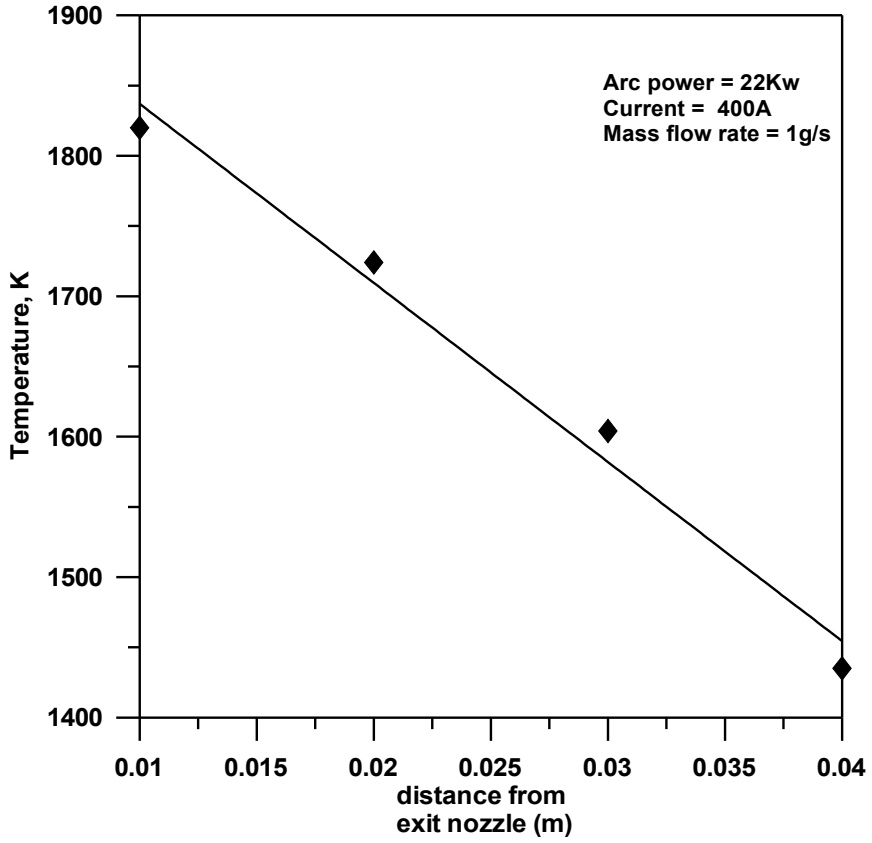

Fig. 40. Maximum temperature Vs. exit nozzle distance, hemispheric model with 5mm radius, 22 kW arc power, 1g/s mass flow rate.

In Fig. 41 there is the average of maximum temperature Vs. arc current, the values are averaged on all the experiments on the small sized (hemisphere with 5mm radius, and cone with 5mm base diameter) models. At low arc current the function T_{max} Vs. arc current is linear, but at high values, above 500A, the temperature increment is low, because the efficiency of the facility decreases at high arc power.

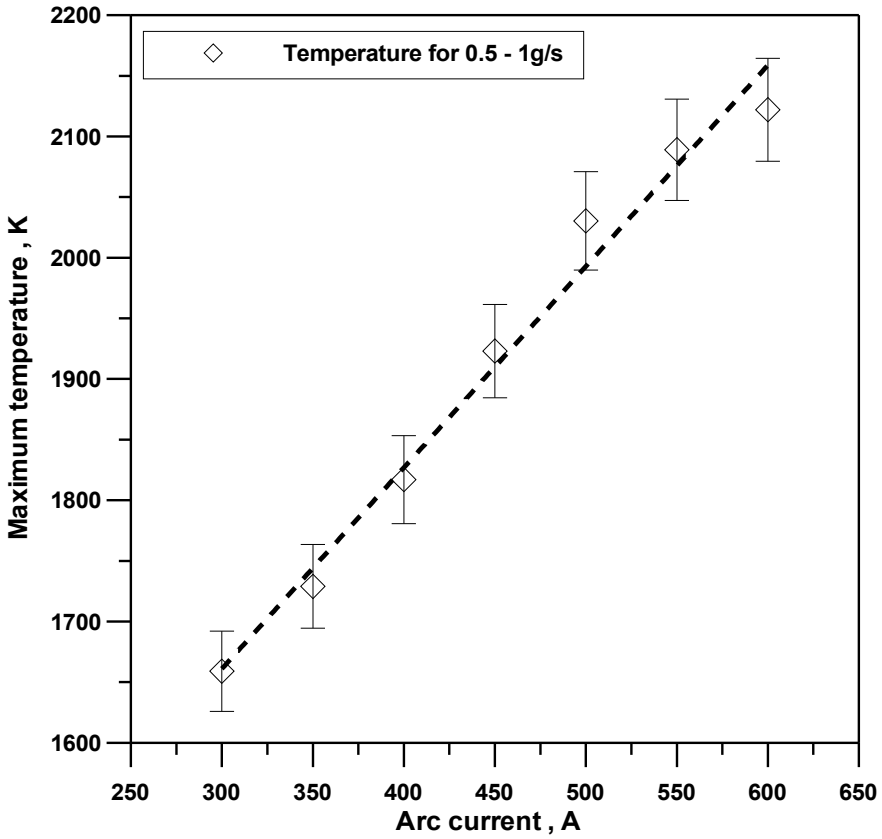

Fig. 41. The average of maximum temperature Vs. arc current.

V.2. Arc jet tests on ZrB2-SiC UHTC

ZrB2 is considered for ultra high temperature applications such as leading edges of hypersonic vehicles due to their high melting points. However, application of these materials is limited due to their poor oxidation resistance, low toughness, and low thermal shock resistance [36]. There are methods to improve the oxidation resistance of ZrB_2 [37] . ZrB_2 oxidizes to form B_2O_3 and ZrO_2. At temperatures between 670 and about 1370K, liquid phase boria is formed [38]. This liquid phase provides a somewhat protective liquid layer that slows oxygen transport to the underlying substrate. At temperatures greater than 1370K, the B_2O_3 boils off allowing rapid transport of oxygen through the zirconia scale to the underlying ZrB_2 substrate. Additions of 20v% SiC to ZrB_2 [39] provided improved oxidation resistance since the formation of a silica scale provides protection to much higher temperatures dependent on the amount of additive and oxidation condition [40].

The resistance to oxidation, the catalyticity and the emissivity of two models of a hot-pressed ZrB_2-SiC(15%Vol) composite were studied under aero-thermal heating in a strongly dissociated flow that simulates hypersonic re-entry conditions, in the SPES facility. The two UHTC models with a blunted and sharp profile (Fig. 42) were exposed to enthalpy flows up to 10 MJ/kg for a full duration of about ten minutes, the surface maximum temperature was about 2100 K. Because the different shapes the effect of the geometry was analysed also.

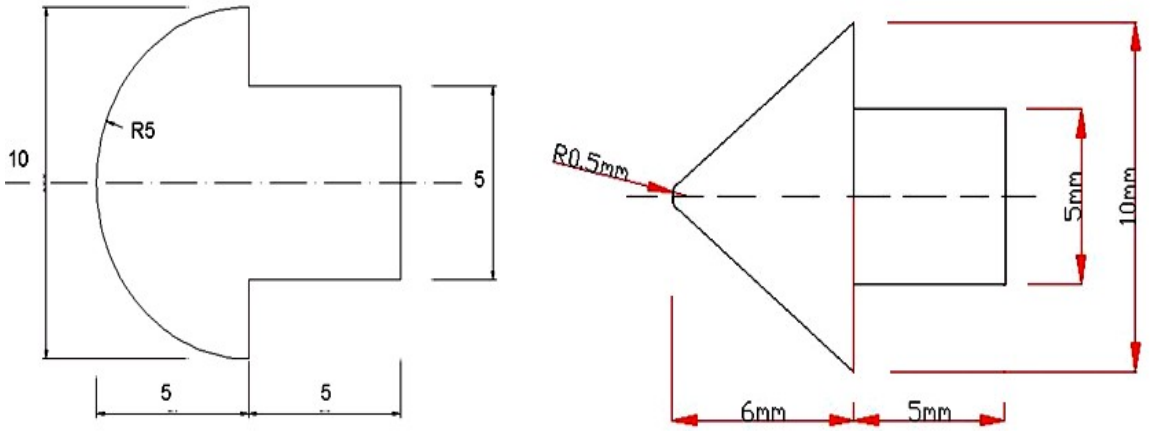

Fig. 42 The geometry of the tested models

The experiments were performed with standard SPES set-up and conditions, i.e. a gas flow rate of 1 g/s, a distance from the exit nozzle of 1cm, a static chamber pressure of about 200 Pa, and maximum arc current of 500A. Average specific total enthalpy (H_0) and maximum stagnation point pressure (P_{02}) ranged, between 4.5-10.3 MJ/kg, and 7000-9000Pa. In the Fig. 43 there are the pyrometer temperature measurement for the two models. The arc current was increased step by step because the safety of the facility, and to study the surface catalyticity in a wide range of temperature.

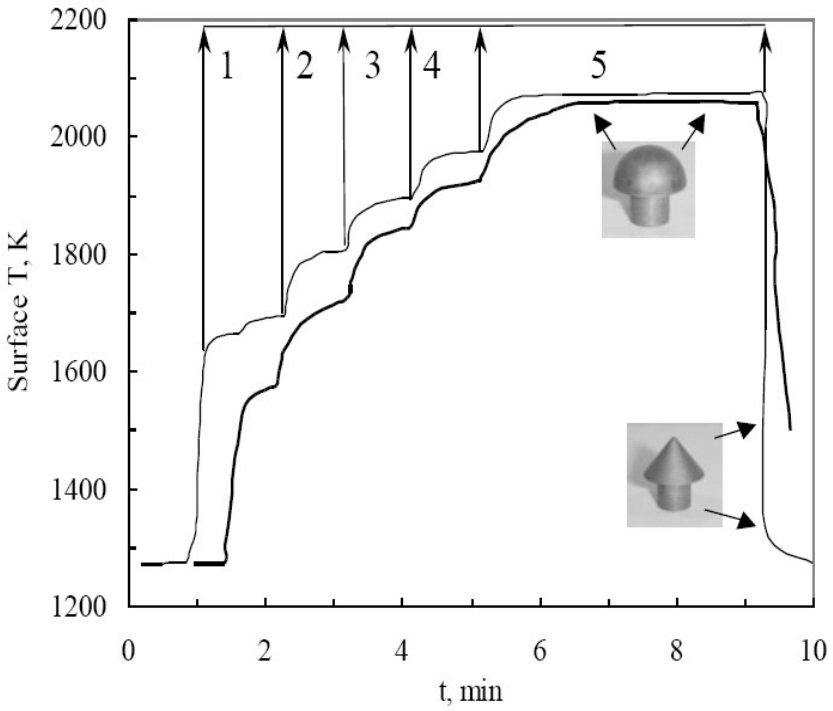

Fig. 43. Thermal history of the ZrB_2 SiC specimens.

The measured emissivity at 1μm wavelength Vs. temperature is shown in Fig. 44.

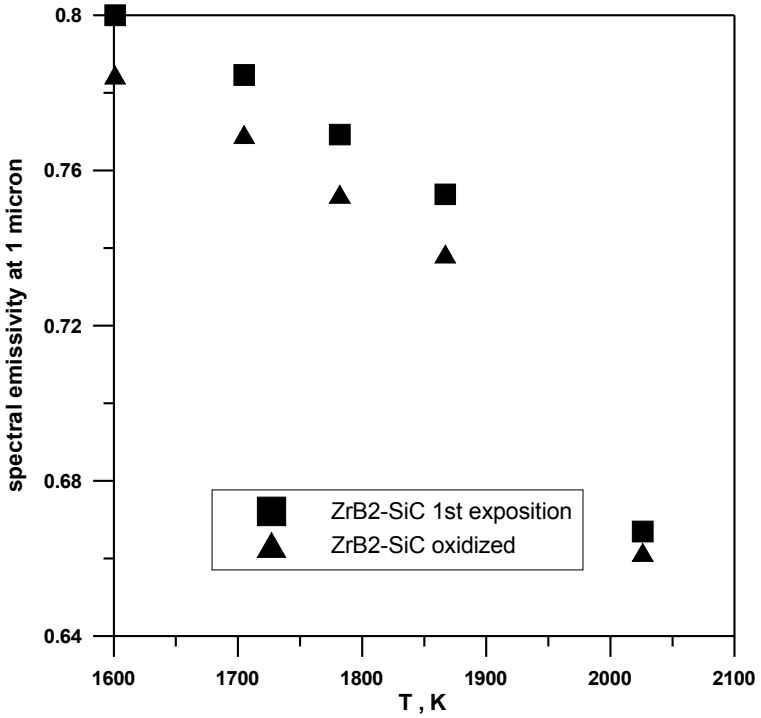

Fig. 44. The measured emissivity at 1μm wavelength Vs. temperature is shown.

Spectral emissivity values are consistent with post-test reflectance measurements of Marschall J. and co-workers [41]

The Tab.11 resume the condition for every step, i.e. the stagnation point pressure, the arc voltage and current, the exit nozzle total enthalpy. The indicated stagnation point pressure was calculated by numerical analysis.

	Step1	Step2	Step3	Step4	Step5
p_{02}, Pa	-	7000	-	7800	8100
ΔV, V	53	54	56	57	58
I, A	300	350	400	450	500
H_0, Mj/kg	4.5	5.5	7	8.6	10

Tab. 11. Fundamental parameters of experiment.

The reported emissivity of the UHTC specimen appear to change not only with the temperature, but also as its surface progressively interacts during exposure to the hot stream, changing the chemical nature of the surface under oxidation. In comparison to experiments performed in high enthalpy subsonic flow conditions (emissivity of 0.9 [42]), emissivity results were lower at the highest temperature. These results show that surface oxidation is affected not only by the specific total enthalpy H_0 of the flow but also by the peculiar flow behaviour. One direct consequence of a reduced surface emissivity is that the specimen reaches a stagnation point temperature comparable to that achieved in a subsonic flow [42] even though H_0 is half of that applied in high pressure tests (i.e. 20 MJ/kg). In fact from numerical analysis is resulted an increasing of about 5% in the average temperature for a 10% decreasing in surface emissivity .

In the Fig. 45 there is a comparison between the temperature measurement of the two colour pyrometer with the thermocam at two emissivity values.

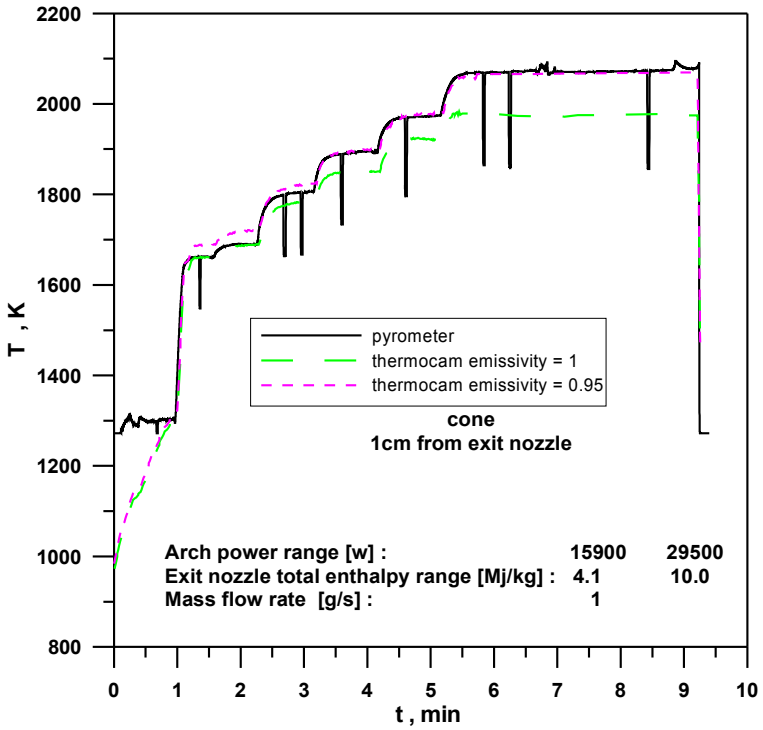

Fig. 45. The temperature measurement of the two colour pyrometer with the thermocam at two emissivity values.

The pyrometer curves present the spikes used to calculate emissivity. It is important to underlain that also the emissivity at the thermocam wavelength (9μm) changes from 0.95 to 1, and that the emissivity at different wavelength can be quite different. In fact in the Fig. 46 there is the spectral emissivity Vs. wavelength, in which the spectral emissivity of zirconia (ZrO_2) changes from 1 to 0.4 for wavenumber $=2\pi/\lambda$ (λ=wavelenght) from 1000 to 3000.

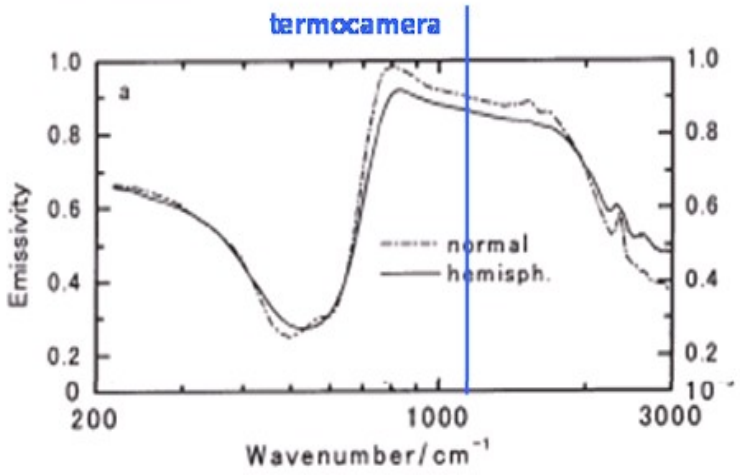

Fig. 46. Spectral emissivity Vs. wavenumber, for zirconia.

Both the UHTC specimens survived the arc-jet exposure without any optical evidence of mechanical failure, Fig. 47 shows the comparison of the two models before and after the exposures.

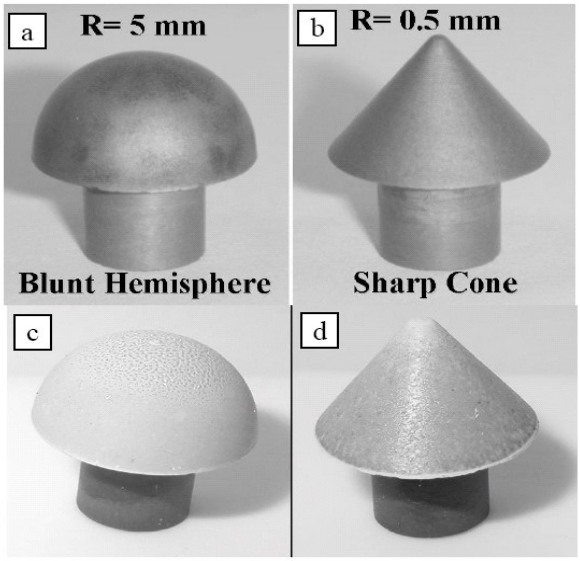

Fig. 47. the two models before and after the exposure.

Mass changes turned into net losses of 0.5 and 0.6% for the blunt hemisphere and the sharp cone, respectively. At the post-test inspections the hemisphere shows an uniform oxide surface, while the cone shows large oxidation on the tip and on the base edge, and a very thin layer on the main surface area. The images revealed a rather smooth contour of the oxidized surface and a whitish coloration, in the case of the cone this effect was concentrated at the tip. At higher magnifications, the oxidized surfaces appear more inhomogeneous, and mostly covered by a glassy coating. The major contribution to the varying surface roughness arises from the presence of craters, which are presently interpreted as the signature of the evolution of gases during exposure. The craters were differentiated in size and shape depending on their position with respect to the spot where the hot stream hit the model surface, Fig. 48 shows a magnification of the cone surface where the the craters are present.

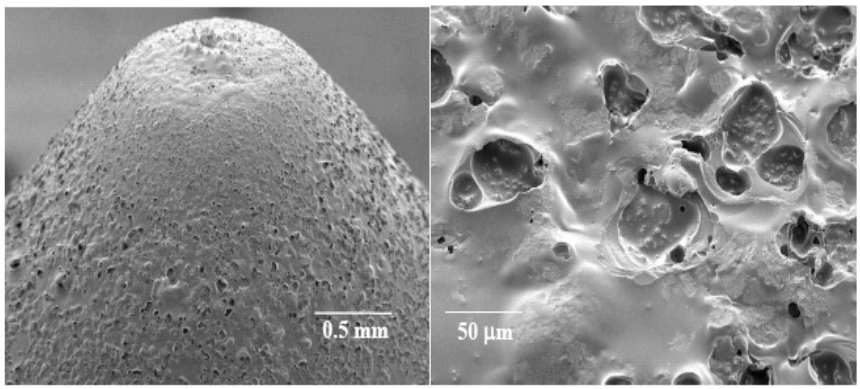

Fig. 48. Cone surface particulars.

SEM analysis on the cross sections of the specimens (Fig. 49 and Fig. 50), performed after the test campaign showed that a SiC depleted region was established below the oxide surface layer only in the sharp tip region of the cone; on the contrary, this SiC depleted region was absent along the conical surface of the sharp model and also along all the spherical surface of the hemisphere. The cross-sectional analysis shows an interesting variety of oxidized sub-layers extending below the outermost

glassy layer, and an non-uniform thickness of the oxidized layer for the hemisphere (150-50 μm), and a non-uniform thickness of the oxidized layer for the cone (190-60 μm).

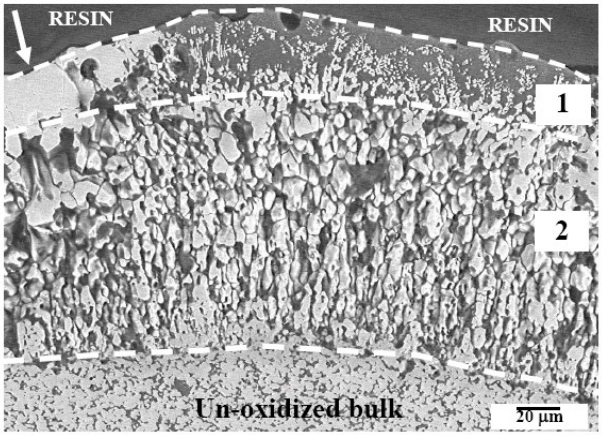

Fig. 49 Cross-sectioned polished blunt hemisphere (tip area, electron SEM micrograph): outermost glassy layer decorated with tiny zirconia particles (1), oxide sub-layer with zirconia crystals (2). Large zirconia crystals are indicated.

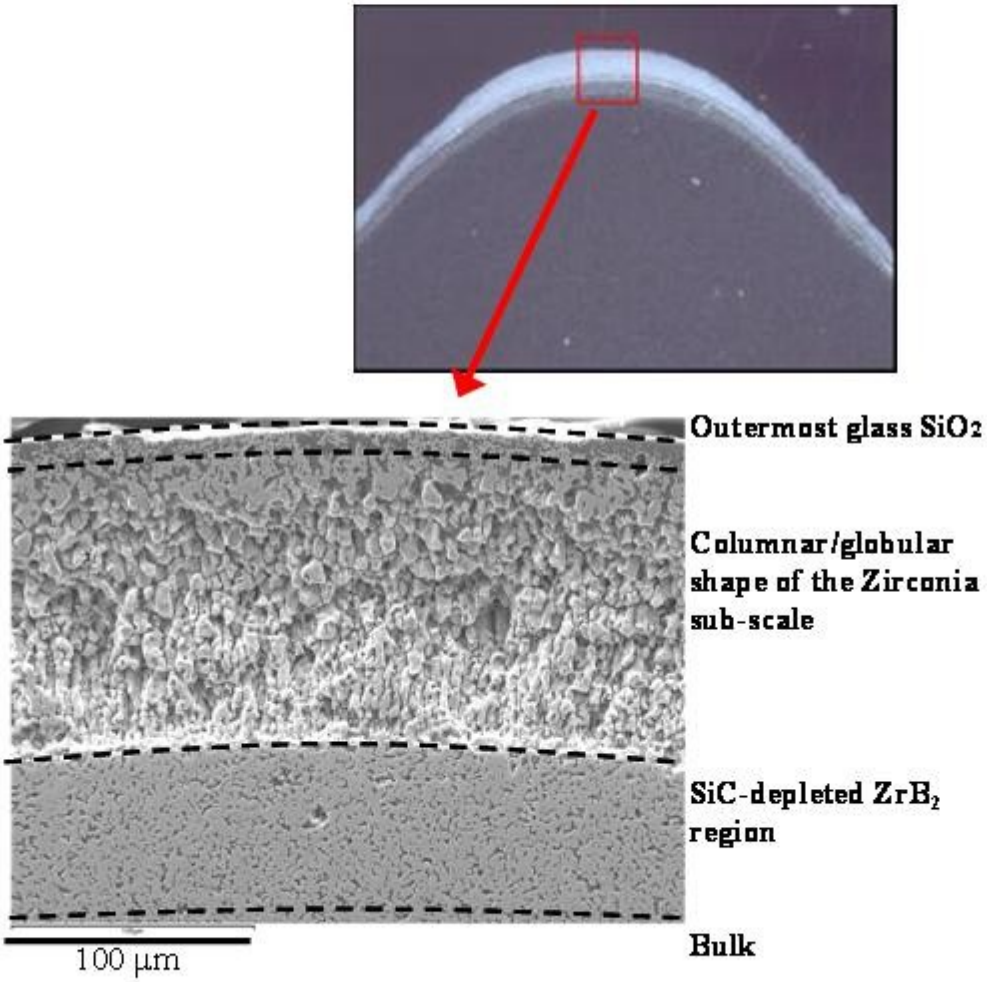

Fig. 50. The cone cross section with two magnifications (SEM micrograph).

In high-temperature oxidizing environments, ZrB_2-SiC composites react with oxygen through the net parallel reactions

$ZrB_2 + 5/2\ O_2 = ZrO_2 + B_2O_3$

$SiC + 3/2\ O_2 = SiO_2 + CO(g)$

These reactions yield oxide by-products like zirconia (ZrO_2), boron oxide (B_2O_3) and silica (SiO_2). Boron oxide, which melts at 670K, promptly it mixes with SiO_2 for temperatures above 1470K to form a borosilicate glass that spreads over and seals the external surfaces. The large volume increase upon oxidation of the bulk material due to the formation of solid zirconia was proposed as the driving force for the upward transportation of the fluid borosilicate glass. Increasing testing temperature, the B_2O_3 component of the borosilicate glass possesses an unusually high vapour pressure that leads it to evaporate preferentially from the glassy phase and leaves behind a boron-deficient silica layer. As the silica rich-layer thickens, it slows down the inward diffusion of oxygen to the pristine material below, limiting oxidation and lowering the oxygen partial pressure in the reaction zone. At sufficiently low oxygen pressures, the oxidation of ZrB_2 becomes negligible and the oxidation of silicon carbide becomes "active," proceeding through the main reaction $SiC + O_2(g) = SiO(g) + CO(g)$.

The specimens cross section show also the oxide sub-layer underlying the outermost glassy scale (Fig. 50), it is characterized by a duplex morphology of the zirconia crystals with a prevailing columnar shape close to the un-oxidized material, and a more globular shape nearer to the outermost surface glassy layer. Also, tiny zirconia particles which decorate the external glassy layer grow preferentially with a columnar shape (Fig. 49).

In contrast to conventional high temperature air-furnace experiments where the gas environment can be assumed in thermal equilibrium with the test specimen, arc-jet wind tunnels generate high-enthalpy and strongly dissociated gas flows that more actively reproduce the aero-heating expected in service on hypersonic vehicles [43].

Since the temperature and pressure levels reached on the two models during the arc jet experiments are similar, one of the possible explanations for the presence of this depleted region only at the sharp nose could be the different aerothermal behaviour. CFD and thermal models allow us to understand what is happened.

The Fig. 51 and Fig. 52 show the non catalytic wall heat flux, and surface pressure on both the models for the step 5 condition, i.e. the maximum arc power of 28kW. Because the wall heat flux is inversely proportional to the square root curvature radius, the wall heat flux on the cone results higher than blunt hemisphere model. The calculated peak cold-wall heat fluxes at step #5 is 5 or 12 MW/m^2, for the hemisphere and cone respectively.

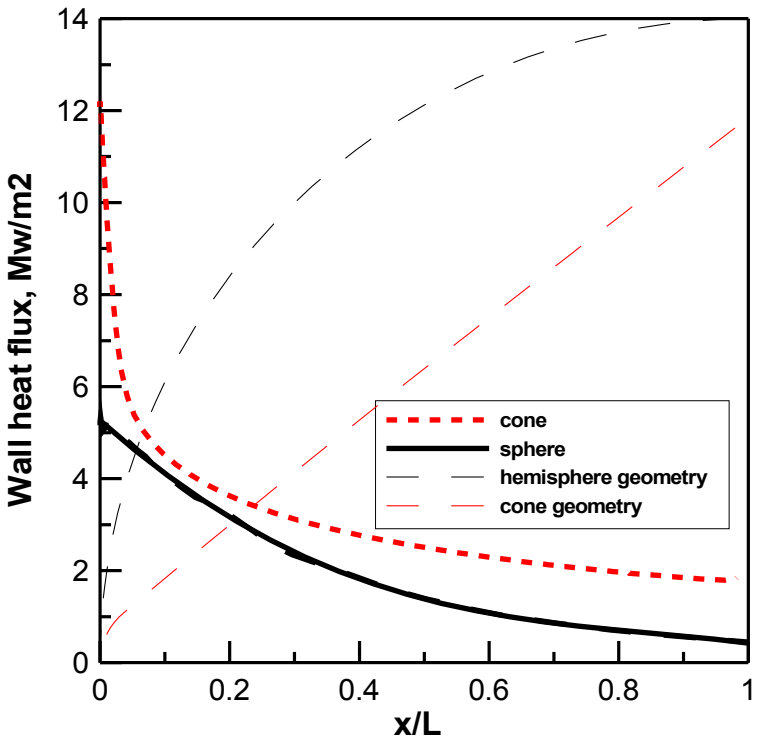

Fig. 51. Surface wall heat flux for hemisphere and cone model Vs. the non-dimensional abscissa, in the step 5 conditions.

The pressure distribution along the model surface results different between the two models, this is due to the different shock wave behaviour of the two models, in fact the shock wave for the cone results closer than the hemisphere. The stagnation point pressure of the cone is slightly larger than on the hemisphere and the stagnation point heat flux of the cone is again larger than expected considering the scaling law of the inverse of the square-root of the radius. These differences can be justified when rarefaction effect is considered. In fact, the Knudsen number (based on the nose radius) for the cone ($0.2<Kn<1$) is in the transition regime where the Navier-Stokes equations used in the CFD code are still valid but give pressure and the wall heat flux larger than for continuum regime [44].

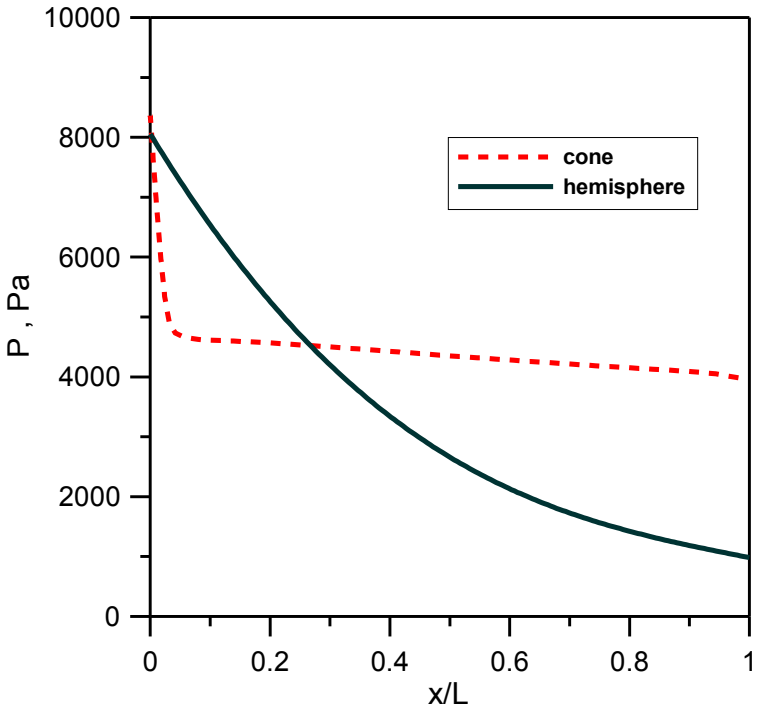

Fig. 52. Surface wall pressure for hemisphere and cone model Vs. the non-dimensional abscissa, in the step 5 conditions.

As shown in Fig. 53 the oxygen mass fraction along the surface is similar for both the specimens, for this reason can not be the cause of the different oxidation.

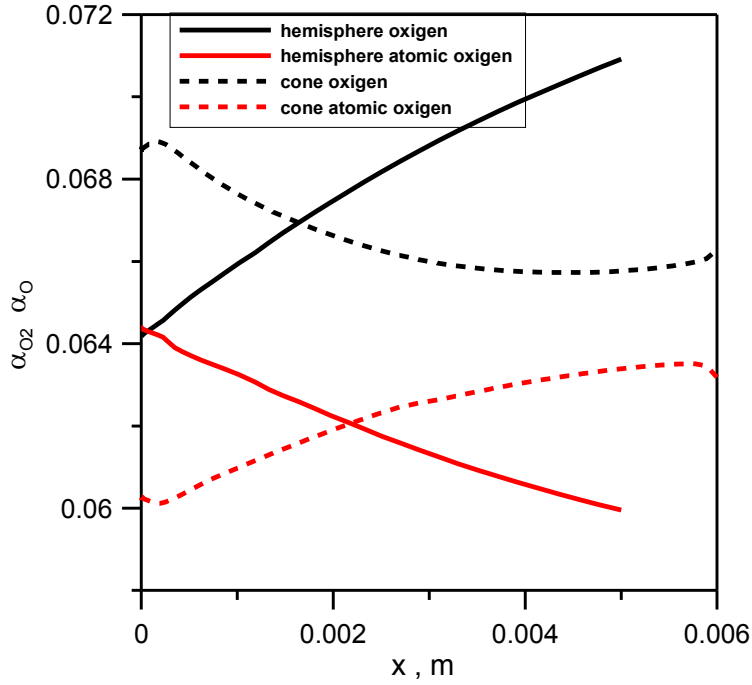

Fig. 53 the mass fraction of oxygen and molecular oxygen along the two model surfaces

A transient thermal analysis was executed for two steps in order to verify the CFD model by comparing the steady state temperature values with those obtained experimentally (T_{exp}), but overall to

calculate the maximum temperature in the stagnation point, which can be hundreds of Kelvin degrees higher. Tab.12 reports the comparison of numerical averaged temperature in a 3 mm diameter spot (T_{spot}) in the same area targeted by the pyrometer, with the experimental data. Tab.12 shows a good agreement of the numerical model to the experimental data, the global emissivity used for the thermal model is close to the experimental value at high temperature. The stationary temperatures obtained by the numerical model are in a good agreement with experimental temperatures achieved, by assuming a non catalytic surface behaviour.

		Hemisphere			Cone		
Power [Kw]	H_0 [Mj/Kg]	T_{exp} [K]	T_{spot} [K]	Global emissivity	T_{exp} [K]	T_{spot} [K]	Global emissivity
28	10.3	2053	2060	0.6	2083	2089	0.6
22	7.3	1823	1819	0.6	1893	1880	0.6

Tab.12. Comparison experimental-numerical results.

Two numerical models have been considered, one assuming the material UHTC properties (which results are indicated in the table), and another with an oxide layer of thickness similar to that evaluated by micrography. The density and specific heat of the oxide layer is supposed equal to the virgin UHTC, indicated in Tab.13, but the thermal conductivity is supposed 1.7 W/(mK); in the same Tab.13 also the other materials used in the model are indicated.

	ZrB_2+15% SiC	Alumina	Thermal Insulant
ρ , kg/m^3	6000	3900	400
c_p, J/kgK	460-785	881	469
K,W/mK	66	30	0.15

Tab.13. Material properties in the thermal model.

The resulting surface temperature for hemispherical and conical geometry, in the worst condition of step 5, is shown in Fig. 54 and Fig. 55. The inner axial temperature is shown also (the dashed lines), the experimental temperature is indicated by the circle. The high thermal insulation of the thin oxide layer changes very much the temperature distribution along the surface and in the inner of the two models especially for the cone.

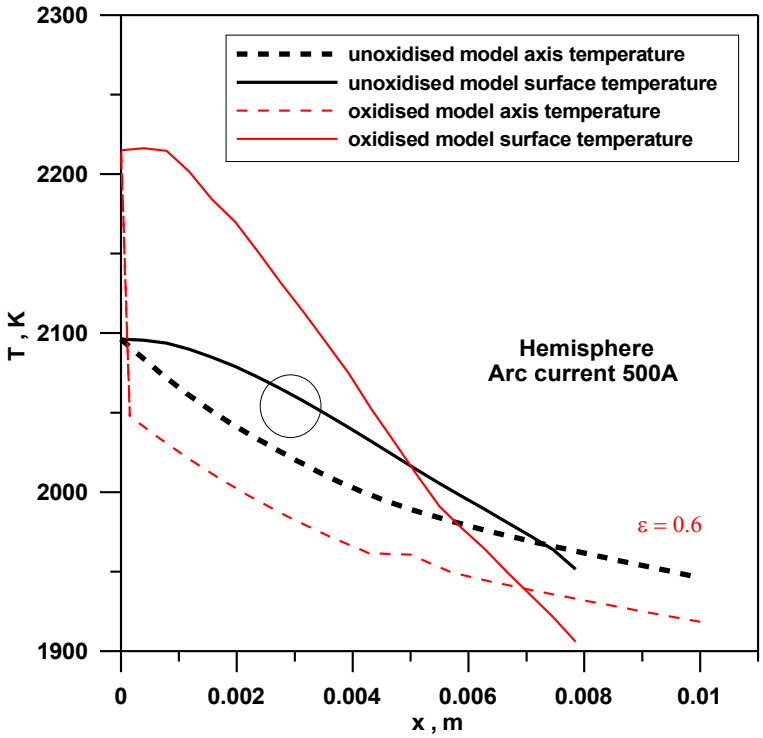

Fig. 54. Surface and axial temperature, for hemispherical geometry, in the worst condition of step 5, the experimental value is indicated by the circle.

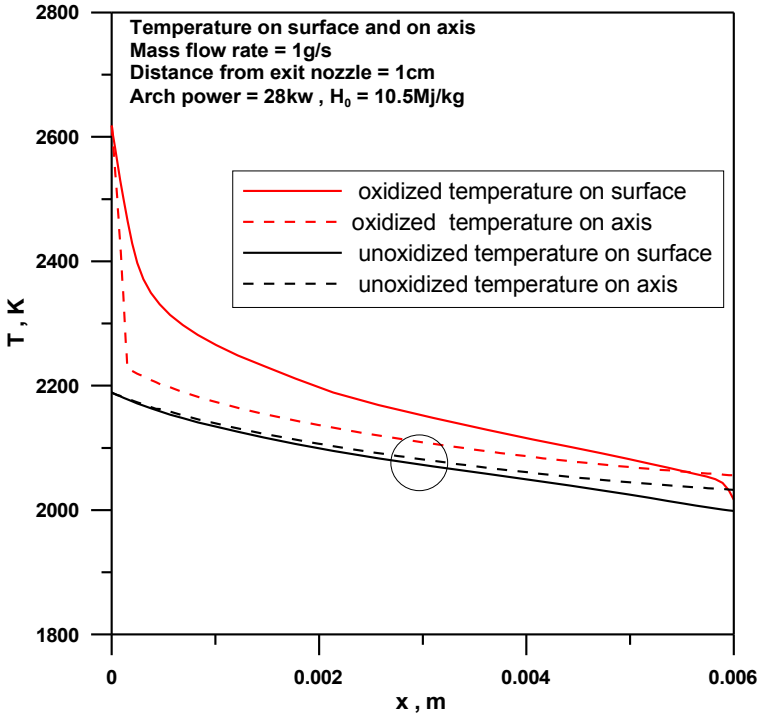

Fig. 55. Surface and axial temperature, for conical geometry, in the worst condition of step 5, the experimental value is also indicated by the circle.

The presence of the thermal insulating oxide layer influences overall the forward temperature, increasing it. The oxidation increases the stagnation point temperature for the cone of about 400K; the oxide layer has the effect to reduce the inner temperature. The effect of oxide layer on the surface temperature can not be seen by pyrometer because it reads the average temperature in a spot in the middle of the specimen, and neither by thermocam because the small resolution and curvature effect of such small specimen do not allow it to see the temperature close to the leading edge .
The distribution of the shear stresses (Fig. 56) correlates well with the evolution/bursting of bubbles. In fact, a localized increase in the shear stress promotes an anticipated explosion of gas bubbles (see small sized craters close to the tip in Fig. 48).

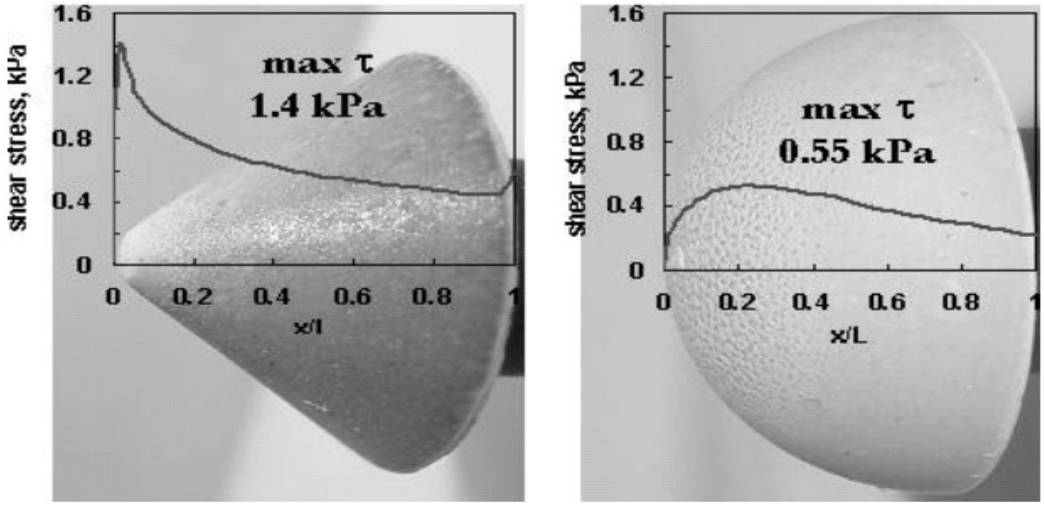

Fig. 56 Shear stress Vs. curvilinear normalized coordinate (x/L)

The distributions are quite different and this can be one of the causes of the different oxidation behaviour together with the different temperature distribution. In particular the shear stress values are comparable along the model surfaces with the exception of the leading edge.

Summarising, six aspects have come in evidence:

1) This UHTC changes the superficial composition, the emissivity, and thermal properties, if it is exposed in the SPES hypersonic high enthalpy flow.
2) The effects of thermal heating in hypersonic high enthalpy flow are quite different from those of plasma-torch or oxidation furnace exposition.
3) The two geometries have the same thermal treatment only apparently, in fact the numerical analysis shows higher wall heat flux, and temperature on the tip of the conical model than hemispherical one.
4) The thickness of the oxide layer grows up with the temperature-time product, because both the cone and the hemisphere have the maximum oxide thickness on the leading edge (190 and 150μm) respectively.
5) Above 2100K SiC-depleted diboride region can be found because 2100K is the melting point of silica, and the liquid film can be lost to volatility and shear forces in high velocity applications [45].
6) The material has a negligible catalytic behaviour.

V.3. Arc jet tests on HfB2-TaSi2 UHTC

15% vol $TaSi_2$ is added to HfB_2 matrix in attempt to further increase the oxidation resistance [46].

Two models have been machined by electro-erosion from the same cylinder obtained by hot pressing sintering process described in the par. II.1 earlier.

The arc-jet wind tunnel conditions, as well as the model geometry is the same analysed in the earlier paragraph, i.e. an hemisphere and a cone (Fig. 57).

The difference respect to the experiment earlier described is the material, the maximum exit total enthalpy (that allows a little high heat flux) , the maximum temperature, and the repeated heating cycle (the hemisphere has been tested three times).

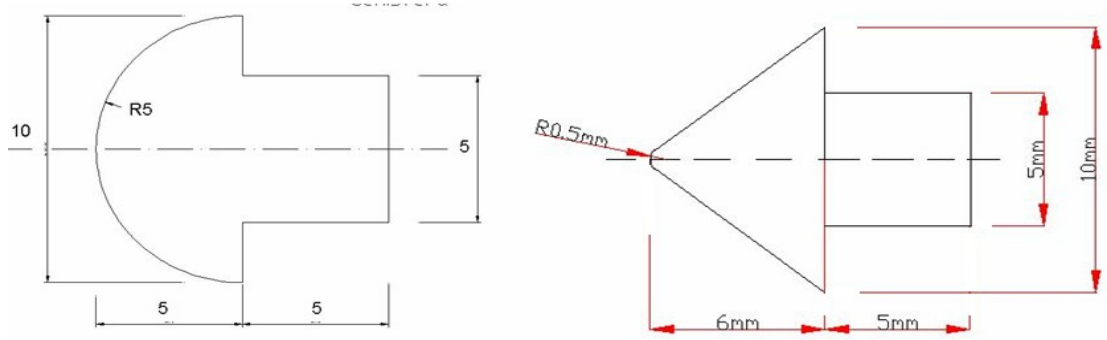

Fig. 57. Sketch of the two geometry tested for the HfB_2TaSi_2 model.

The arc-jet mass flow rate is set as to simulate the air, i.e. 1 gr/s with a chemical composition of 80 %wt N2 and 20%wt O2. The specimens are located at a distance of 1 cm from the exit nozzle. The models are tested in a series of runs. Each run is constituted by a succession of steps obtained by subsequent increase of the arc current. The initial average specific total enthalpy of about 8.7 MJ/kg is increased up to 12.9 MJ/kg. The hemisphere model was subjected to a 3 thermal cycles from room temperature to the final temperature in about 300-400 s. For each run, the maximum temperature was held for about 180 s. Tab. 14 shows the tests conditions and the stationary temperatures achieved. The stagnation point pressure in the present test conditions results to be between 7000 and 11000 Pa. Fig. 58 and Fig. 59 show the thermal histories of the two models in the various runs and steps. The spectral emissivity measurements at 1 μm wavelength are plotted in Fig. 60.

	Condition	a	b	c	d	e
	Arch Power, kW	16000	19000	22000	26000	29000
	H0, Mj/kg (±10%)	8,71	8,96	9,77	11,69	12,90
Hemisphere	Tmax 1st run, K	1601	1705	1782	1867	2026
	Tmax 2nd run, K	1659	1747	1860	1958	2010
	Tmax 3rd run, K	1605	1701	1818	1931	2044
	Time exposition, s	142	129	111	116	186
Cone	Tmax 1st run, K	1558	1676	1794	2025	2182
	Tmax 2nd run, K	1733	1874	2011	2144	2279
	Time exposition, s	84	86	87	95	95

Tab. 14 test conditions for the HfB_2TaSi_2 models.

In the Fig. 58 and Fig. 59 there are the pyrometer temperature histories, also the spikes to measuring the emissivity are visible.

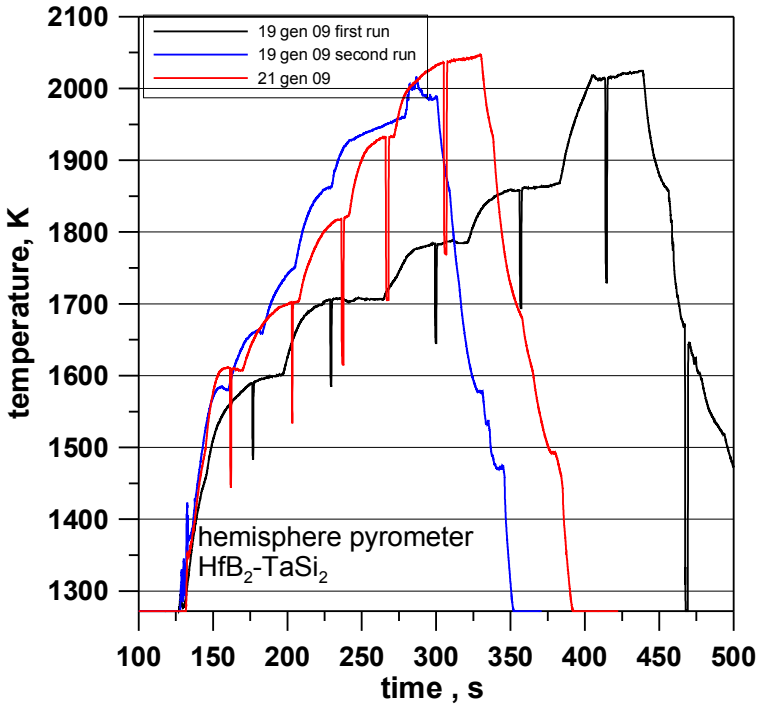

Fig. 58. Temperature history for hemispheric HfB_2TaSi_2 model.

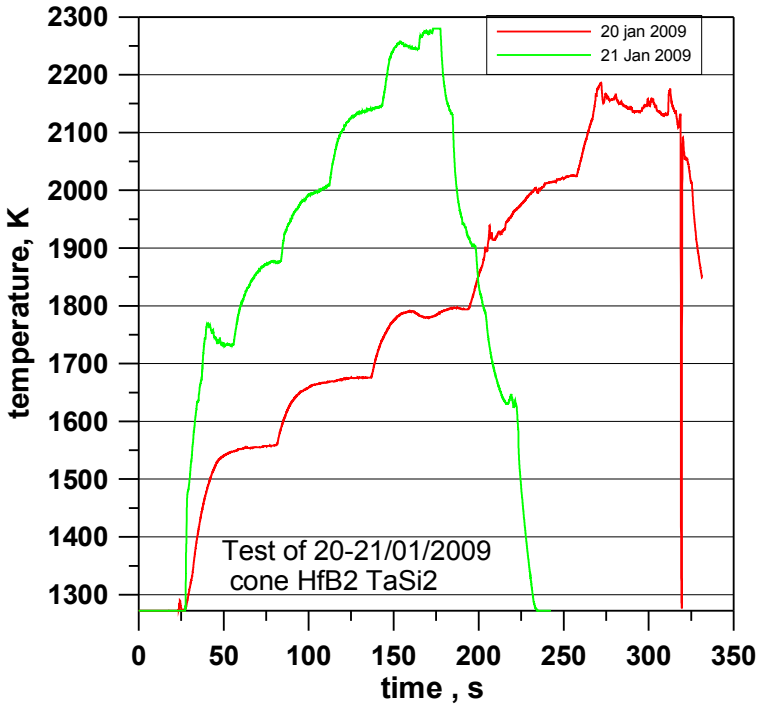

Fig. 59. Temperature history for cone HfB_2TaSi_2 model.

The emissivity is shown in the Fig. 60 for comparison the emissivity values for ZrB_2SiC are indicated also. The HfB_2TaSi_2 changes the surface emissivity in the first thermal heating as soon as the temperature goes over the 1800K.

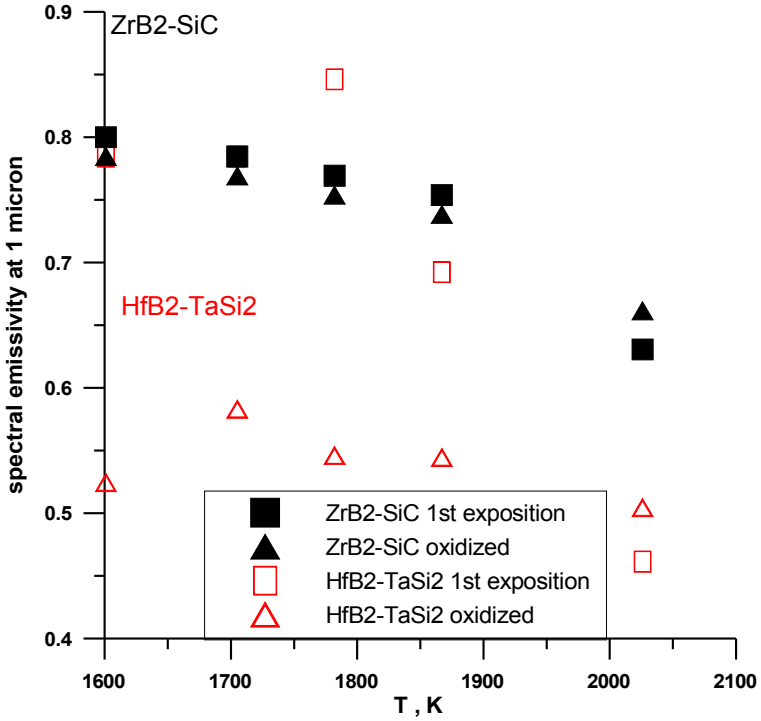

Fig. 60. Spectral emissivity for HfB_2-$TaSi_2$ and ZrB_2-SiC

The emissivity plot shows that during the first run there is an abrupt decrease when the recorded temperature exceeds 1800K (from 0.85 at 1800 K to 0.45 at 2050K). In contrast, during the following runs, the values of emissivity tend to remain between 0.5 and 0.6. This change is certainly related to the microstructural modification induced by oxidation, as described later. During the first exposition, the high surface temperature achieved, together with the chemical environment, caused a surface oxidation, which changed the emissivity and the thermo-physical properties of the external layers. It must be mentioned that the temperature reached at the sample surface depends much on the ability of the material to reject the heat by radiation, i.e. on its emissivity ($\varepsilon = 1$ for an ideal black body, $\varepsilon < 1$ for a real material surface). The higher the emissivity, the greater the emitted radiation, the lower is the heating. The temperature distribution on the sample also depends on its thermal conductivity, since a high thermal conductivity allows heat to be conducted from the leading edge to colder zones and to obtain a more uniform temperature distribution.

It must be remembered that at the exit of the torch, the plasma flow containing nitrogen and atomic nitrogen expands through the mixing chamber (22 mm in diameter), comes into contact with the oxygen, so that oxygen dissociates and a reacting mixture composed of O2, N2, NO, O and N is formed. Fig. 62 shows composition of the flow at the exit nozzle that results from computations performed considering a torch power of 16 and 29 kW, which corresponds to an average specific total enthalpy of 8.7 (condition (a) in Tab. 14) and 12.9 MJ/kg respectively (condition (e)). The dissociated oxygen mass fraction at the exit nozzle is high (about 0.08 for condition e), and this concentrations remain constant until the shock wave because the flow is supersonic and chemically frozen in this zone of the SPES. This dissociated oxygen is fundamental for the model oxidization, because of its reactivity. Because the presence of dissociated chemical species in the exit nozzle flow, the arc-jet plasma wind tunnel tests are considered more severe than an in flight test, from the oxidation point of view. Although the shock wave (in the condition e) reaches a temperature of about 6000K (Fig. 61), its contribute in increasing the dissociated oxygen is low (from 0.08 up to 0.09).

In Fig. 61 there is the temperature contours for the hemispherical model in the condition e, it gives also information on the blunt shock wave shape.

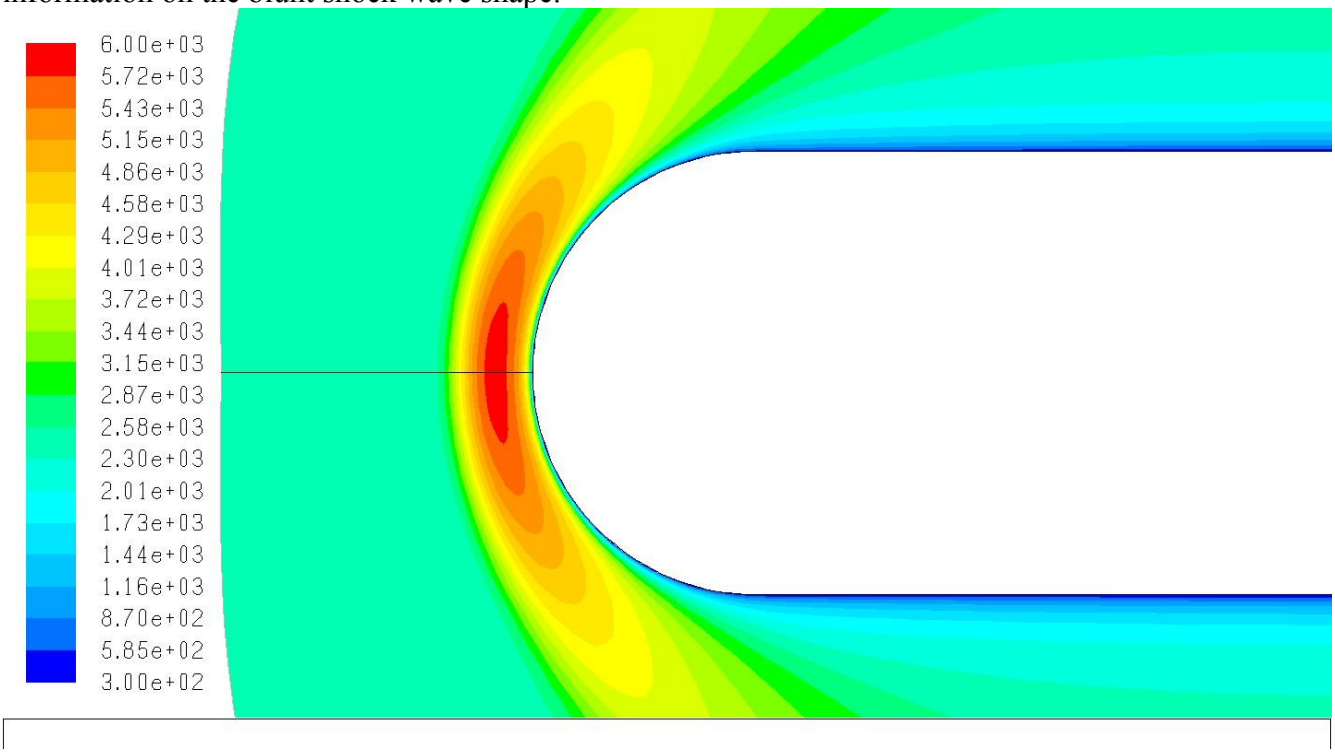

Fig. 61 The temperature contours for the hemispherical model in the condition e

In Fig. 63 also the exit nozzle pressure and total enthalpy are shown, the pressure decreases until the shock wave because the nozzle is under-expanded, but the total enthalpy in the axis zone remains constant also after the shock wave and at model location.

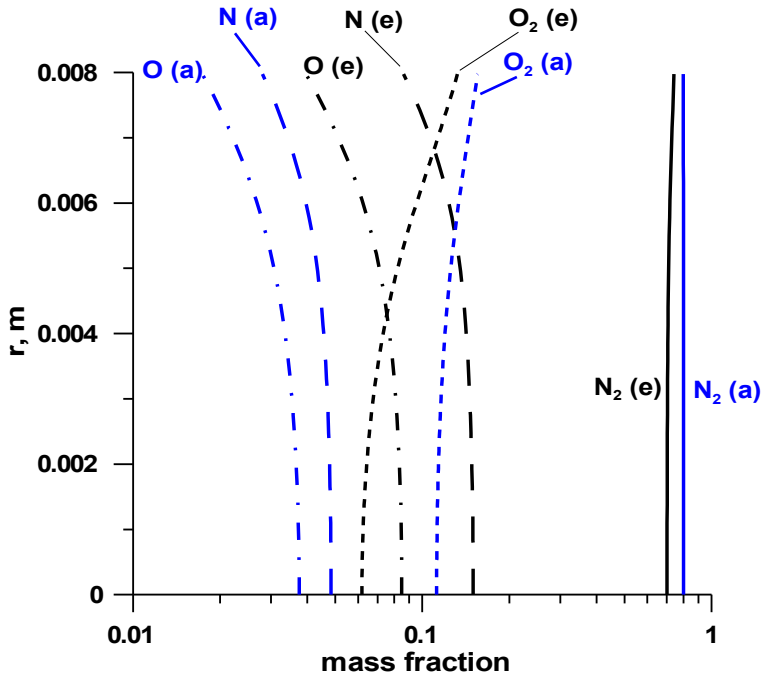

Fig. 62. computed mass fractions of the species along the exit nozzle radius (r) for conditions (a) and (e) indicated in Tab. 14.

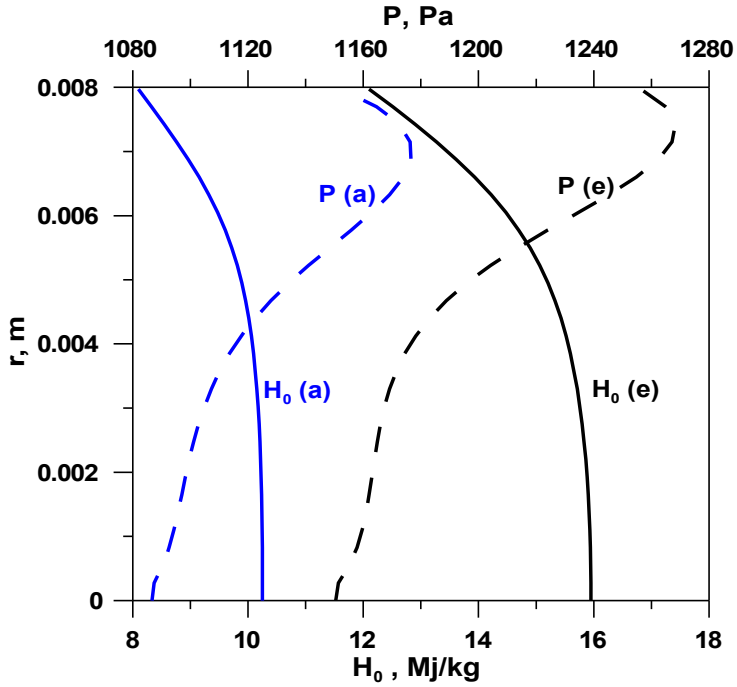

Fig. 63. Computed pressure and total enthalpy at the exit nozzle along the exit nozzle radius (r) for conditions (a) and (e) indicated in Tab 14.

At the exit nozzle the total enthalpy remains constant for 4mm along the nozzle radius, thus the small sized models, such as those here investigated, are put in an uniform enthalpy flow.

According to the calculations, the average specific total enthalpy in proximity of the specimen remains constant with the same values as at the exit nozzle, at about 10 and 16 MJ/kg respectively. The stationary temperatures obtained by the numerical model are in a good agreement with experimental temperatures achieved, by assuming a non catalytic surface behaviour. The calculated wall heat flux distribution with cold wall (300 K) for the condition (e) is shown in Fig. 64. The average wall heat flux is bigger for the conical geometry, but the integral of the wall heat flux is the same because of the greater surface area of the hemisphere.

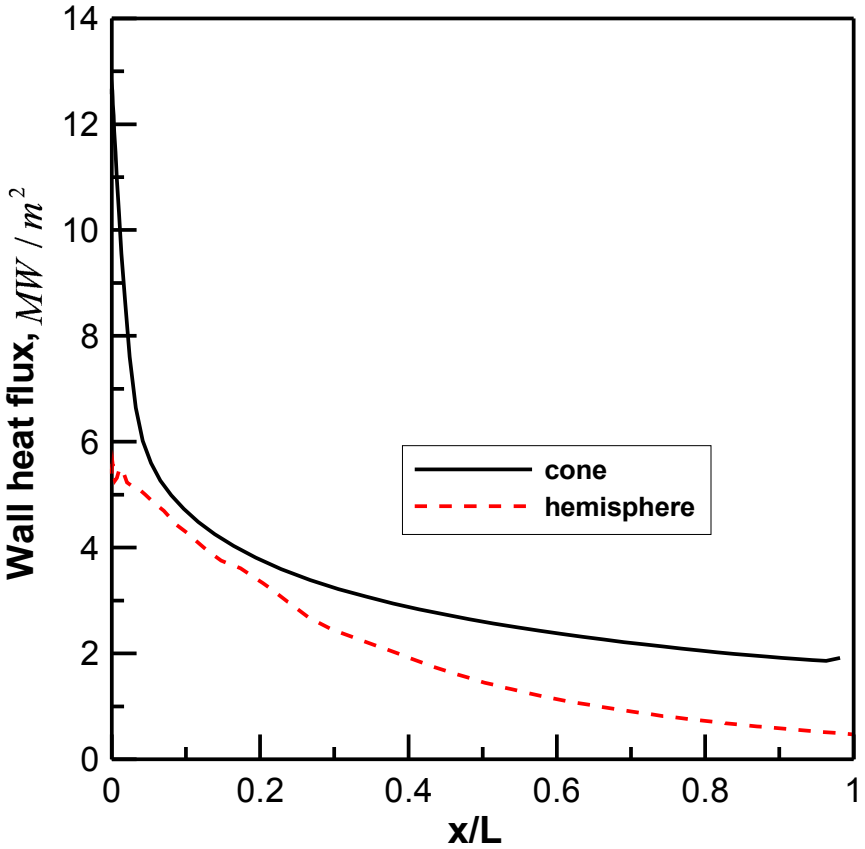

Fig. 64. Calculated wall heat flux on the models' surfaces, for the worst thermal condition, i.e. for the step (e).

The formation of the oxide layer with a low thermal conductivity can create a change in the temperature distribution. To assess if such oxidised layer can generate a significant change in the surface temperature, a numerical model of the cone and of the hemisphere with an mixed oxide layer HfO_2 and SiO_2 was implemented. From the post exposure analysis (see next paragraph), the oxide thickness is variable from 170 to 100 μm for the cone and from 130 to 45 μm for the hemisphere. In first approximation, the oxide was considered to be constituted by a mixture of 50 vol% HfO_2+50 vol% SiO_2, taking 1.6 W/(mK) and 3.3 W/(mK) as the thermal conductivities of silica and HfO_2 [46] respectively. Hence an average thermal conductivity value of 2.5 W/(mK) was used.

The Tab. 15 shows the thermal properties of the numerical thermal model.

Material	Density	C_p	Thermal Conductivity	Emissivity
%vol	g/cm^3	j/(kgK)	W/(mK)	
HfB_2+15 $TaSi_2$	10.9	400	78	0.8
HfO_2-SiO_2	10.9	400	2.5	0.6-0.5

Tab. 15. The thermal properties of the numerical model.

Fig. 65 shows the calculated increase of the surface temperature as a function of the exposition time for hemispheric and conic samples in the condition of step (e), the numerical model has a variable thinness oxide layer similar to that found by post test cross section analysis.

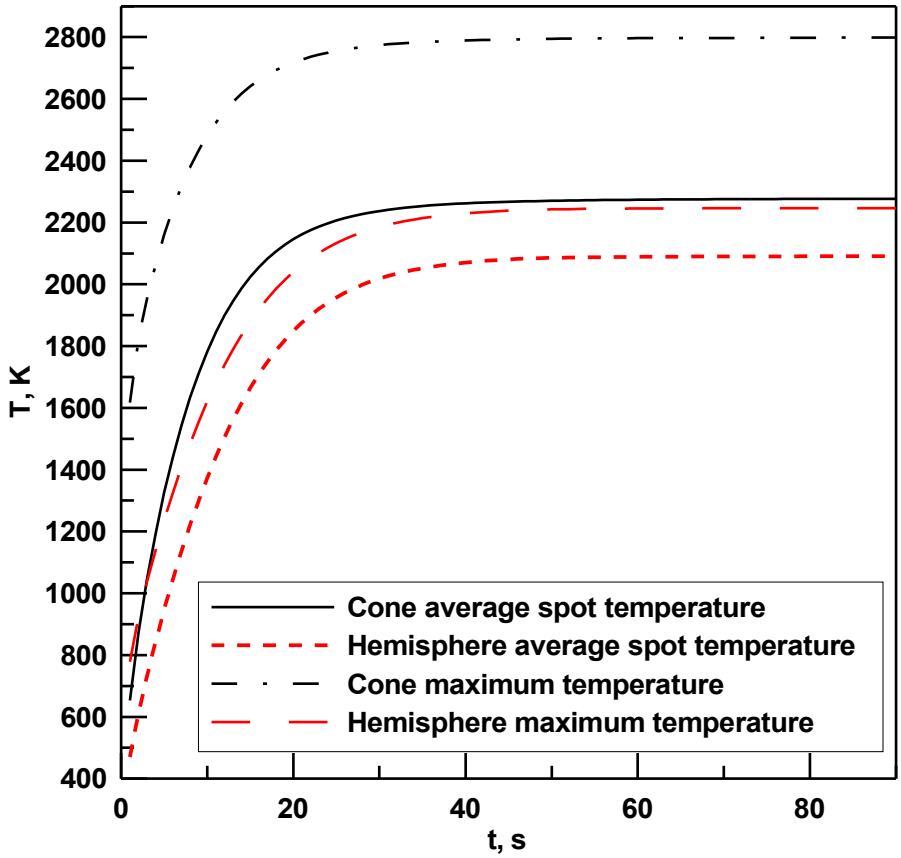

Fig. 65. Numerical temperature histories of the models surfaces in the case of the wall heat flux corresponding to point (e) of Tab. 14. For oxidised surfaces, the emissivity is considered 0.5.

The temperature on the leading edge increases rapidly and achieves the stationary state in few seconds. This is especially true for the cone (Fig. 65), where the nose tip zone remains at high temperatures for a longer time than the base. The thermal heating is faster for the cone than for the hemisphere due to the smaller mass of the former than the hemisphere. The maximum temperature measured on the surface of the hemispheric sample was 2044 K, the total time of exposition was about 11 minutes. The corresponding stagnation point heat flux, computed by numerical simulation is in the range 3-6

MW/m^2. During the testing of the cone, the surface temperature measured by the two colour pyrometer reached 2279 K, the total time of exposition was about 8 minutes. The corresponding computed stagnation point wall heat flux is of the order of 6-13 MW/m^2. The surface temperature profiles are shown in Fig. 66 and 67, and they are compared to the surface temperatures of a non oxidised material. The points corresponding to the experimental temperatures are also superimposed to the curves, showing a good agreement with the simulations.

The surface temperature distribution of the oxidised layer is radically different from that of unoxidised model, especially in the cone tip region (Fig. 67). Indeed for the cone, the increase of the maximum temperature reached on the tip due to oxidization is about 400 K respect to that of unoxidised model. Instead, for the hemisphere, the difference between the oxidised and unoxidised model is about 85 K. This can be explained with a thinner oxide layer for the hemisphere than for the cone.

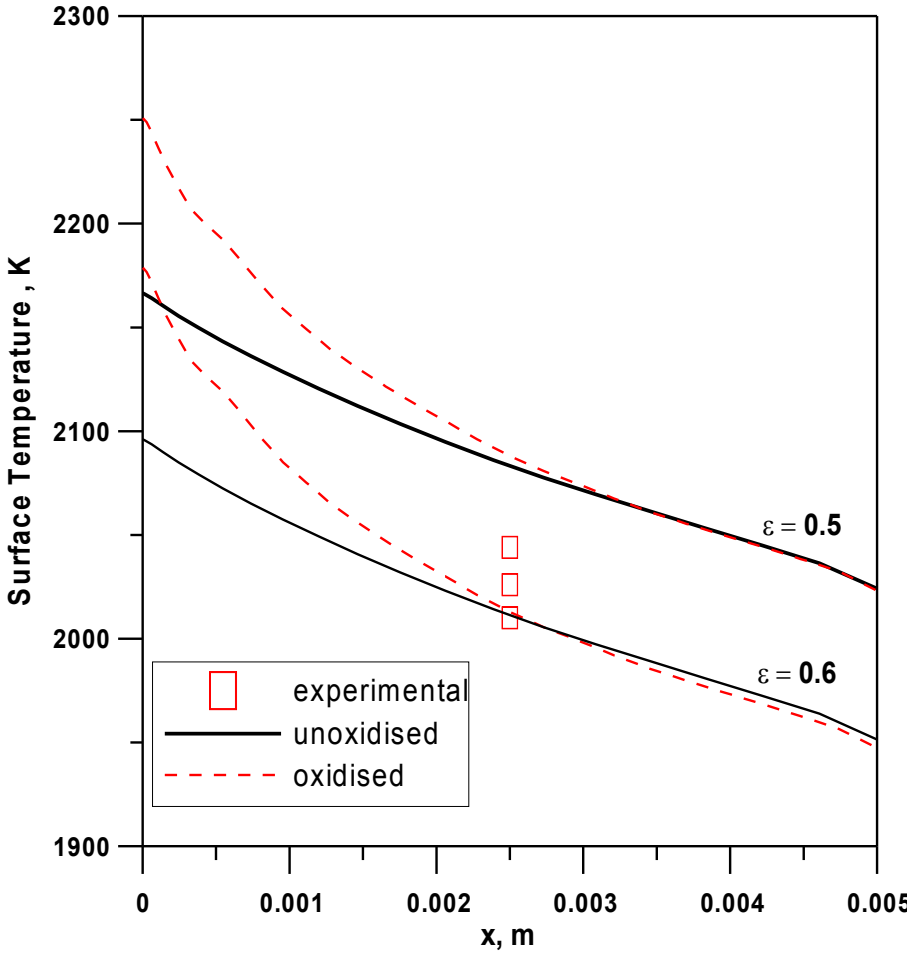

Fig. 66. Computed surface temperature distribution for the condition at point (e), for the hemisphere . Emissivity of 0.5 and 0.6 were considered for oxidised and non oxidised surface, respectively. Experimental value are superimposed.

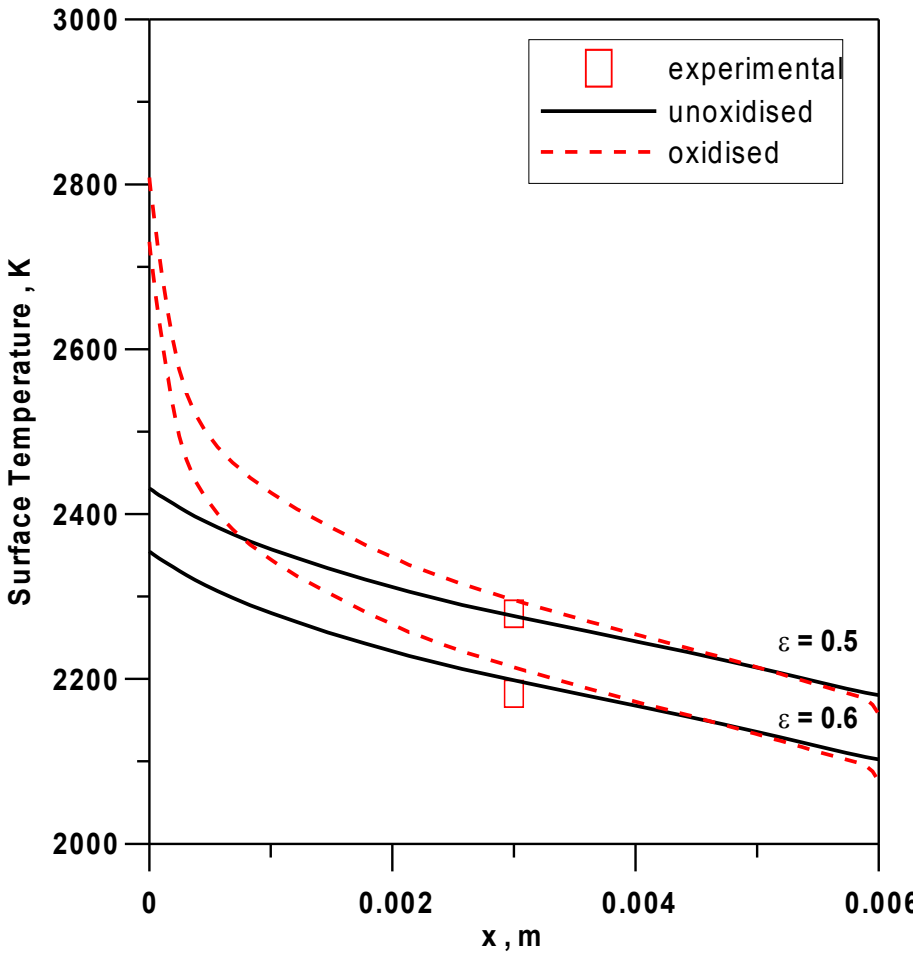

Fig. 67. Computed surface temperature distribution for the condition at point (e), for the cone. Emissivity of 0.5 and 0.6 were considered for oxidised and non oxidised surface, respectively. Experimental values are superimposed.

The change of temperature distribution caused by the oxide formation does not have a significant effect on the experimental temperature read by pyrometer. As a matter of fact, the increase of temperature due to oxidization is located only in the leading edge and the decrease of the temperature is located only in the trailing edge, while the pyrometer reads the average temperature in a spot at around in the middle height of the specimen body. On the contrary, the high temperature resulting by the numerical simulation on the leading edge of the oxidised cone must be taken into consideration, because it could have provoked more pronounced damages on the top of the cone surface.
The model pictures before and after the tests are in Fig. 68. The sharp cone appear more damaged in the leading edge than in the other zones.

Fig. 68. The two models before and after the tests.

The altered morphology of the hemisphere after arc jet testing is shown in Fig. 69.

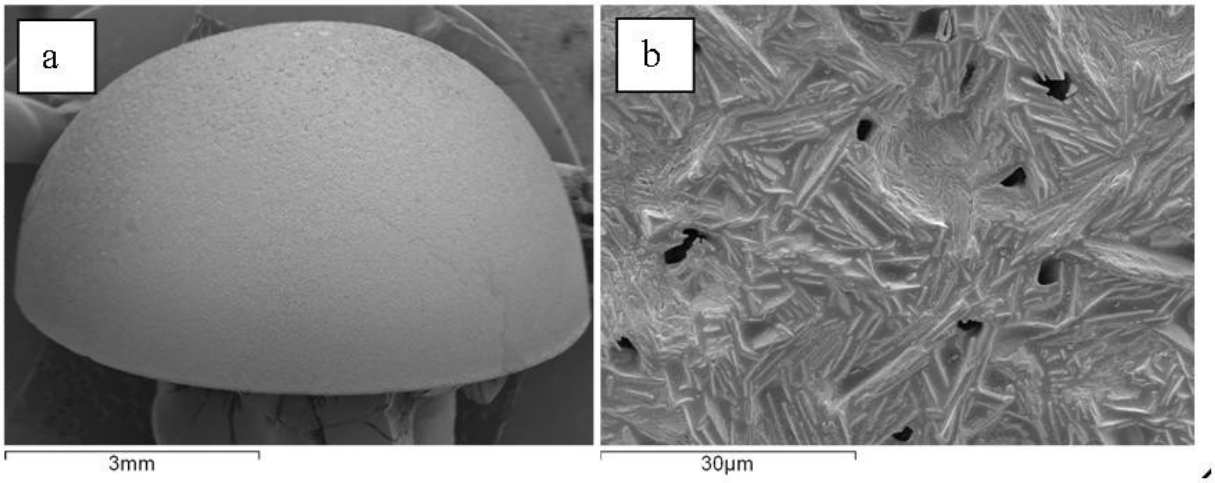

Fig. 69. The details of the hemisphere surface.

The sample surface presents holes with a diameter about 1µm, and it is covered by an amorphous silica-based scale, which embedded elongated crystals (Fig. 69). Holes are due to gas out flowing.

The analysis of the cross section (Fig. 70 and 71) reveals that the scale is a multilayered oxide having a variable thickness (130 μm in the near-tip region, 50 μm in the back). Despite the presence of few macro-cracks at the interface between oxide and unreacted bulk, the scale was quite well adherent to the bulk..

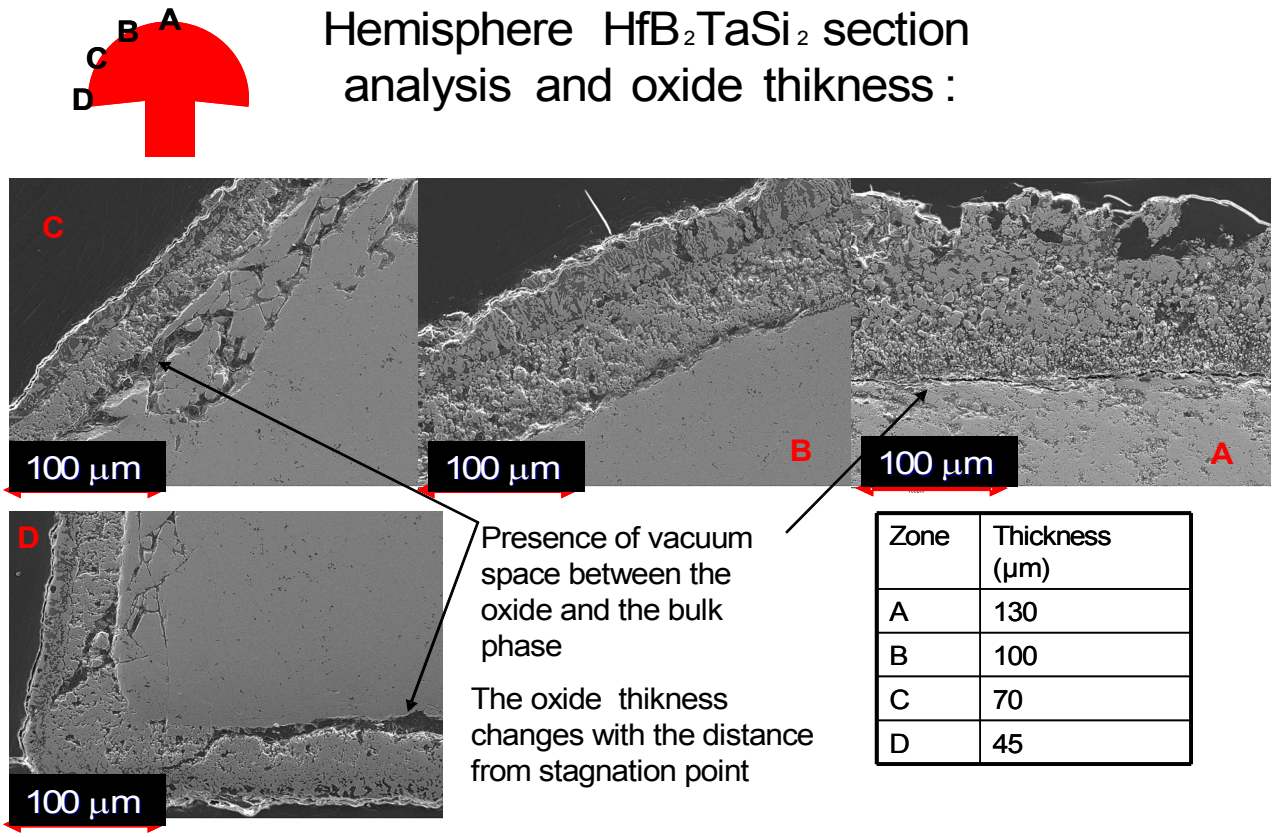

Fig. 70. The details of the oxidized layer for the hemisphere.

The different oxide layers of the hemisphere are shown in Fig. 71.

XRD pattern (not shown) revealed that the crystalline phases present after thermal treatment on the surface are prevalently a mixed oxide with extended crystals of $Ta_2O_5 \cdot 6HfO_2$ and traces of HfO_2, dispersed in protective silica (SiO_2) amorphous (Fig. 71). The silica–based scale contained several impurities, including Ta and Hf . Underneath the superficial layer, the scale was mainly constituted by porous HfO_2 in form of large rounded grains (~5 mm) containing a low amount of Ta (less than 3%). The inner layer was composed of fine HfO_2 grains (<2 mm) and residual porosity. Few silica was observed in the intermediate and inner sub-layers. Due to the severe conditions applied and the thermal cycling, micro-cracks were observed in both Hf, Ta-oxide and HfO_2 phases.

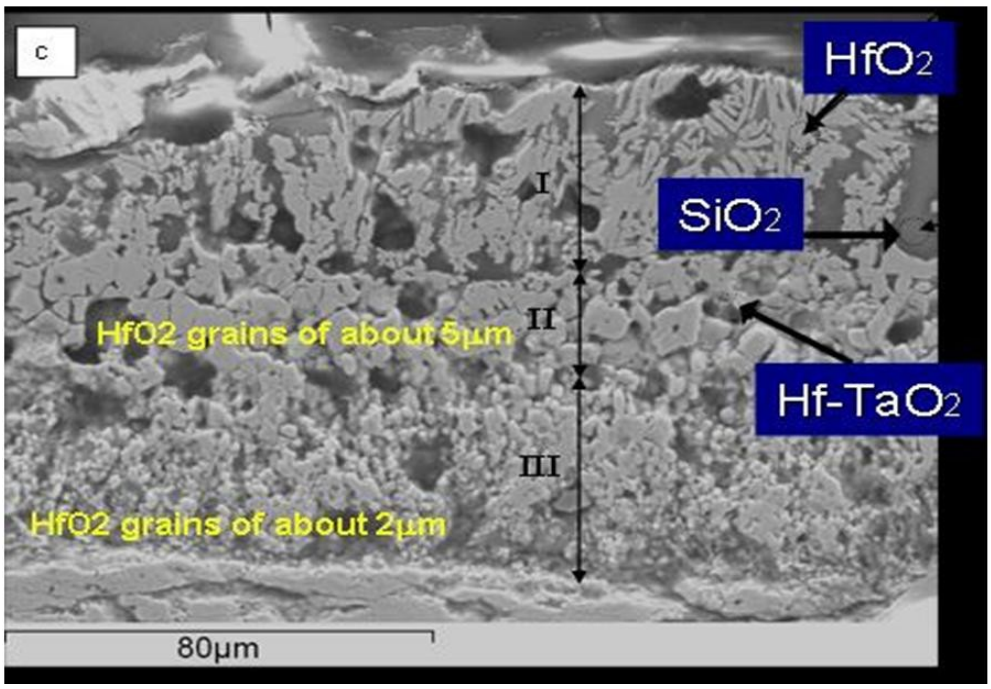

Fig. 71. oxide sub-layers of the hemisphere.

The cone model was subjected to a 2-time cycles from room temperature to the final temperature in about 150 s. For each run, the maximum temperature is held for about 90 s. According to numerical simulations, the maximum temperature on the tip is of order of 2800 K and rapidly decreased along the cone profile. The analysis of the sample surface revealed that the extent of damage was much more pronounced for this model respect to the hemisphere, due to high tip temperature, the leading edge oxide layer is turned down because it is detached from the bulk phase (Fig. 72).

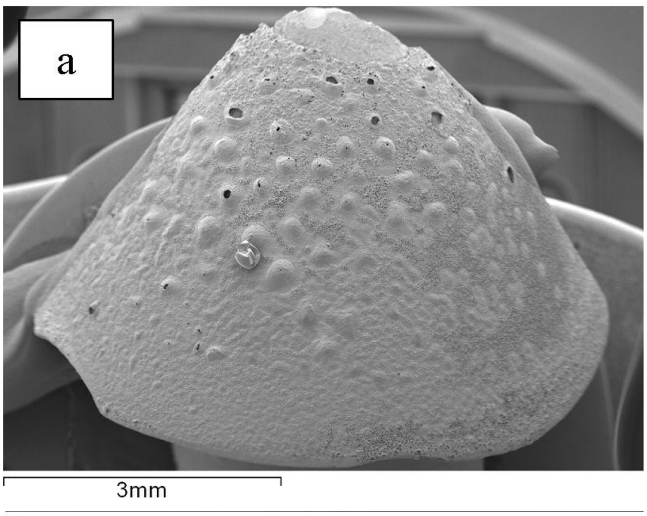

Fig. 72. Picture of the cone, surface leading edge damage, and porosity is visible.

The surface morphology was heavily altered by the shear forces associated to the hot stream, which enhanced the bursting of bubbles creating craters with diameter in the order of 10μm. The oxide layer in various zones of the cone's surface is shown in Fig. 73, the thickness is indicated also.

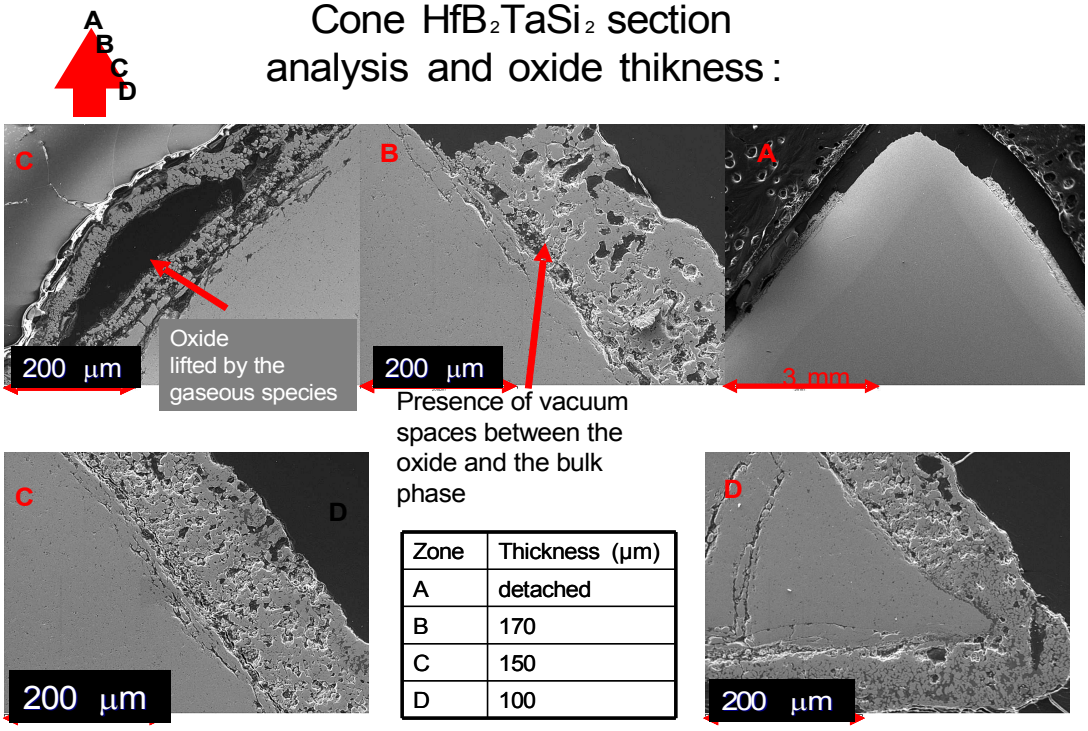

Fig. 73. The details of the oxidized layer for the cone.

The cone surface has less amount of $Ta_2O_5{\cdot}6HfO_2$ phase than hemisphere this implies that between 2300 and 2800 K, extensive evaporation of $Ta_2O_5{\cdot}6HfO_2$ occurs. As for the previous case, the scale is a multilayered oxide having a variable thickness (~170 mm near the tip, ~100 mm in the bottom part). The outer layer is constituted by a mixed Hf, Ta-oxide with stoichiometry $(Hf_{0.8}Ta_{0.2})O_2$ dispersed in the above mentioned Ta-containing silica amorphous layer.

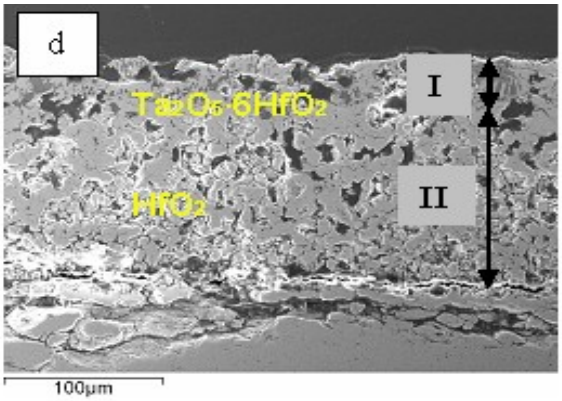

Fig. 74. Oxide layers of the cone.

Underneath the superficial oxide layer (Fig. 74), the scale was mainly constituted by large rounded HfO_2 grains (5 μm) containing a low amount of Ta (less than 3 at %) and large porosities. The presence

of silica in this layer was dependent on the position. No silica was observed in the near-tip regions. Some silica was instead observed in the bottom regions. Macro-cracks were observed at the interface oxide/unreacted bulk. The hafnium oxide crystals also presented micro-cracks.

The observed morphologies evidence that the samples underwent complex oxidation phenomena. Hafnium diboride is known to oxidise according to:

$HfB_2(s) + 5/2\ O_2\ (g) = HfO_2\ (s) + B_2O_3(l)$

$B_2O_3(l) = B_2O_3(g)$

Hafnia is a very stable phase in oxidizing atmosphere above 2300 K. It has a melting point of 3173 K and relatively low vapour pressure. HfO_2 in the pure form crystallizes in the monoclinic phase at room temperature, but transforms into the tetragonal phase over a temperature range of 373-2023 K, becoming fully tetragonal above 2023 K. This transformation is reversible and, during cooling, the return to the tetragonal phase is associated to a large volume change (3-4%) which can cause structural degradation, especially under repetitive thermal cycling. Thus, if the oxide is not stabilized with additives, cracking due to volume expansion is predictable. On the other hand, boron oxide has a low melting point and high vapour pressure, therefore at T>1373K, it starts to evaporate. Hence, the overall oxidation process of hafnium diboride is the result of the combined processes of oxygen inward or metal ion outward diffusion and, at relatively lower temperatures, gaseous/liquid products outward diffusion through the oxide scale.

Besides, $TaSi_2$ may oxidise according to: $2\ TaSi_2 + 6.5\ O_2(g) = Ta_2O_5 + 4\ SiO_2$, Ta_2O_5 is liquid at temperature between 1973 and 2073K. Thus the formation of liquid phase at the temperatures involved in the present experiments is confirmed.

The morphology of the observed oxides suggests the following oxidation phenomena. As the temperature rises and overcomes 2073 K, a liquid Ta-Si-O phase is formed on the sample surface, while HfB_2 oxidises to HfO_2 and liquid/gaseous B_2O_3 is formed. The Ta-Si-O phase further reacts with newly formed HfO_2 crystals, leading to formation of the $Ta_2O_5{\cdot}6HfO_2$ crystals with elongated morphology and a Ta-phase containing borosilicate glass. The $Ta_2O_5{\cdot}6HfO_2$ phase, which is not thoroughly investigated, can only be formed on the sample surface where the temperature is 1873 K or higher and where the Ta-Si-O phase is present. Indeed, this phase is not found in the intermediate and inner layers, which are depleted from the amorphous silica-based phase. As a confirmation, in the bottom regions of the sample, where the maximum temperature decreases, the $Ta_2O_5{\cdot}6HfO_2$ phase is not observed. The melting point of the $Ta_2O_5{\cdot}6HfO_2$ phase is not known exactly, i.e. it could be higher of lower than pure hafnium oxide.

Summarising, four aspects have come in evidence:

1) Also this UHTC changes the superficial composition, the emissivity, and thermal properties, if it is exposed in the SPES hypersonic high enthalpy flow, but after the first oxidation, the emissivity arrives at very low values (0.5) and it remains at this value independently from the temperature.
2) The coupling between the thermal insulator oxide layer with the low emissivity can have negative effects on the heating with temperature about 2800K for the cone.
3) For temperature up to 2200K, as those achieved by hemisphere, the UHTC HfB_2-$TaSi_2$ shows a good oxidation resistance.
4) Also the HfB_2-$TaSi_2$ has a non catalytic behaviour.

V.4. Arc jet tests on SiC compared with UHTC ZrB_2 systems

Tests on a SiC and ZrB_2 – SiC(15%vol) hemispherical models have been conducted with the standard SPES condition described earlier. Although the SiC is a good refractory material, it is not considered UHTC material. The SiC is used for the surface of RCC Space Shuttle's thermal shield. Both the materials have been siterized by hot pressing. This experiment have been conducted by incrementing the arc current from 300A up to 600A, corresponding to a maximum arc power of 36 kW. The maximum mass weighted average exit nozzle total enthalpy is 18MJ/kg, corresponding to the last step of the experiments.

The thermal histories for the two model are shown in Fig. 75, the measured temperature has exceeded the 2100K.

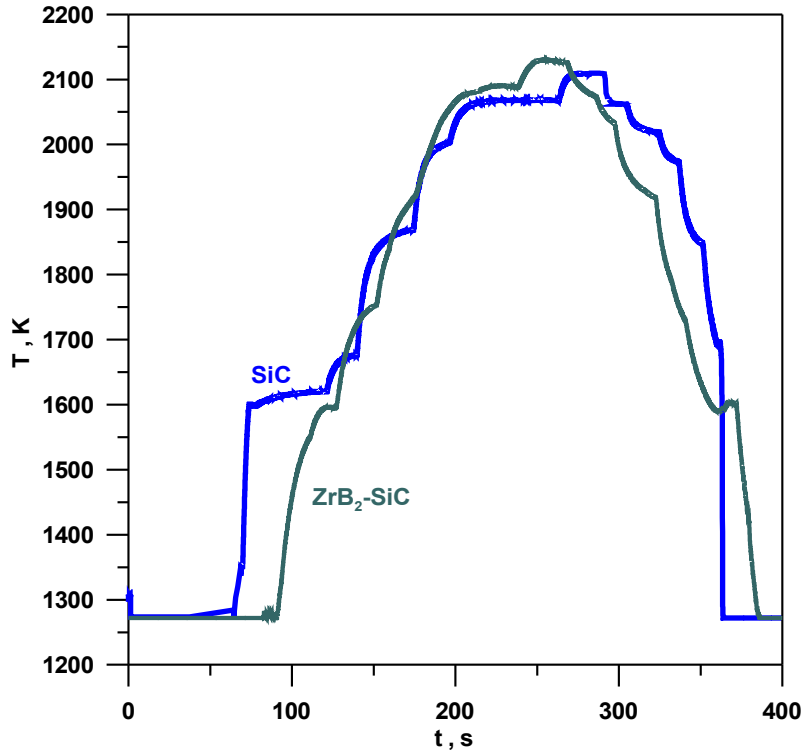

Fig. 75. Thermal histories for the two hemispherical models.

The Fig. 75 shows a similar maximum temperature, and thermal history, but the surfaces have had a different behaviour.

The Fig. 76 and Fig. 77 show the upper surface of the specimens after the exposure to the high enthalpy flow, and a cross section image.

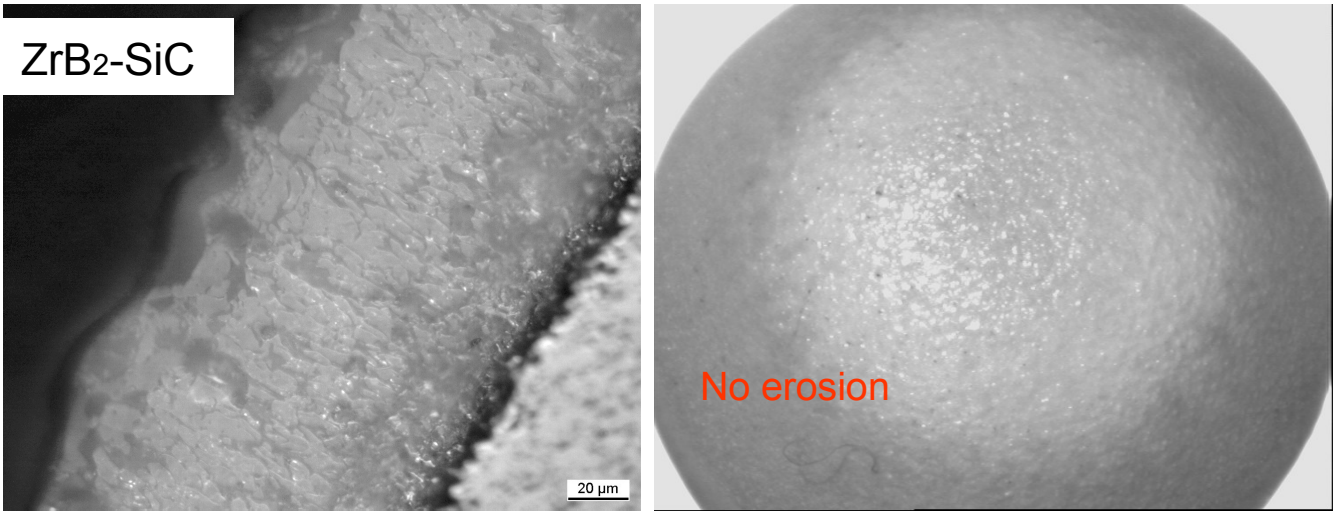

Fig. 76. The upper surface of the ZrB_2-SiC specimen after the exposure to the high enthalpy flow, and a cross section image.

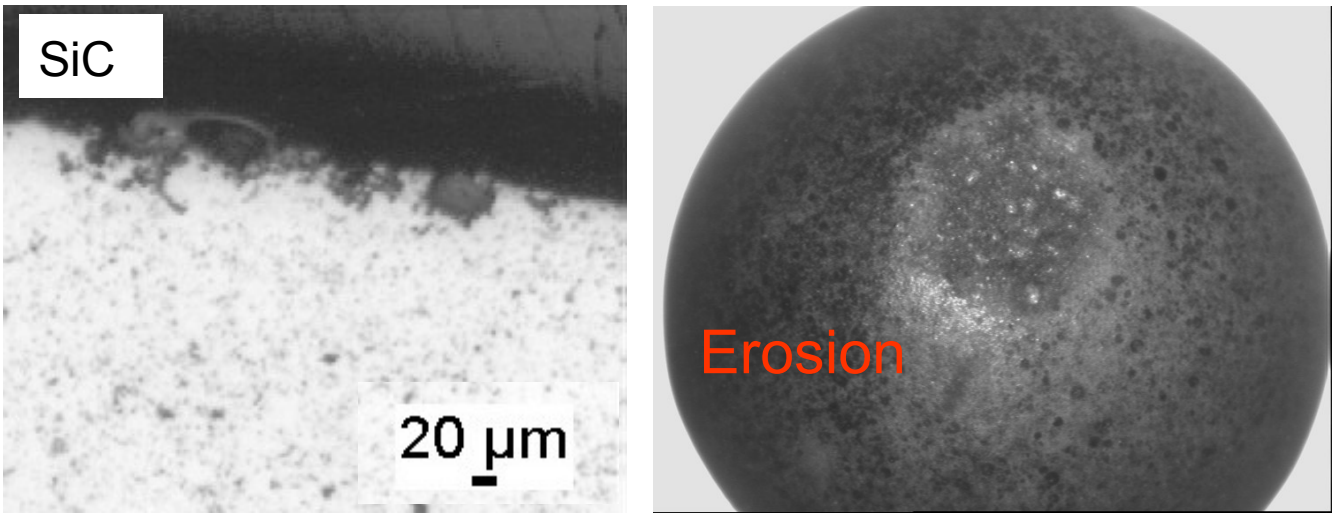

Fig. 77. The upper surface of the SiC specimen after the exposure to the high enthalpy flow, and a cross section image.

The oxide thickness of the ZrB_2-SiC model is bigger than that of the SiC, moreover the ZrB_2-SiC appears completely oxidised, instead the SiC remains of the same grey colour. But the SiC has been eroded in the stagnation point zone, instead the UHTC maintains the original geometry.

In the attempting to improve the ZrB_2 performances other additives have been tested. Sometimes the additive has got worse thermal performances. For example Fig. 78 shows a ZrB_2-based UHTC with non-protective additives.

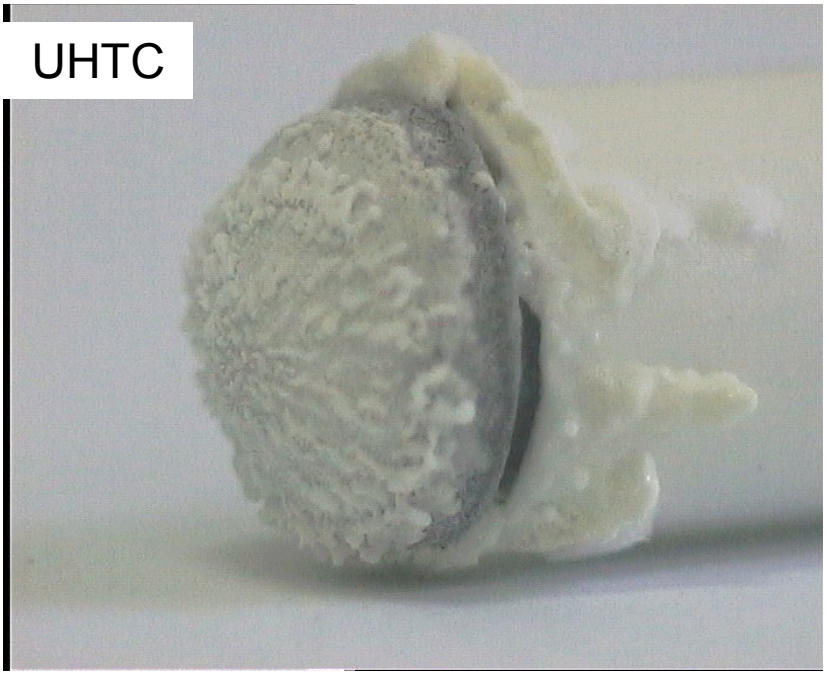

Fig. 78. A ZrB_2-based UHTC with non-protective additives, after the arc-jet exposure, the model is inserted in the alumina support.

The model was tested in the standard SPES conditions, i.e. mass flow rate of 1 g/s (0.8g/s N_2 and 0.2 g/s O_2), exit nozzle total enthapy of 15 MJ/kg, arc power of 500A. The maximum measured temperature was about 2000K.

The model before of the experiment had the standard hemispherical shape.

In the Fig. 79 there is a picture of the specimen during the test.

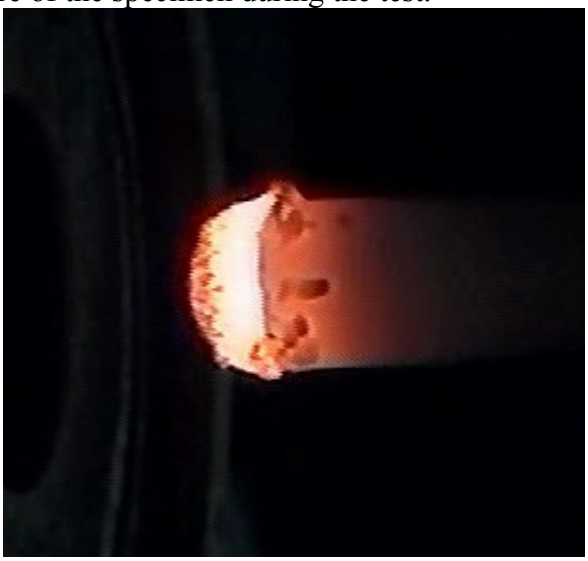

Fig. 79. A ZrB_2-based UHTC with non-protective additives, during the test.

V.5. Superficial catalytic behaviour of the UHTCs

It is important for a material designed for thermal shielding, the emissivity and the surface catalyticity. The emissivity must be high, but catalyticity must be very low to avoid excessive temperatures.

In fact the wall heat flux balance is :

$$h(T_\infty - T_w) = \varepsilon\sigma T_w^4 + k_s \overline{\nabla_s T} \cdot \bar{n} - \rho\alpha\big|_w K\ (T_w)\Delta H_r$$

The left hand side of equation is the total convective heat arriving at the wall, and the right hand side terms has the radiative and conductive energy subtracted at the wall of the specimen, and $\rho\alpha\big|_w K\ (T_w)\Delta H_r$ is the wall heat flux due to the atom recombination where $K(T_w)$ is the catalyticity constant depending the chemical species of the gas, on the wall temperature, chemical composition and roughness. From the above energy balance it is clear the importance of catalyticity in thermal heating.

The catalyticity constant is connected to the recombination coefficient γ_i by $K_i(T_w) = \gamma_i \sqrt{\frac{RT}{2\pi M_i}}$

For the definition of γ_i see par. IV.5.

The Fig. 80 shows the calculated wall heat flux for an hemispheric model (5mm radius) in the standard SPES conditions, i.e. at 1cm from exit nozzle, with mas flow rate of 1 g/s, arc current of 500A. The total enthalpy at the exit nozzle is 15MJ/kg.

The wall heat flux along the model's surface is calculated parametrically with surface recombination coefficient γ_i , the recombination coefficient γ_i is assumed to be the same for nitrogen as well as for the oxygen.

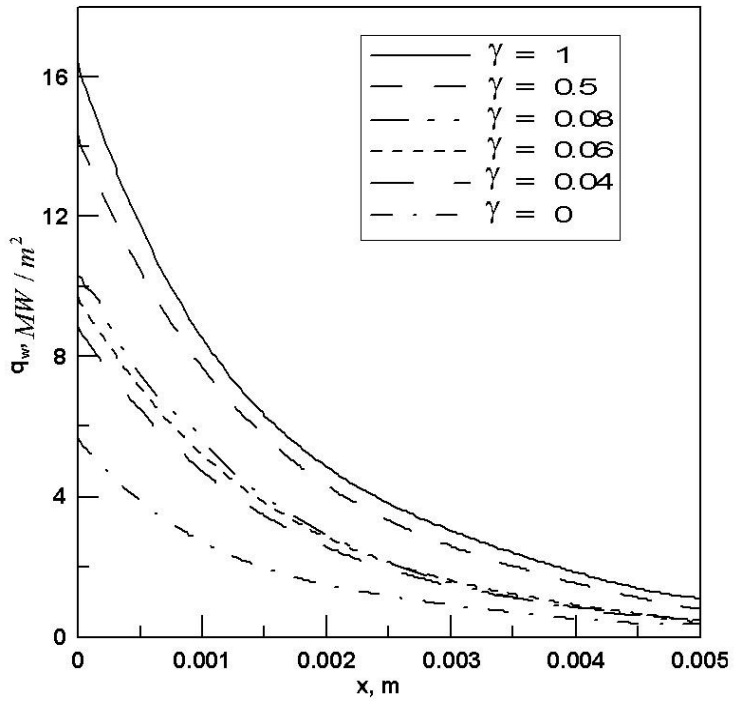

Fig. 80. The wall heat flux along the model's surface, calculated parametrically with surface recombination coefficient γ.

A surface recombination coefficient zero and one corresponds to the fully and non catalytic conditions respectively, it must be underlined the big difference between the the fully and non catalytic wall heat flux, the first one is about three times the second one.
For little specimen as those usually experimented in the SPES, the approximation of radiative thermal equilibrium has been verified. For this reason the maximum temperature in the pyrometer spot can be found by the formula: $\frac{T_1}{T_2} \cong \sqrt[4]{\frac{q_1}{q_2}}$ where q_1 and q_2 are the integral of the wall heat flux in the two conditions 1 and 2. In this case the fully catalytic spot temperature is about $\sqrt[4]{3}$ times higher than the non catalytic, i.e. 32% higher.

An example of catalytic surface behaviour is given by HfC-$MoSi_2$.

In the Fig. 81 there is the temperature Vs. the recombination coefficient, parametric with the arc power, for the UHTC HfC-$MoSi_2$.

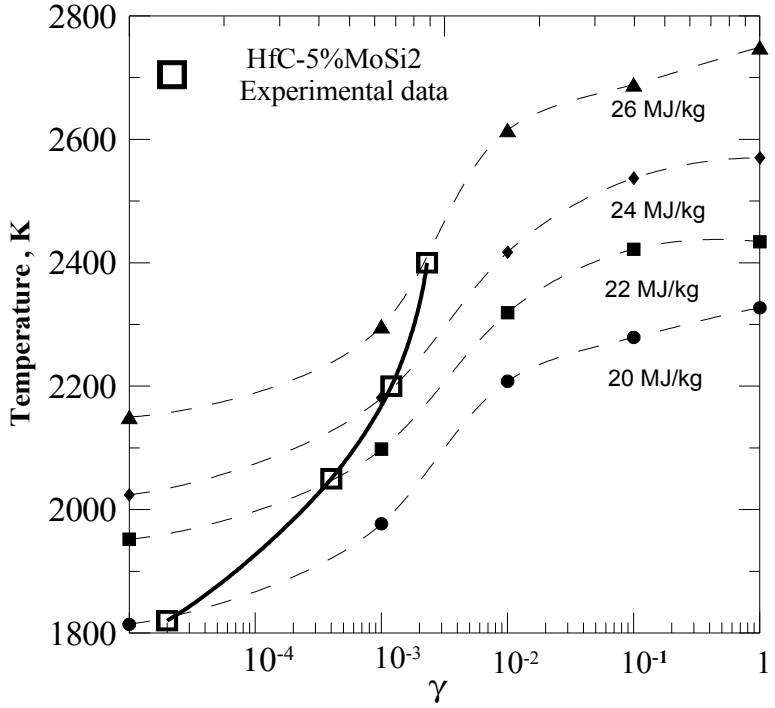

Fig. 81 Temperature Vs. the recombination coefficient, parametric with the arc power, for the HfC-$MoSi_2$

This results refer to arc jet testing in subsonic conditions, at atmospheric pressure. The condition are quite different from those specified above. In particular, in the torch there is 75% argon–25% nitrogen mixture plasma jet with mass flow rate of 1.45 g/s, for an average specific total enthalpy of the flow at the torch exit varying from 20 MJ/kg to 27 MJ/kg, at atmospheric pressure. At the exit of the torch the plasma containing argon, nitrogen and atomic nitrogen expands through a nozzle (5mm in diameter), comes into contact with the surrounding air at ambient conditions, so that oxygen in the atmosphere dissociates, and a reacting mixture composed of Ar, O2, N2, NO, O and N is formed.
From the Fig. 81 it is clear the dependence of γ from the temperature, for temperature below the 2000K the material results non catalytic. The emissivity in this conditions is resulted to be 0.7 at 1μm

wavelength. The specimen is located at a distance of 6 cm from the exit torch. The details of the experiment are given in [47].

The Fig. 82 shows another way to visualize the catalyticity, by plotting the experimental and numerical temperature points (calculated for both fully and non catalytic case) Vs. arc current and total enthalpy.

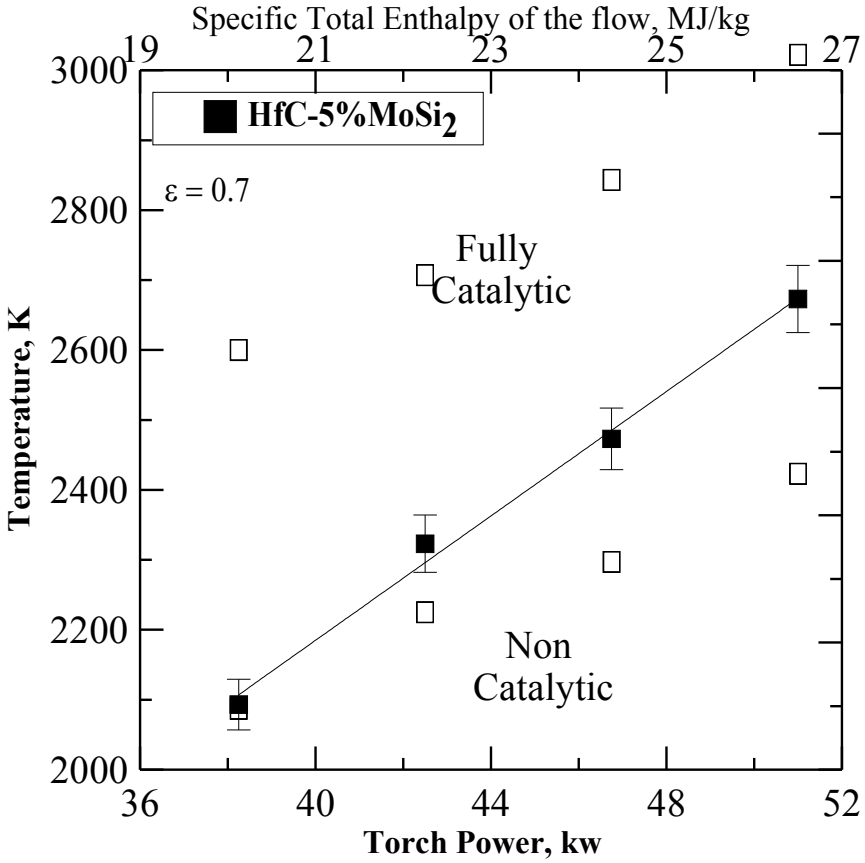

Fig. 82. The experimental and numerical temperature points (calculated for both fully and non catalytic case) Vs. arc current and total enthalpy.

From CFD, results an atomic oxygen and nitrogen mass fraction at the specimen wall, similar to that of the standard hypersonic-low pressure test (about 0.1 for both the species).

The maximum temperature above 2600K achieved it is due to the high value of the total enthalpy and to the high pressure respect to the standard value of the SPES supersonic conditions. As already mentioned in the Par. IV.2, also if a similar thermal history is obtained, the hypersonic test conditions have different chemical-physical results on the model. In particular in the subsonic test at atmospheric pressure, the oxidation is different, and the final emissivity of the exposed model is higher than that of model exposed at hypersonic flow.

The Fig. 83 and 84 show a comparison between the pictures of two model of ZrB_2-SiC before and after the test, this images give the idea of the different oxidation in the two types of testing.

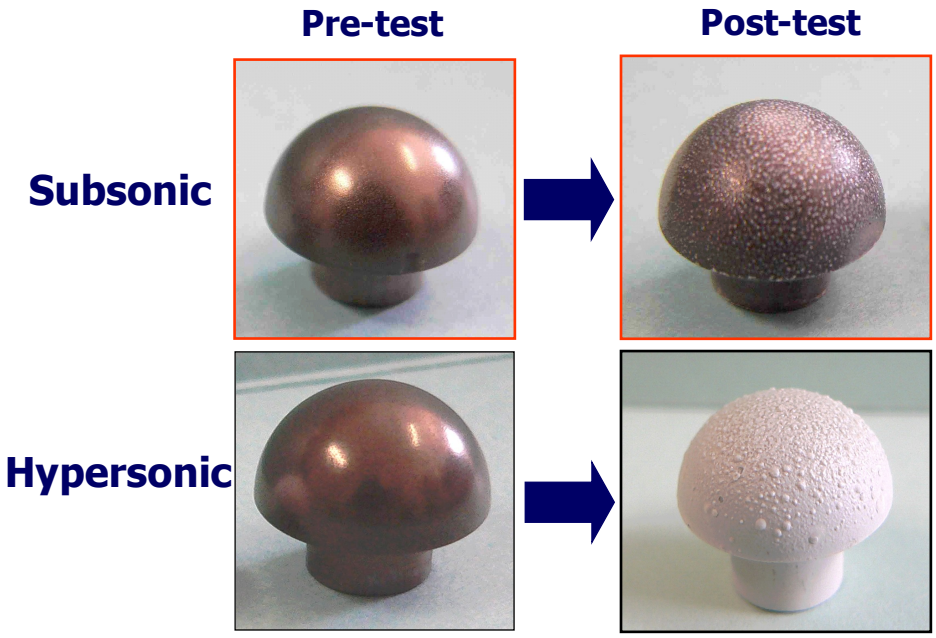

Fig. 83. Comparison between two model of ZrB_2-SiC before and after the experiments, tested in hypersonic and subsonic test conditions.

The oxidation (white colour) is pronounced in the hypersonic test because the presence of zirconia crystals close to the surface, in hypersonic the low pressure push the evaporation and bubble formation.

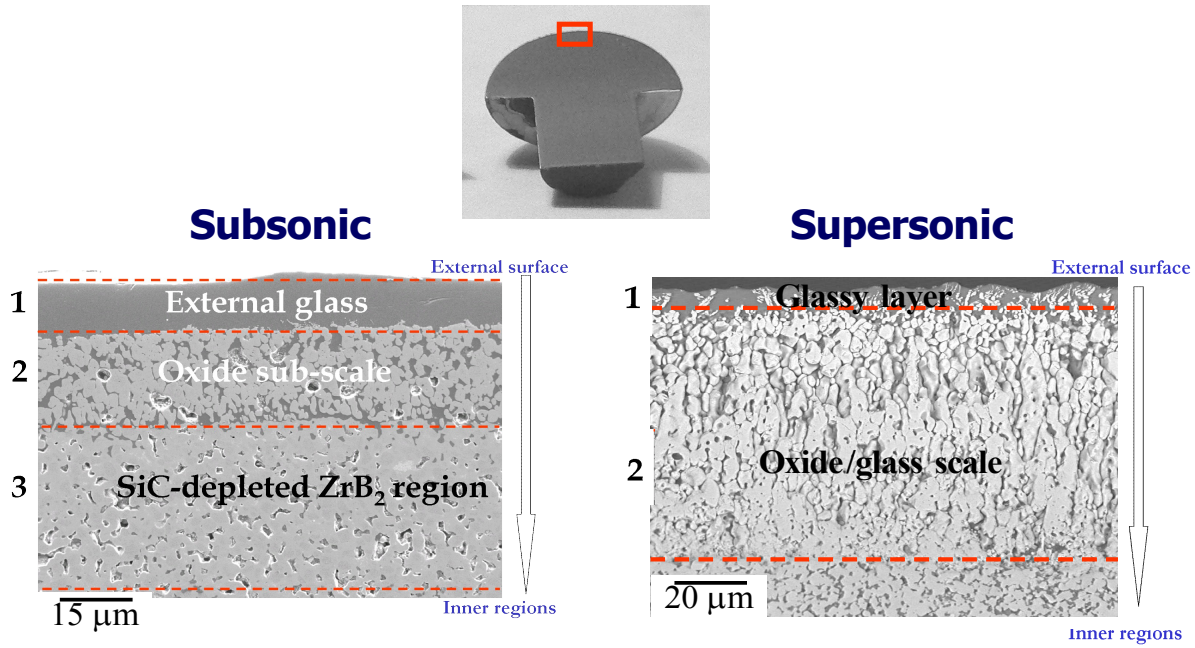

Fig. 84. Comparison of the cross sectioned oxide layer of two model of ZrB_2-SiC, tested in hypersonic and subsonic test conditions.

The subsonic test results in the presence on the surface of a thick silica layer that give at the model an high emissivity. In the subsonic tests elongated crystals are not present, but is present a SiC depleted region because the high temperature achieved.

Conclusions

The main objective of this thesis work has been the study of ultra-refractory ceramic materials in supersonic high enthalpy flows. Atmospheric re-entry conditions have been simulated by an arc-jet plasma wind tunnel.

The developed methodologies have been experimental and numerical.

The thesis is focused on the aerothermodynamic and oxidation behaviour of ultra-high-temperature Ceramic (UHTC) for aerospace applications.

UHTC are very high temperature resistant (>2000K) materials, with good chemical inertness and mechanical properties. These materials could be used for next generation aerospace and hypersonic vehicles.

The arc jet plasma wind tunnel available at the Department of Aerospace Engineering of Naples (DIAS) is able to reproduce specific total enthalpies and stagnation pressure conditions typical of atmospheric re-entry vehicles; for this reason advanced materials for hypersonic applications can be investigated. In particular, the materials behaviour at ultra high temperatures, the durability at repeated warmed up, and oxidation resistance can be analysed. The experimental procedure based on the simultaneous use of an infrared thermocamera and a dual-colour optical pyrometer allowed to take accurate measurements of the real temperature surface distributions during tests and to evaluate the spectral surface emissivity, which is a fundamental property for aero-thermal heating.

Numerical models allow the simulation of the aerothermochemical and flow fields characterizing the details of the wind tunnel experiments. For example the heat flux, the chemical environment on the model, the aero-thermal heating, and the effects of the material properties on the thermal heating can be analysed in detail.

The fundamental results obtained are: characterization of several UHTC models; they are original because specific properties of UHTC materials are provided for the first time. In particular the atomic recombination induced by surface catalyticity, the spectral emissivity, the oxidation behaviour and temperature resistance at temperatures in the order of 2000K. In addition, electronic micrographs and X-rays analysis of cross sections of the investigated UHTC samples after test, allow to characterize the oxidation layer and explain the measured surface properties

In fact in available literature there are few results of UHTC specimens tested in arc jet.

Some important points are:

1) For thermal heating analysis in the SPES's high enthalpy flow test, the optimal set-up is a small sized specimen, with an hemispherical or conical shape at 1cm from the exit nozzle, with an arc current of 500A, and a mass flow rate of 1 g/s.
2) A lot of UHTCs change the superficial composition, the emissivity, and thermal properties, if they are exposed in the SPES hypersonic high enthalpy flow.
3) The effects of thermal heating in hypersonic high enthalpy flow are quite different from those of plasma-torch or oxidation furnace exposition at atmospheric pressure.

4) The two conical and hemispherical geometries have similar thermal history only apparently, in fact the numerical analysis shows higher wall heat flux, and temperature on the tip of the conical model than hemispherical one.
5) The thickness of the oxide layer grows up with the temperature-time product, because both the cone and the hemisphere have the maximum oxide thickness on the leading edge, and depending on the time of exposition, also the dimensions of the oxide crystals are proportional to the time of exposure.
6) Above 2100K SiC-depleted diboride region can be found because 2100K is the melting point of silica, and the liquid film can be lost to volatility and shear forces in high velocity applications.
7) The most part of analysed UHTC material has a negligible catalytic behaviour.
8) The coupling between the thermal insulator oxide layer with the low emissivity can have negative effects on the heating with temperature about 2800K for the conical model.

For the future it is opportune to give high global emissivity at the oxidised UHTC specimen, because the tested models in low pressure conditions (200 Pa) have shown low values (0.5-0.7).

The develop of UHTC production technology will allow us to construct higher scale models to be tested, in prevision of full scale flight experiments.

References

1 J.D. Anderson, Hypersonic and High Temperature Gas Dynamic, McGraw-Hill, 1989

2 R. Monti, G. Pezzella, Low Risk Re-entry Vehicle, in: 12th AIAA International Space Planes and Hypersonic Systems and Technologies,15-19 December 2003, Norfolk, Virginia

3 R. Monti, D. M. Paterna, in: A Low Risk Reentry: Looking Backward To Step Forward , Aerospace Science and Technology, Volume 10, Issue 2, March 2006, Pages 156-167

4 R. Janowski, M. Tauche, M. Scheper, R. Monti, R. Savino, in: Spaceplane: a New Way for Atmospheric Reentry, In Proceedings of the 1st Inter-national ARA Days, Atmospheric Reentry Systems, Missions and Vehicles, Session 15-System Design, 2006.

5 R. Monti, R. Janovsky, R. Savino, M. De Stefano Fumo, in: Exploiting Lift Force in Reentries from Exploration Missions, DGLR International Symposium "To Moon and beyond", 14 - 16 March, 2007, Bremen, Germany.

6 I. E. Campbell, E. M. Sherwood, in: High-Temperature Materials and Technology, ed. Wiley, New York, 1967.

7 E. Wuchina, M. Opeka, S. Causey, J. Spain, A. Cull, J. Routbort, et al., in: Designing for Utrahigh-Temperature Applications: the Mechanical and Thermal Properties of HfB2, HfCx, HfNx and _Hf(N)), J. Mat. Sci., 2004, 39, 5939–5949.

8 E. V. Clougherty, L. Kaufman, Investigation of boride compounds for very high temperature applications, RTD-TRD-N63-4096, Part III, ManLabs, Inc., Cambridge, MA, 1966
Force Technical Documentary Report No. RTD-TDR-63-4096, 1963.

9 S. R. Levine, E Opila, M Halbig, J Kiser, M Singh, Evaluation of Ultra-High Temperature Ceramics for Aeropropulsion use. J. Eur. Ceram. Soc., 2002, 22(14–15), 2757–2767.

10 W. G. Fahrenholtz, G. E. Hilmas, NSF-AFOSR Joint Workshop on Future Ultra-High Temperature Materials, National Science Foundation Workshop, Arlington, VA, 13–14 January 2004.

11 R. Monti, M. De Stefano Fumo, R. Savino, in: Thermal Shielding of a Reentry Vehicle by Ultra High Temperature Ceramic Materials, J. Thermophys.
Heat Transfer, 2006, 20(3), 500–506.

12 R. Monti, R. Savino, D. Paterna, M. De Stefano Fumo, The Boundary Layer Thermal Protection System: an Advanced Concept for Protecting Hot Structures During Re-entry , Thermal Protection Systems and Hot Structures, Proceedings of the 5th European Workshop held 17-19 May, 2006 at ESTEC, Noordwijk, The Netherlands, Edited by K. Fletcher. ESA SP-631, European Space Agency, 2006. Published on CDROM, p.33.1.

13 K. Upadhya, J.M. Yang, and W. Hoffman, "Materials for ultrahigh temperature structural applications", Am. Ceram. Soc. Bull., vol. 76 (12), pp. 51– 56, 1997.

14 J. Marschall, A. Chamberlain, D. Crunkleton, and B. Rogers, "Catalytic atom recombination on ZrB_2/SiC and HfB_2/SiC ultrahigh-temperature 511ceramic composites", J. Spacecraft Rockets, vol. 41 (4), pp. 576–581, 2004.

15 M. Gasch, D. Ellerby, E. Irby, S. Beckman, M. Gusman, and S. Johnson, "Processing, properties and arc-jet oxidation of hafnium diboride/silicon carbide ultra high temperature ceramics", J. Mater. Science, vol. 39, pp. 5925– 5937, 2004.

16 A. Bongiorno, C. J. Forst, R. K. Kalia, J. Li, J. Marschall, A. Nakano, M.M. Opeka, I.G. Talmy, P. Vashishta, and S. Yip, "A perspective on modelling materials in extreme environments: oxidation of ultrahigh-temperature ceramics". MRS Bull., vol. 31, pp. 410–418, 2006.

17 N. Richet, P. Lespade, P. Goursat, and E. Laborde, "Oxidation resistance of HfB2–SiC coatings for protection of carbon fibre based composites". Key Eng. Mater., pp. 264–268 (TTP), pp. 1047–1050, 2004.

18 A. Francese, Numerical and experimental study of UHTC materials for atmospheric re-entry, PhD dissertation, Federico II University of Naples, 2006.

19 John David Anderson, Computational Fluid Dynamics, McGraw-Hill Science/Engineering/Math; 1 edition, 1995.

20 Bertin JJ, Cummings RM. 2003. Fifty years of hypersonics: where we've been, where we're going. Progr. Aerosp. Sci. 39:511–36.

21 Brown, S. L. Approximate Riemann Solvers for Moment Models of Dilute Gases. PhD thesis, The University of Michigan, 1996.

22 M. G. Dunn, and S. W. Kang, Theoretical and Experimental Studies of Reentry Plasmas, NASA CR-2252, April 1973.

23 C. Park, "Assessment of Two-Temperature Kinetic Model for Ionizing Air," AIAA Paper 87-1574, June 1987.

24 J.S. Evans, C. J. Schexnayder, Jr., and Paul K. Huber, Boundary-Layer Electron Profiles for Entry of a Blunt Slender Body at High Altitude, Langley Research Center, NATIONAL AERONAUTICS AND SPACE ADMINISTRATION WASHINGTON, D. C. JULY 1973.

25 E.W. Miner, and C.H. Lewis, Hypersonic Ionizing Air Over Nonanalytic Blunt Bodies Viscous Shock-Layer Flows, National Aeronautics And Space Administration Washington, d. C. May 1975.

26 Park, Review of Chemical-Kinetic Problems of Future NASA Mission, I Earth Entries, 1993.

27 R. N. Gupta, J. N. Yos, R. A. Thomson, a review of reaction rates and thermodynamic and transport properties for the 11-species air model for chemical and thermal nonequilibrium calculations to 30000 k, NASA, Langley Rosearch Center, Hampton. Virginia 23665-5225, February 1989.

28 Scalabrin, Boyd, Numerical Simulation of Weakly Ionized Hypersonic Flow for Reentry Configurations, AIAA/ASME conference, 2006 LORE memorandum: Description And Validation of a New Developed Three-dimensional Thermo-chemical Nonequilibrium Navier-Stokes Solver, TUDelft, 1997.

29 Grundmann, Computational Methods In Hypersonic Aerodynamics, Editore: Kluwer Academic Publishers, 1992.

30 C. Park, Assessment of a two-temperature model for dissociating and weakly ionizing nitrogen, J. Thermophysics and Heat Transfer-2. 8-16,1988.

31 Park, C. 1993 Review of chemical-kinetic problems of future NASA mission, I: Earthentries. Journal of Thermophysics and Heat Transfer, 7(3) 385.

32 Millikan, R.C. White, D.R. Systematics of Vibrational Relation, J. Of Chem. Phys., vol. 39, 1963, pp. 3209-3213.

33 Hoffman K., Computational Fluid Dynamics, Engineering Education System, 1996.

34 Thoemel J., Chazot O., and Barbante P., Aspects of advanced catalysis modelling for hypersonic flows, Center for Turbulence Research, in proceedings of the Summer Program, 2008.

35 Carlomagno Giovanni M., Fluidodinamica, Editor: Liguori, ISBN: 9788820732790, 2004.

36 W.G. Fahrenholtz, G.E. Hilmas, I.G. Talmy, and J.A. Zaykoski, “Refractory Diborides of Zirconium and Hafnium,” J. Am. Ceram. Soc., vol. 90, pp. 1347-1364, May 2007.

37 Elizabeth J. Opila*, Jim Smith, Stanley R. Levine*#, Jonathan Lorincz&, Marissa Reigel†Oxidation of TaSi2-Containing ZrB2-SiC Ultra-High Temperature Materials ; Open Aerospace Engineering journal 2009.

38 J.B. Berkowitz-Mattuck, “High Temperature Oxidation III. Zirconium and Hafnium Diborides,” J. Electrochem. Soc., vol. 113, pp. 908-914, Sept. 1966.

39 E.V. Clougherty, R.L. Pober, and L. Kaufman, “Synthesis of Oxidation Resistant Metal Diboride Composites,” Tran. Of Metall. Soc., vol. 242, pp. 1077-1082, June 1968.

40 X.-H. Zhang, P. Hu, and J.-C. Han, “Structure Evolution of ZrB2-SiC During the Oxidation in Air,” J. Mater. Res., vol. 23, pp. 1961-1972, July 2008.

41 Marschall, J, Pejakovic, D.A., Fahrenholtz, W.G., Hilmas, G.E., Zhu, S., Ridge, J.,. Fletcher, D. G C., Asma, O., and Thomel, J., Oxidation of ZrB_2-SiC ultrahigh-temperature ceramic composites in dissociated air. J. of Thermophysics and Heat Transfer, 2009, 23(2), 267-278.

42 Monteverde, F., and Savino, R., Stability of ultra-high-temperature ZrB_2-SiC ceramics under simulated atmospheric re-entry conditions. J. Europ. Ceram. Soc., 2007, 27, 4797-4805.

43 Monteverde F.; Savino R., ; De Stefano Fumo M.; Di Maso A., Plasma wind tunnel testing of ultra-high temperature ZrB2-SiC composites under hypersonic reentry conditions, Journal of the European Ceramic Society, 2009.

44 Lofthouse Andrew J., Nonequilibrium Hypersonic Aerothermodynamics Using the Direct Simulation Montecarlo and Navier Stockes Models. A dissertation submitted in partial fulfillment of the requirements for the degree of Doctor of Philosophy (Aerospace Engineering) in The University of Michigan 2008.

45 Zhang X., P. Hu, J. Hun, and S. Meng, "Ablation Behavior of ZrB2-SiC Ultra High Temperature Ceramics under Simulated Atmospheric Re-Entry Conditions," Comp. Sci. & Tech., vol. 68, pp. 1718-1726, 2008.

46 Di Maso A., Savino R., De Stefano M., Silvestroni L., Sciti D., Arc-jet testing on HfB_2- $TaSi_2$ models: effect of the geometry on the aerothermal behaviour, Open Aerospace Engineering Journal, 2009.

47 Savino R.,*, De Stefano Fumo M.,Silvestroni L.,Sciti D., Arc-jet testingon HfB2 and HfC-based ultra-high temperature ceramic materials, Journal of the European Ceramic Society, 1899–1907, 28, 2008.

Acknowledgements
The SEM micrography, the chemical analysis, and the sintering of UHTC specimens in the present work have been performed by F. Monteverde, D. Sciti, and L. Silvestroni, and several technicians of the ISTEC institute in Faenza (Ra).

I wish to thank all the people who have been close to me in this three years.
The my family, who has accepted the idea to live with me at home again, for other three long years without showing a bit of intolerance.
The my colleagues: Mario named "Col. St. The Motivator" who has taught to me a lot of things and with whom I have shared a lot of time, and of soccer and tennis matches; Roberto, named "the Guiscardo" , Roberto named "the Intrapendente", and Lino who have improved very much the quality of a lot of days. I am sure to forget someone, but I hope to be excused because in this moment I am very tired.
Overall I wish to thank God, because above all I am here, still in an apparently perfect health, still I am able to hope in the future.